UNIVERSITÀ DEGLI STUDI DELL'AQUILA
DIPARTIMENTO DI INGEGNERIA CIVILE, EDILE – ARCHITETTURA E AMBIENTALE

Dottorato di Ricerca in Ingegneria

Curriculum Civile e Ambientale

XXXVI ciclo

Titolo della tesi

Seismic Hazard evaluation for Urban Planning through A-DInSAR Data and In Situ Investigation: The Case Study of L'Aquila (Abruzzi, Central Italy)

SSD GEO/05

Dottoranda

Alessandra Sciortino

Coordinatore del corso

Prof. Marcello Di Risio

Tutor

Prof. Marco Tallini

Prof. Paolo Mazzanti

a.a. 2022/2023

Contents

Riassunto

Il centro storico dell'Aquila è collocato nell'Appennino centrale, in una regione d'Italia soggetta ad elevato rischio sismico. La città è stata colpita da numerosi terremoti sia storici e recenti. Tra questi, il sisma di magnitudo 6.3 del 6 aprile 2009 e quello di magnitudo 6.7 del 2 febbraio 1703 hanno danneggiato gravemente e distrutto la maggior parte degli edifici della città. In questa tesi viene illustrata un'analisi statistica integrata dei dati di danneggiamento sismico degli edifici del centro storico dell'Aquila e delle deformazioni al suolo, riconosciute mediante Interferometria Differenziale SAR Satellitare Avanzata (A-DInSAR). Confrontando le mappe di danneggiamento sismico del 2009 e del 1703 con la mappa A-DInSAR prodotta a partire dalle immagini acquisite in orbita discendente da Cosmo-SkyMed (tra il 2010 e il 2021), è stata riconosciuta una correlazione tra le deformazioni post-sismiche e l'intensità dei danni agli edifici. È stata condotta un'analisi differenziata delle velocità di deformazione del terreno e di quelle che interessano gli edifici, al fine di valutare l'impatto delle caratteristiche strutturali e delle opere di ristrutturazione e ricostruzione sulle deformazioni registrate da satellite. L'analisi geostatistica ha rivelato la presenza di una subsidenza diffusa (fino a -5 mm/anno) in tutta l'area di studio e l'assenza di correlazione spaziale. Attraverso una Cluster Analysis è stato possibile riconoscere trend di subsidenza/sollevamento ricorrenti che, in termini di forma delle curve spostamento - tempo, sembrano indipendenti dall'intensità del danneggiamento e dalle opere di ricostruzione.

Poiché questi risultati sottolineano come l'entità dei danni subiti dagli edifici nel centro dell'Aquila, sia nel caso del terremoto del 2009 che in quello del 1703, sia direttamente correlata al livello di subsidenza rilevato tramite le mappe A-DInSAR, ho analizzato attentamente i fattori geologici che potrebbero influenzare la distribuzione delle deformazioni nell'area di studio, con l'obiettivo di comprendere meglio il danneggiamento sismico registrato.

Grazie alla disponibilità di una lunga serie temporale di dati InSAR acquisiti dalle missioni Cosmo-SkyMed e Sentinel-1, è stato possibile valutare le relazioni tra le deformazioni del terreno e la Vs delle litologie affioranti, la profondità della falda

acquifera e altri fattori geologici e geomorfologici. L'analisi di correlazione tra i fattori predisponenti e la deformazione SAR ha evidenziato un aumento della subsidenza fortemente condizionato dalla litologia affiorante, mostrando come le variazioni composizionali all'interno di una litologia possano influenzare significativamente le deformazioni al suolo. Inoltre, è emerso che la profondità della falda acquifera influenza la subsidenza a lungo termine, mentre le sue fluttuazioni stagionali sono responsabili di oscillazioni di second'ordine delle velocità nelle curve spostamento - tempo.

I risultati ottenuti aprono la strada a un nuovo utilizzo delle serie temporali di dati SAR satellitari in zone ad alto rischio sismico, fungendo da strumento prezioso per la mappatura delle aree più suscettibili e la mitigazione del rischio sismico.

Abstract

L'Aquila downtown (Central Italy) is situated in a highly seismic region, making it susceptible to numerous historical and recent earthquakes. Among these, the earthquake of Mw 6.3 on April 6, 2009, and the one of Mw 6.7 on February 2, 1703, caused severe damage or complete destruction of the majority of buildings in the historical center. An integrated statistical analysis of A-DInSAR and seismic related building damage data is illustrated. By comparing the seismic damage maps from the 2009 and 1703 earthquakes with the A-DInSAR map produced with Cosmo-SkyMed descending orbit images (acquired between 2010 and 2021), a correlation between post-seismic deformations (in terms of average velocity) and building damage intensity has been identified. Furthermore, ground and building velocities have been separately examined, in order to evaluate the impact of building features and reconstruction efforts on ground deformations. The geostatistical analysis revealed a widespread subsidence motion (until -5 mm/year) across the whole study area. Notably, neighboring points did not exhibit consistent deformation velocities, indicating a lack of spatial correlation. Additionally, Cluster Analysis has allowed recognition of recurring subsidence/uplift trends, which, in terms of shape of curve displacement vs. time, appears independent on building damage intensity or reconstruction interventions. As these results shown that the intensity of damage to buildings in L'Aquila downtown, both in the case of the 2009 earthquake and the 1703 earthquake, is proportional to the post-seismic subsidence rate detected through A-DInSAR maps, I've analyzed the geological factors that might control deformations (and therefore seismic damage) in the study area. Thanks to the availability of a long time series of InSAR data acquired from the Cosmo-SkyMed and Sentinel-1 missions, it has been possible to analyze the relationships between ground deformations and the Vs of the outcropping lithology, depth of water table, and other geological and geomorphological factors that could determine deformation pattern. The correlation analysis between predisposing factors and SAR deformation has highlighted an increase in subsidence strongly conditioned by the outcropping lithology, showing how compositional variations within a lithology can significantly influence ground deformations. Furthermore, hydrogeology has been recognized as playing an important role in determining deformation processes: the depth of the water table locally

influences long-term subsidence, while seasonal fluctuations in the water table are responsible for secondary areal variations in ground deformations.

The obtained results pave the way for a novel utilization of long-term series of satellite SAR data in high-risk seismic zones, serving as a valuable tool to map the most susceptible areas and mitigate seismic risk.

Chapter I - Introduction

The study of pre- and post-seismic ground behavior is of increasing importance in the context of seismic risk mitigation, and predicting the local seismic effects induced by earthquake is of course crucial for urban planning. The extent of building damage resulting from a seismic event is contingent upon both inherent structural characteristics (such as geometry, number of floors, loadings, construction material, foundation typology, year of construction, and, if applicable, maintenance status (Peduto, Ferlisi, et al., 2017; Peduto, Nicodemo, et al., 2017)) and the intensity of specific parameters linked to subsidence (including absolute settlements, differential settlements, angular distortions, and relative rotations (Ferlisi, S., Nicodemo, G., Peduto, D. Negulescu & Grandjean, 2020; Mair et al., 1996; Peduto, Ferlisi, et al., 2017; Skempton & Mc Donald, 1956)).

However, traditional tools for measuring soil movement may prove inadequate for characterizing urban-scale deformations, where heterogeneity poses a risk of underestimating ground displacement rates (Nappo et al., 2020, 2021). In last decades, Advanced Satellite Interferometric Synthetic Aperture Radar (A-DInSAR) (Berardino et al., 2002; Alessandro Ferretti et al., 2001) has emerged as a pivotal tool in civil engineering, as it enables the identification of surface deformations with extreme precision (up to the millimeter level), allowing for the assessment of their temporal evolution and spatial distribution and benefiting from having relatively low cost, short revisiting time and wide area coverage (Cigna et al., 2011; Ezquerro et al., 2020; Tomás et al., 2014).

This technique exploits the presence of points on the Earth's surface, known as Persistent Scatters (PS), characterized by consistently high reflectivity over time. The A-DInSAR technique allows the estimation of ground displacement and reconstruction of the deformation history of radar targets (PS). The applications of this technique are manifold: studying slope instability phenomena (Bordoni et al., 2018; Bru et al., 2017; Mantovani et al., 2019), monitoring seismic and volcanic areas (Di Traglia et al., 2021), analyzing deformative processes in mining areas (Antonielli et al., 2021; Herrera et al., 2012), monitoring dams, infrastructure, and much more.

Although A-DInSAR techniques have been used to characterize ground deformations for various geological processes (Capes & Teeuw, 2017; Ciampalini et al., 2014; Comerci et al., 2015; Del Soldato et al., 2019; Vallone et al., 2008)), the comparison between post-seismic A-DInSAR maps and maps showing seismic damage associated with both historical and recent earthquakes has not been extensively explored. For this reason, through the use of quantitative data and statistical analyses, this study challenges the application limitations of the technique: the aim of this research is to conduct an in-depth analysis of A-DInSAR deformation maps to assess its potential use in predicting seismic effects at the scale of individual buildings and identifying highly susceptible areas.

In terms of seismic risk mitigation, mapping the most susceptible areas is crucial, especially in contexts like that of the Central Apennines, highly prone to seismic activity and often responsible for the damage and destruction of cities and villages (Stucchi et al., 2011; Valensise et al., 2017).

The focus of this study is the historic center of L'Aquila, an Italian city with a population of 73,000, situated in the highly seismic region of the Central Apennines. This city, renowned for its significant cultural heritage, has endured the impact of numerous earthquakes over time, profoundly influencing its urban development. Notable among these seismic events are the November 26, 1461 earthquake, which led to the destruction of medieval structures, and the February 2, 1703 earthquake (with a macroseismic magnitude of Mw 6.7 [27]), which shaping the present urban layout. Subsequently, the city faced another devastating earthquake on April 6, 2009, registering Mw 6.3, causing extensive damage and destruction to a majority of buildings in the historic center.

This PhD thesis delves into analyzing the pattern of building damage within L'Aquila's central area resulting from the 2009 and 1703 seismic events. Additionally, it evaluates the influence of geological, hydrogeological, and geomorphological conditions on the spatial distribution of deformations identified through satellite-based observations.

In the initial section of my PhD thesis, I delve into comparing satellite-derived deformations during the post-seismic period with the spatial distribution of building damages. To accomplish this, I meticulously examined point-based deformation values measured in mm/year obtained from descending Cosmo-SkyMed images spanning from 2010 to 2021. These measurements were juxtaposed with damage maps specifically detailing the impact on L'Aquila's historic center from the earthquakes of 2009 (Tertulliani et al., 2011) and 1703 (Colapietra, 1978). This comparative analysis involved a comprehensive evaluation of both ground and building velocities, allowing an assessment of the potential influence of building vulnerability and reconstruction efforts on the Line of Sight (LOS) deformations. Moreover, through geostatistical analysis, I evaluated the spatial characterization of deformations within the study area. Finally, I show the findings from statistical and clustering analyses, aimed at identifying coherent displacement patterns among the time series data obtained from monitored points.

The second part of this thesis aims to clarify the geological and geomorphological conditions that determine the distribution of deformation in the study area. Indeed, a deep understanding of geology is essential for interpreting InSAR maps (Nappo et al., 2020; Tosi et al., 2009) and investigating deformations induced by geological processes (Cigna et al., 2011; Nappo et al., 2020). Furthermore, several previous studies (Amoroso et al., 2018; Antonielli et al., 2020a; Del Monaco et al., 2013; Durante et al., 2017; Mannella et al., 2019; Martelli et al., 2012; Nocentini et al., 2017b) have shed light on the influence of the variability (both spatially and in terms of thickness) of continental deposits, which represent the city's substrate, on seismic site amplification (Macerola et al., 2019). These insights, combined with a comprehensive database of geological and geophysical surveys conducted in the city of L'Aquila (many of which were carried out after 2009 to expand knowledge of seismic site amplifications in the urban area), enable to assess the satellite deformations recorded by Cosmo-SkyMed and Sentinel-1 missions, while examining subsurface geology from a new perspective. In this phase of the research, the most relevant geological-geomorphological factors for deformation analysis have been identified; existing surveys in the historic center of L'Aquila have been reanalyzed to produce a detailed geological map, and Pearson's

correlation coefficient (PCC) analysis has been used to assess the influence of factors such as the thickness of the Red Soils (RS), depth of the regional aquifer, terrain slope, and surface geology on InSAR deformations. Moreover, the correlation between precipitation and seasonal ground deformation has been evaluated.

The thesis is structured into five chapters: the first consists of this brief introduction detailing the motivations and objectives guiding the research. The second and third chapters represent the core of the study and consist of two scientific papers. The first article, titled "*Satellite A-DInSAR pattern recognition for seismic vulnerability mapping at city scale: insights from the L'Aquila (Italy) case study*" has been published by the journal GIScience & Remote Sensing in December 2023. The second, "*Geological and Hydrogeological Drivers of Seismic Deformation in L'Aquila, Italy: Insights from InSAR Analysis*," has been submitted to the same journal and is currently under review. Both articles feature an internal structure with chapters and sections whose numbering remains distinct from the main thesis. Additionally, the figure numbering in chapters II and III is specific to each scientific article. The fourth chapter discusses the main results, while the fifth and final chapter presents the key conclusions and future research perspective. Lastly, the 'References' section includes a comprehensive list of all bibliographic references cited in the text.

Chapter II - Satellite A-DInSAR pattern recognition for seismic vulnerability mapping at city scale: insights from the L'Aquila (Italy) case study

1. Background and state of the art

The continuous development of remote sensing techniques, particularly SAR (Synthetic Aperture Radar) satellite technology, greatly supports the field of civil engineering, especially in urban planning. Advanced Differential Synthetic Aperture Radar Interferometry (A-DInSAR) techniques (Berardino et al., 2002; Alessandro Ferretti et al., 2001) is one of the most widely used tools in this regard as it enables the identification of surface deformations with extreme precision (up to the millimeter level), allowing for the assessment of their temporal evolution and spatial distribution and benefiting from having relatively low cost, short revisiting time and wide area coverage (Cigna et al., 2011; Ezquerro et al., 2020; Tomás et al., 2014). This technique is extensively employed in order to analyze various natural and anthropic deformation phenomena, e.g., slope instabilities (Bordoni et al., 2018; Bru et al., 2017; Mantovani et al., 2019), volcanoes (Di Traglia et al., 2021), subsidence (Nappo et al., 2020; Tomás et al., 2014), tailings dam (Mazzanti et al., 2021) and mining areas (Antonielli et al., 2021; Herrera et al., 2012). Through the characterization of ground deformations, A-DInSAR techniques are also used to study urban damage induced by various geological processes (Capes & Teeuw, 2017; Ciampalini et al., 2014; Comerci et al., 2015; Del Soldato et al., 2019; Vallone et al., 2008). However, the comparison between post-seismic A-DInSAR maps and damage maps for recent and historical near-source earthquakes has not been extensively explored. Therefore, in this work, through the use of quantitative data and appropriate statistical analyses, we aim to deepen into this aspect. Indeed, mitigating seismic risk also necessitates mapping the most susceptible areas, especially in geological contexts such as the Central Apennines, which are prone to intense seismic activity (Fig.1, panel A) and are often responsible for causing damage or destruction to towns and villages (Stucchi et al., 2011; Valensise et al., 2017).

With a population of approximately 73,000 inhabitants (A. Tertulliani et al., 2012), L'Aquila is a medium-sized city in central Italy (Figure 1), characterized by a notable cultural heritage. It is situated in a seismic zone (Galadini et al., 2003; P. Galli et al., 2002; M. Moro et al., 2013; Stucchi et al., 2011; Andrea Tertulliani et al., 2009; Valensise et al., 2017), surrounded by important mountain ranges (Tertulliani et al., 2011) (Fig.1, panel A and C).
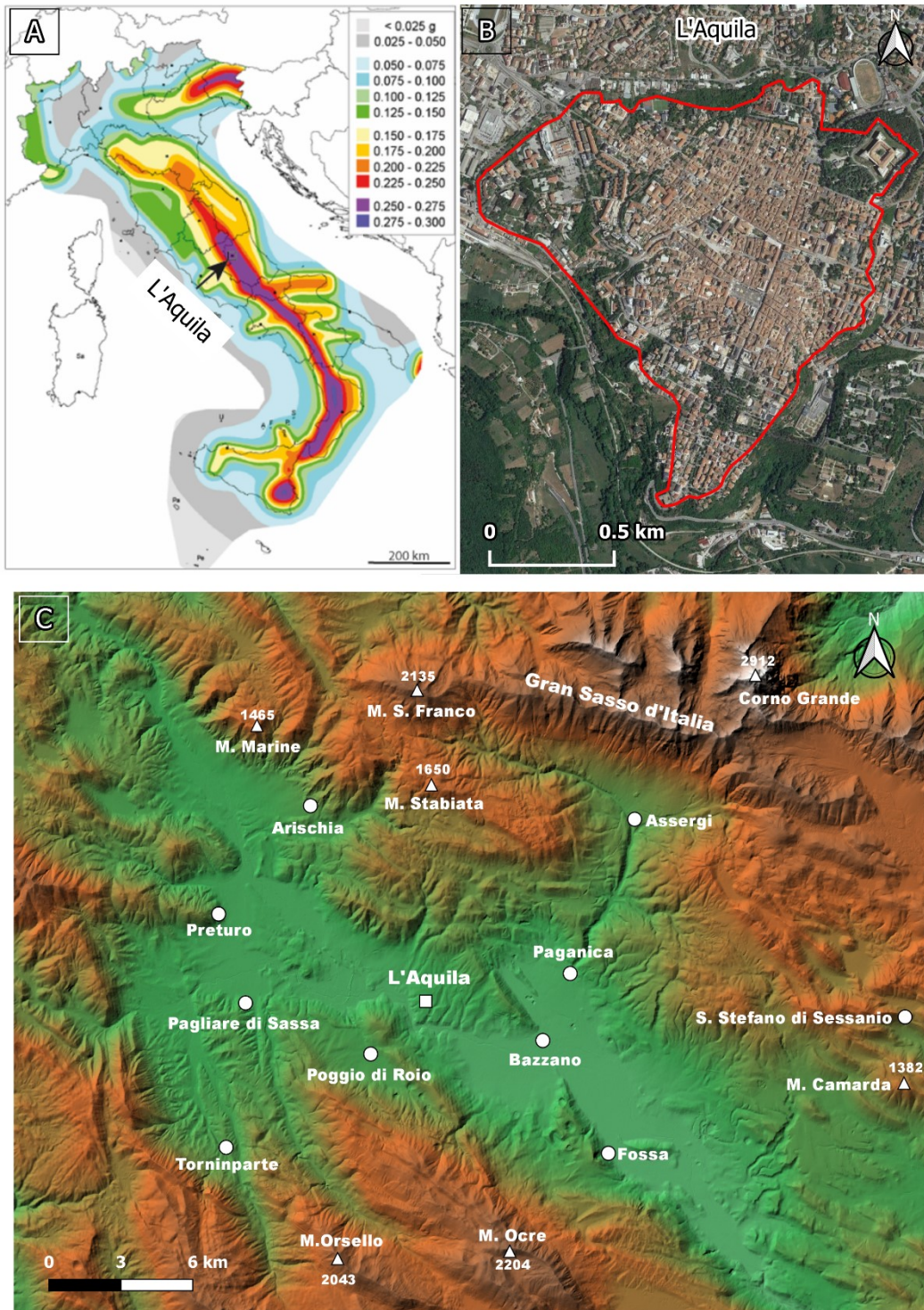
Figure 1: Map of the Seismic Hazard of Italy (panel A), showing peak ground accelerations (g) that have a 10% chance of being exceeded in 50 yr (Meletti and Montaldo, 2007). The study area is located in central Italy, in a high seismic risk zone.

In the panel B, a satellite image of the center of L'Aquila, enclosed within the medieval walls (in red), is shown. In panel C the position of the city surrounded by significant mountain ranges is depicted.

The city's buildings exhibit several kinds of structures. The downtown area is predominantly characterized by stone masonry buildings, while the outer areas are mostly defined by more contemporary structures made of reinforced concrete and masonry. This diversity reflects the urban evolution of the city, which has been affected by numerous strong earthquakes over time. Historical sources indicate that the most significant earthquakes were those in November 26, 1461 (which led to the destruction of medieval buildings) and February 02, 1703 (A. Tertulliani et al., 2012; Andrea Tertulliani et al., 2009) (locate at Pizzoli,15 km northwest of L'Aquila and with a macroseismic magnitude of M_w 6.7 (Gruppo di lavoro CPTI, 2004)). The 1703 earthquake, which marked the birth of the current urban plan (Tertulliani et al., 2011), ranks as one of the most devastating seismic catastrophes in Italy's history. The impact of the 1703 earthquake extended over an expansive area, covering roughly 52,000 square km, spanning regions from northern to southern Italy, encompassing areas from Bologna to Naples. Even isolated, minor tremors were reported in distant locations like Milan and Venice (Locati et al., 2021; Rovida et al., 2020). The event on February 2nd, 1703, forms part of a broader seismic sequence, including two other significant events: the first, with its epicenter in Norcia on January 14, 1703, registered a magnitude of 6.92, and the second, occurring on January 16 of the same year with an epicenter in Montereale, had a magnitude of 6.0 (Locati et al., 2021; Rovida et al., 2020). The earthquake of 1703 decimated 44 villages within an area spanning approximately 19,000 square kilometers, resulting in an estimated death toll of around 6,000 (Antinori, 1971). In L'Aquila, the city closest to the epicenter (approximately 12 kilometers away), it recorded an MCS intensity level of roughly 9. Indeed, every building in the city sustained damage, with at least 35% of buildings collapsing entirely.

After the 1703 earthquake, in Rome three arches of the Colosseum's second-order collapsed, and there was damage to sections of the already poorly maintained Aurelian

walls. Additionally, cracks and structural damage occurred in the domes and vaults of several churches. The seismic event occurred on April 6, 2009, when a M_w 6.3 earthquake (Ameri, G., Massa, M., Bindi, D., D'Alema, E., Gorini, A., Luzi, L., Marzorati, S., Pacor, F., Paolucci, R., Puglia, R. & Smerzini, 2009; Amoruso & Crescentini, 2009; Anzidei et al., 2009; Atzori et al., 2009; Chiarabba et al., 2009; Tallini et al., 2019, 2020) severely damaged and destroyed most of the buildings in the historic center (Atzori et al., 2009; Tallini et al., 2020; Walters et al., 2009). It is estimated that 47% of the buildings suffered moderate damage, while 20% experienced severe damage and over 40,000 individuals were rendered homeless, churches and monuments were heavily struck (Tertulliani et al., 2011). Following this seismic event, a building-by-building damage assessment, resulting in the production of a damage map, was carried out (Tertulliani et al., 2011). The survey was carried out under the European Macroseismic Scale (EMS98), to evaluate the local macroseismic intensity. Specific damage patterns were observed and attributed to a combination of geological factors and building vulnerability (A. Tertulliani et al., 2012). The most affected areas were the southern and southwestern sectors. The objective of this study consists of a in-depth analysis A-DInSAR deformation maps, in order to evaluate its potential use in predicting seismic effects at the scale of individual buildings, mapping high-susceptibility areas, and mitigating seismic risk in urban contexts.

To this aim, our analysis is mainly addressed at characterizing post-seismic subsidence/uplift motions as well as at individuating some potential controlling or correlated factors, such as, building damage intensity, reconstruction interventions, building typology, etc. For this purpose (i) deformations detected by A-DInSAR analyses of Cosmo-SkyMed data between 2010 and 2021 in the descending orbit have been compared with the seismic damage map for 2009 (Tertulliani et al., 2011) and with the damage map for 1703 (Colapietra, 1978); (ii) ground and building velocities have been examined, in order to evaluate the possible impact of building's vulnerability and reconstruction efforts on the LOS (Line of Sight) deformations; (iii) Geostatistical Analysis has been carried out to achieve a spatial characterization of deformations affecting the study area and (iv) statistical and cluster analyses have been performed in order to identify common trends in displacement time series of monitored points. This

analysis was divided into the phases of data pre-processing, cluster analysis and inferential analysis. Data pre-processing was aimed at improving the quality of the data associated with each PS, as well as removing seasonal effects. The cluster analysis was aimed at identifying common subsidence/uplift trends, so as to be able to remove from the data sets time series showing anomalous trends, very different from that common to the class studied. These procedures allowed to carry out an inferential statistical analysis on well-selected and quality improved data sets.

2. Materials and Methods

2.1. Macroseismic data

After the 2009 earthquake, following the guidelines of the EMS98 [37], a detailed building damage survey of L'Aquila historic center (located within the medieval city wall), was carried out, in which were classified and plotted into a geo-referenced map 1710 buildings (Tertulliani et al., 2011). The EMS98 [37] takes into account an inventory of building types, ranked according to their seismic vulnerability, i.e., susceptibility to be damaged by an earthquake. In addition to vulnerability and damage, the database includes data on the area, perimeter, and height of each building.

The buildings, grouped in vulnerability classes, are displayed in Figure 2 and summarized in Table 1. Vulnerability is expressed with a letter from A to D (where A represents the maximum vulnerability and D the minimum) and to each building was assigned a grade of damage (DG). The survey resulted in the production of a damage map (Figure 2), that classifies buildings using a scale ranging from DG0 (no damage) to DG5 (collapsed). Table 2 describe DG under the EMS98.

EMS Scale – Vulnerability class

EMS Scale

Vulnerability class

- A
- B
- C
- D
- Churches & Monuments
- Uncensused

0   0.25   0.5 km
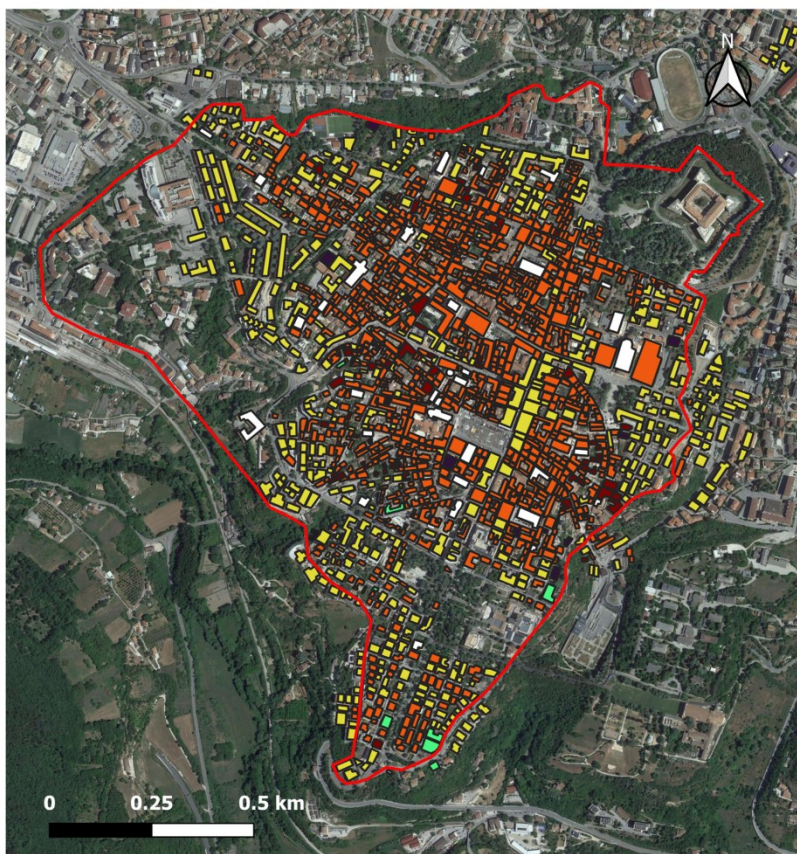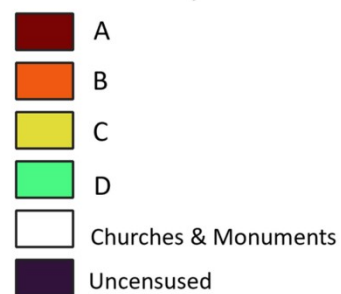
EMS Scale – Damage grade (2009 earthquake)

Damage grade

- 0
- 1
- 2
- 3
- 4
- 5
- Not Surveyed
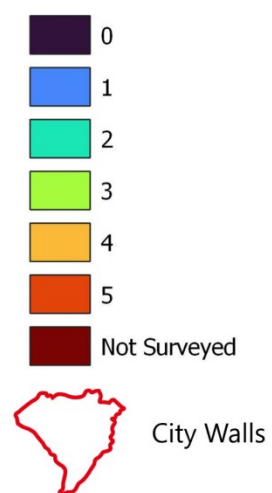
City Walls

0   0.25   0.5 km
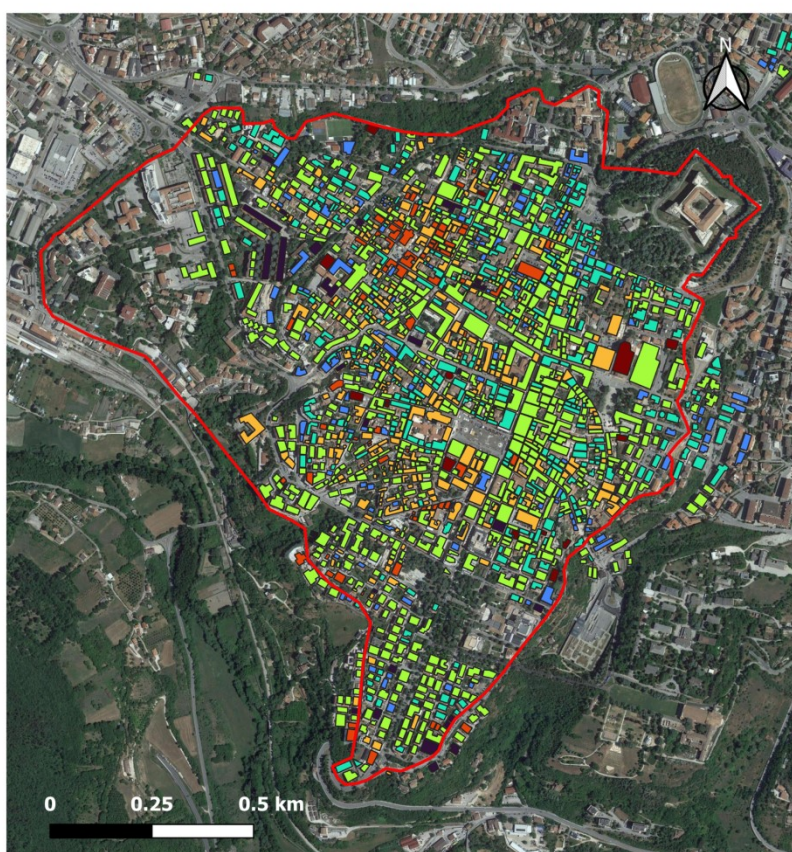
Figure 2: The map on the left displays the vulnerability classification of buildings, while the one on the right illustrates the damage grade resulting from the 2009 earthquake in the historic center of L'Aquila. These maps are the outcome of a detailed building survey carried out by (Tertulliani et al., 2011) following the criteria of the European Macroseismic Scale 98 (EMS98). For a detailed explanation of the vulnerability classes and damage grades, please refer to Tables 1 and 2, respectively.

Table 1. Description of the vulnerability classes related to building type identified in L'Aquila downtown, from (Tertulliani et al., 2011). The number of buildings in each class is reported (modified from (Tertulliani et al., 2011)).

Type of building	Characteristics	Vulnerability class (EMS 98)	Number of buildings
Traditional dwellings. Two to four stories	Masonry construction in field, simple stone, non-manufactured. General bad state of preservation	A	71
Traditional buildings. Two to four stories	Groundwork of masonry in simple stone or manufactured stone units. Many old buildings among them. Presence of tie-rod connections. Variable state of preservation	B	1127
Historical edifices. Two to four stories.	Massive stone, or manufactured stone units. Variable state of preservation	B – C	

Residential buildings (modern). Two to six stories	Masonry constructions in manufactured stone units. Brick with RC floors buildings. RC structure without anti-seismic design. Generally in a good state of preservation	C	504
Public buildings and/or residential buildings (very recent)	RC/steel structure with anti-seismic design. Generally in a good state of preservation	D	8
Monumental buildings (churches, towers etc..)	Masonry construction in field, simple, or massive stone Most of these buildings are several hundred years old. Variable state of preservation. Irregular ground plan	Churches and Monuments	34

Table 2. Description of the damage grade related to building type identified in L'Aquila downtown from (Tertulliani et al., 2011). The number of buildings in each class is reported (modified from (Tertulliani et al., 2011)).

Damage grade	Masonry buildings	RC buildings	Number of buildings
0 No damage			30
1 Negligible to slight Damage	Hair-line cracks in very few walls, fall of small pieces of plaster only, fall of loose stones from parts of buildings in very few cases	Fine cracks in plaster over frame members or in walls at the base, fine cracks in partition and infills[1]	144
2 Moderate damage	Cracks in many walls, fall of fairly large pieces of plaster, partial collapse of chimneys, slipping of roof tiles	Hair-line cracks in columns and beams, cracks in partitions and infill walls, fall of brittle cladding and plaster, falling mortar from the joints of wall panels	386
3 Substantial to heavy damage	Large and extensive cracks in many walls, general falling of roof tiles, chimneys fracture at the roof line, failure of individual non-structural elements	Large cracks in partition and infill walls, failure of individual infill panels, cracks in columns and beams with detachment of pieces of concrete, buckling of reinforced rods	792
4 Very heavy	Serious failure of walls and roofs,	Large cracks in structural elements, damage to the joints	268

Damage	partial structural failure	of the skeleton, destruction of concrete floors, protrusion of reinforcing rods, tilting of columns	
5 Destruction	Very total or near total collapse	Very total or near total collapse	75

The map of earthquake damage from the February 2, 1703 earthquake, on the other hand, is the result of an extensive effort to collect historical sources conducted by Colapietra in 1978 (Colapietra, 1978). In this map, shown in Figure xx, buildings are categorized into three classes: undamaged, damaged, and destroyed. For each damage class, the graph in Figure xx presents both the number of buildings falling into that category and the corresponding percentage. In addition to the Colapietra map (1978) (Colapietra, 1978) used in this article, a wealth of information regarding the damage caused by the 1703 earthquake can be found in Tertulliani and Graziani (2022) (Andrea Tertulliani & Graziani, 2022) (and references therein), as well as in various other works (Tertulliani et al., 2011; A. Tertulliani et al., 2012).

collapses and very heavy damage

partial collapses; large and extensive cracks

light or no damage

Damage due to February 02, 1703 earthquake

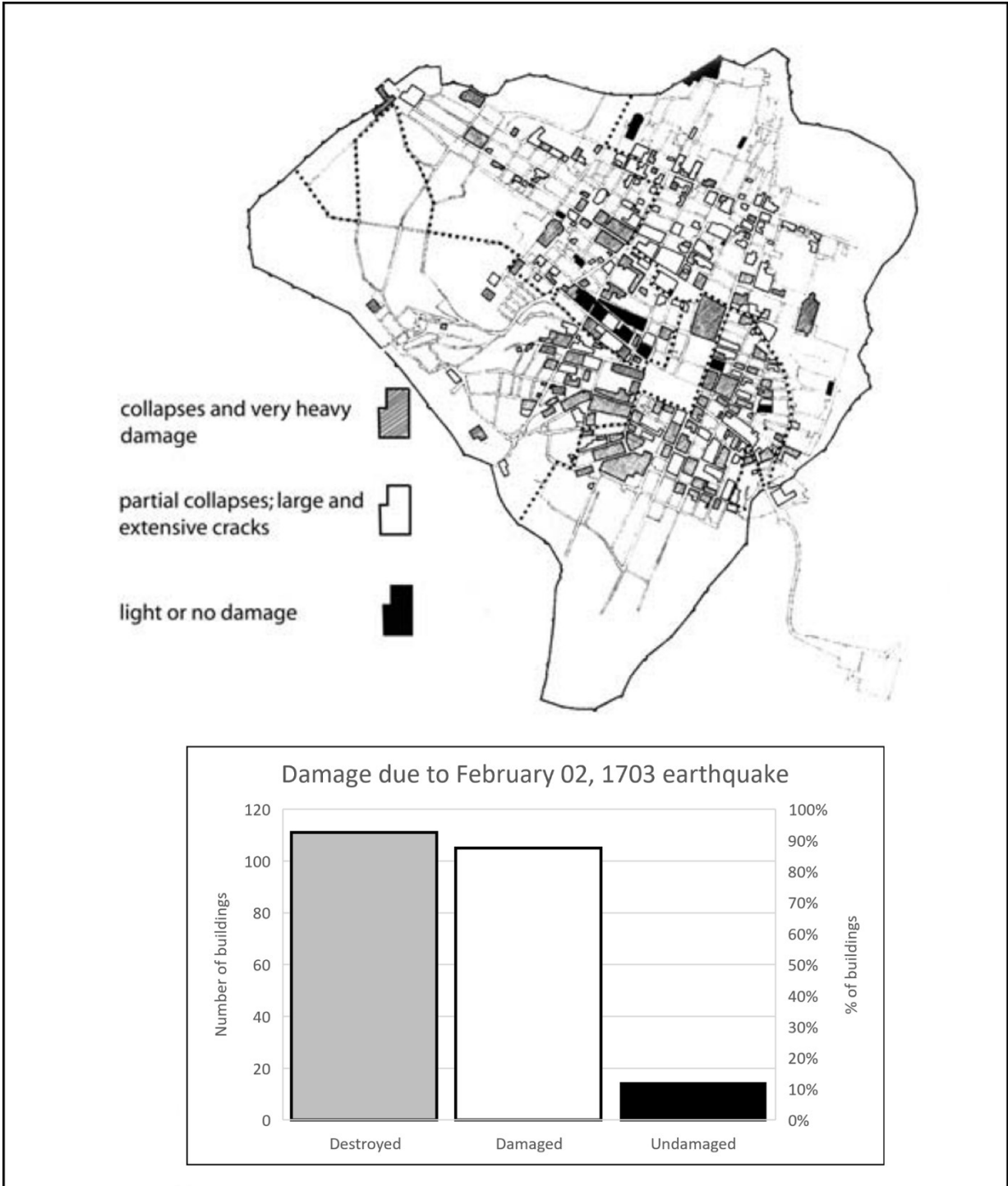Figure 3: Map of the distribution of damage due to the 2 February 1703 event (modified by Tertulliani et al., 2012 (A. Tertulliani et al., 2012), from Colapietra, 1978 (Colapietra, 1978)). This earthquake was the third event of a long and strong seismic sequence that

hit central Italy. The 2 February 1703 earthquake has been located 15 km northwest of L'Aquila, with a macroseismic magnitude of Mw 6.7

2.2. A-DInSAR data

Cosmo-SkyMed images were processed through InSAR technique. By using a long time series (2010-2021) of images acquired over the same area, Advanced Differential Interferometric Synthetic Aperture Radar (A-DInSAR) allows for identifying of past or ongoing deformation processes over time and space with millimeter-level accuracy. This characteristic makes the technique one of the most powerful tools for studying ground deformations and estimating the temporal evolution of displacements during the investigated period (Alessandro Ferretti et al., 2001; Kampes, 2006). The COSMO - SkyMed constellation, developed by the Italian Space Agency (ASI), is a high-resolution Synthetic Aperture Radar (SAR) satellite constellation. It provides detailed imaging of the Earth's surface with fine resolution, enabling the detection and analysis of small-scale features. The SAR sensors operate independently of weather conditions, ensuring all-weather imaging capability. With multiple satellites (currently 6 in operation: 4 from the first generation and 2 from the second generation) that orbit at a height of 619.6 km and orbital inclination of 97.86°. All satellites are equipped with high-resolution X-band radar (3.1 cm of wavelength). The radar sensor of the Cosmo SkyMed satellite is capable of functioning in various data acquisition modes. These modes include spotlight, which concentrates on a specific area covering a few square kilometers and provides observations with a spatial resolution of up to one meter. There's also the Stripmap mode, which continuously observes a linear swath of the Earth's surface, delivering a spatial resolution of 3x3 m. Lastly, the ScanSAR mode can cover a broader region spanning up to 200 km (Figure 4).
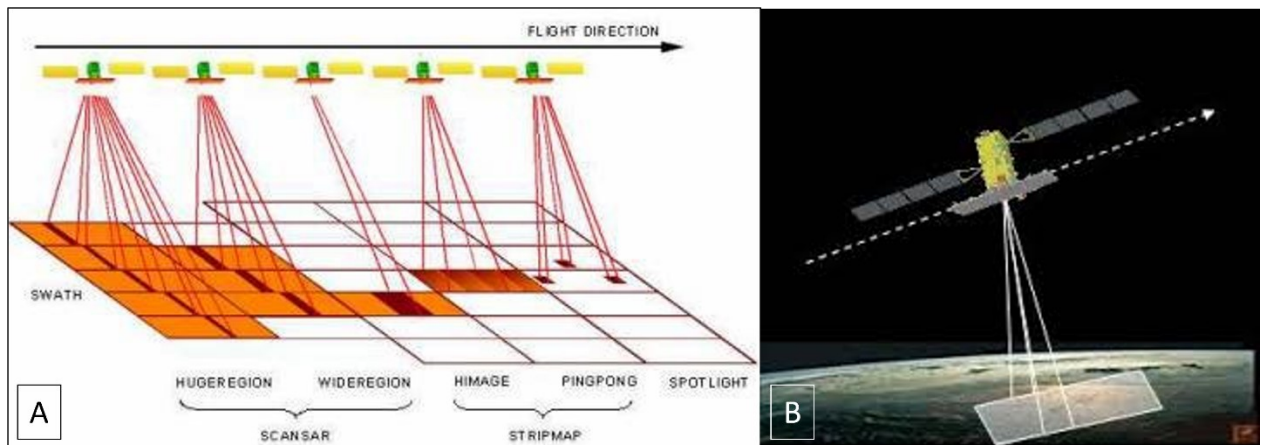
Figure 4: SAR operative acquisition modes. A) type of acquisition data modes available for Cosmo-SkyMed radar sensor. B) Stripmap mode: the right-looking satellite observes a linear area of the Earth's surface, providing a spatial resolution of 3x3 m (modified from ((ASI), 2021)).

In the context of this study, we employed Stripmap HIMAGE images due to their superior geometric and temporal resolution characteristics, which are readily available in the ASI archive. When operating in Stripmap mode, the Synthetic Aperture Radar (SAR) instrument maintains a consistent set of parameters throughout the data acquisition process. The antenna is configured to emit a fixed beam with a constant azimuth and elevation direction. The satellite's orbital motion naturally ensures coverage along the track direction.

COSMO -SkyMed offers frequent revisits, enhancing temporal resolution. However, due to its dual civilian and military purpose, there are some temporal gaps. In this case study, only the descending orbit geometry could be utilized. Ascending images were not employed in our study due to their insufficient level of detail for the conducted analysis. In fact, compared to the descending ones, they had lower coverage and limited temporal continuity. The Italian Space Agency (ASI) provides free access to COSMO-SkyMed data for research purposes.

For this case study, a total of 161 Single Look Complex (SLC) images acquired in the descending orbit geometry by COSMO-SkyMed satellites from April 14, 2010, to November 30, 2021, were utilized (Figure 5). In this work, we utilized the SARPROZ software for the A-DInSAR analysis. The PSI algorithm implemented in SARPROZ, the SAR processing tool developed by Daniele Perissin (Perissin et al., 2011) consists of the following processing steps. Initially, it involves selecting a reference image and defining a star graph to establish connections between images based on temporal and normal baseline parameters. Next, SLC image co-registration is performed on the master area, followed by the generation of a reflectivity map. Ground Control Points (GCPs) are then selected for geocoding the radar images to the ground. Differential interferograms

are computed using the synthetic Digital Elevation Model (DEM) for image pairs exhibiting a high level of coherence. Furthermore, preliminary parameter estimation, including average velocity, non-linear displacements, and residual height, is carried out on the Persistent Scatterers Candidates (PSCs). Finally, atmospheric phase screen removal and the final parameter estimation are performed on all pixels.

Table 3: A-DInSAR analysis characteristics.

Master area dimensions	4000 x 4000 px (32 km^2)
Master image	6 April 2016
Satellite heading angle	168.65°
Satellite incidence angle	32.20°
Reference point selected	LAT: 42.363137 LONG: 13.368094
Digital Elevation Model used	TinItaly 10m resolution

We divided the A-DInSAR data into two categories: ground points (hereinafter GP) and building points (hereinafter BP) to analyze them separately and identify possible differences between these two categories of PSs.

Subsequently, to estimate the average deformation velocity of buildings with different levels of damage incurred during the 2009 earthquake, we clipped the interferometric dataset using the building boundary polygons, classified by the intensity of damage they suffered into five classes, ranging from Damage Grade (DG) 1 to DG 5 (in accordance with the EMS98 guidelines). For each group, we calculated the average values of satellite-recorded displacements. For all PS (Persistent Scatters) located on buildings with DG 3 or higher (damage classes with higher deformation velocities along the LOS), we further analyzed the interferometric dataset by distinguishing between

reconstructed buildings and those that have undergone restoration. For this purpose, we accessed a database that provides extensive information about the buildings located in the L'Aquila downtown. This database offers various details, including the kind of undertaken intervention, the dates of commencement and construction completion works, the amount of funding allocated for maintenance or reconstruction, and other relevant information. The database is accessible at the Gran Sasso Science Institute website (Institute, n.d.).

Indeed, we carried out a similar analysis by juxtaposing the satellite-identified deformations with the buildings affected by the 1703 earthquake. In order to compare the SAR deformation with the damage distribution for the 1703 earthquake, the damage map from Colapietra (1978) (Colapietra, 1978), in Figure 3, was georeferenced in QGIS. We clipped the PS map using boundary polygons corresponding to buildings classified as undamaged, damaged, and destroyed. Subsequently, we computed the average cumulative displacement for each of these distinctive categories.
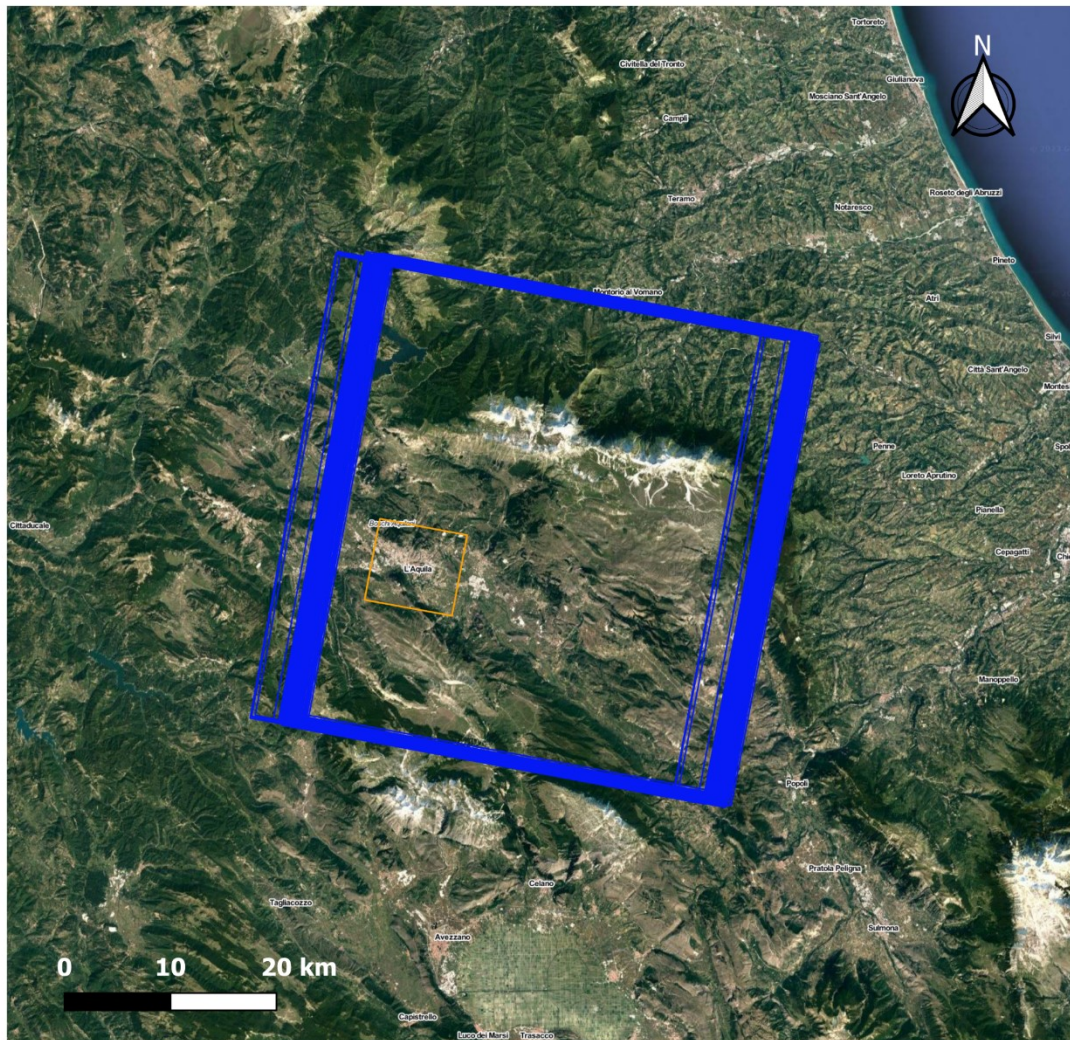
Figure 5: in blue the footprints on descending orbital geometry of the COSMO-SkyMed images and in orange the master area analysed.

2.3. *Geostatistical analysis*

To achieve a spatial characterization of deformations affecting the study area, Geostatistical Analysis has been performed by calculating the variogram of the yearly average velocities of the monitoring points (each monitoring point represents a Persistent Scatter – PS - in the Geostatistical Analysis). A variogram (Diggle, P. J. and Ribeiro, 2007) is a function used in geostatistical analysis to describe the spatial variability of data. Denoting the average velocity (mm/year) of a generic PS by z_i, such

diagram shows the variance of the difference (z_i – z_j) of two points placed at a distance L in ordinates, as a function of the latter (in abscissae). In the most common geostatistical models, the considered variable (in our case, subsidence/uplift rate), if associated with a stochastic spatial process, shows a greater correlation with the closest points (and therefore a lower variance of the differences) than with the more distant. Therefore, in such cases, the variogram appears as an increasing curve. Fig. 6 provides an example (which is not based on our field data) of the expected curve [e.g., 43].
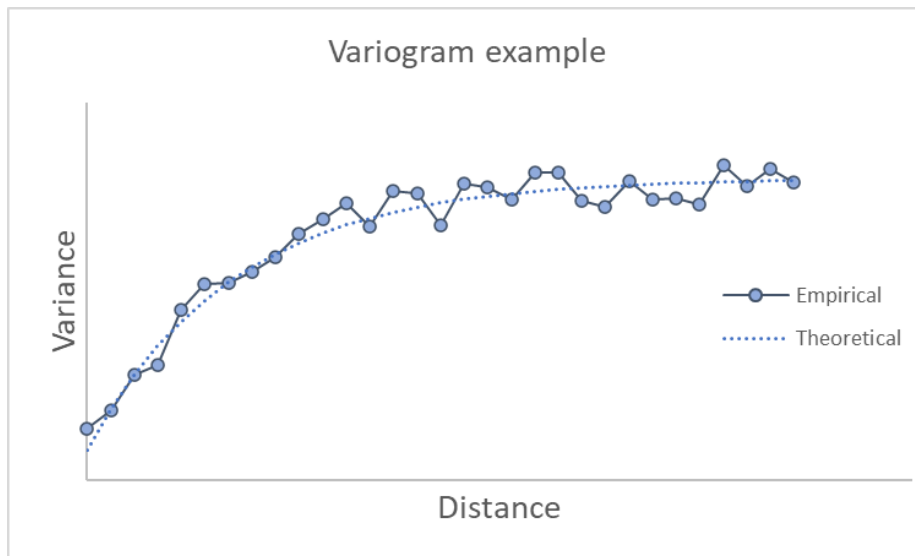
Figure 6: Schematic representation of a typical variogram.

2.4.   *Trend recognition and cluster analysis*

In order to assess whether or not PSs associated with different classes of building damage and category (ten classes) follow different preferential trends, as well as identify the related pattern, a cluster analysis was carried out. Denoting by *yj(t)* the vertical displacement time series of the j-th monitored Ps, the purpose of this analysis was to identify, within our data sets, curves *yj(t)* which exhibit analogous shape or pattern. This allowed us to separate time series associated with subsidence or uplift, as well as to remove from data sets of each class, time series showing anomalous trends, very different from that common to the class studied. The cluster analysis preceded the inferential statistical analysis, aimed at calculating the PS average velocity, for each

class, as well as the related confidence intervals, to confirm or exclude any possible correlation with building damage intensity and/or with reconstruction interventions (Sects. 3.1.3. and 3.1.4.). Therefore, the use of cluster analysis provided the dual advantage of (i) identifying preferential subsidence/uplift patterns associated with each building class studied and (ii) allowing subsequent inferential statistical analyses based on selected/homogeneous samples, i.e., from which anomalous time series were removed. The cluster analysis was performed according to two different variants of the k-means algorithm (e.g., Ertel; Bishop (Bishop, 2006; Ertel, 2011); Appendix 1). The k-means algorithm is a Machine Learning criterion able to identify groupings (clusters) of elements in a given metric space (which is not to be confused with the Euclidean space, but which denotes a Cartesian system made up of variables of any nature). In our case, data consist of vectors with 158 components (i.e., 158 vertical displacement measurements recorded, for each PS, over about 12 years), each associated with a point in the monitored area. Each time series (and PS) is also associated with an average velocity value. In these hypotheses two curves $y_j(t)$ (which are actually made up of a discrete set of points, i.e., the above mentioned vectors) are considered coincident if the arrays $y_j(t)$ have all the components equal, "close" if the differences between the components are moderate and "distant" if these differences are significant. Therefore, two arrays which are close according to this criterion can be associated (and frequently are in our data set) with two points of the territory that are also geographically distant and vice versa. Two variants of the k-means algorithm (hereafter conventionally named method I and method II) have been used in this work, which differ in the definition of the cluster midpoint and in the distance. Method I is an ad hoc formulated variant for our data set, in which the distance between two vectors is defined as ($D = 1 -$ Correlation($y_j(t)$, $y_k(t)$)), an element is considered to belong to a cluster if D is less than a predetermined threshold value (e.g., $D < 0.2$) and the center of the cluster is given by the vector for which the sum of the distances from all its other elements is minimum. Note that, according to this definition, two vectors $y_j(t)$ and $y_k(t)$ have zero distance not only if they have equal components but also if ($y_j(t)$ = const. $y_k(t)$, $\forall t$), i.e., if they are associated with curves showing the same shape although with different displacement values. Method II follows a more usual criterion in which the distance is calculated as a

Euclidean distance, in the 158-dimensional space $\left(D_{jk} = \sqrt{\sum_n(y_j(n) - y_k(n))^2}\right)$, and the midpoint of the cluster is the barycentre (centre of mass) in that space, i.e., the vector y(t)* whose components are equal to the arithmetic average of those of the elements of the cluster itself. Furthermore, an element is considered to belong to the cluster if the distance from the midpoint is less than a desired threshold value and not to belong to it, otherwise. Fig. 7 illustrates examples of curves near and far from midpoint. The threshold value used was such as to allow a not strong selection of the PSs, i.e. such as to discard only those curves that exhibited an anomalous trend, strongly different from that of the midpoint. As, according to this approach, two vectors are at zero distance only if the corresponding curves coincide, and since we are instead interested in comparing the displacement-time curves in terms of shape (e.g., local inflections and slopes) rather than net displacements, the components of each vector yj (t) have been preliminarily normalized (or re-scaled) by dividing by the mean subsidence/uplift rate (expressed in mm/year) corresponding to each vector.
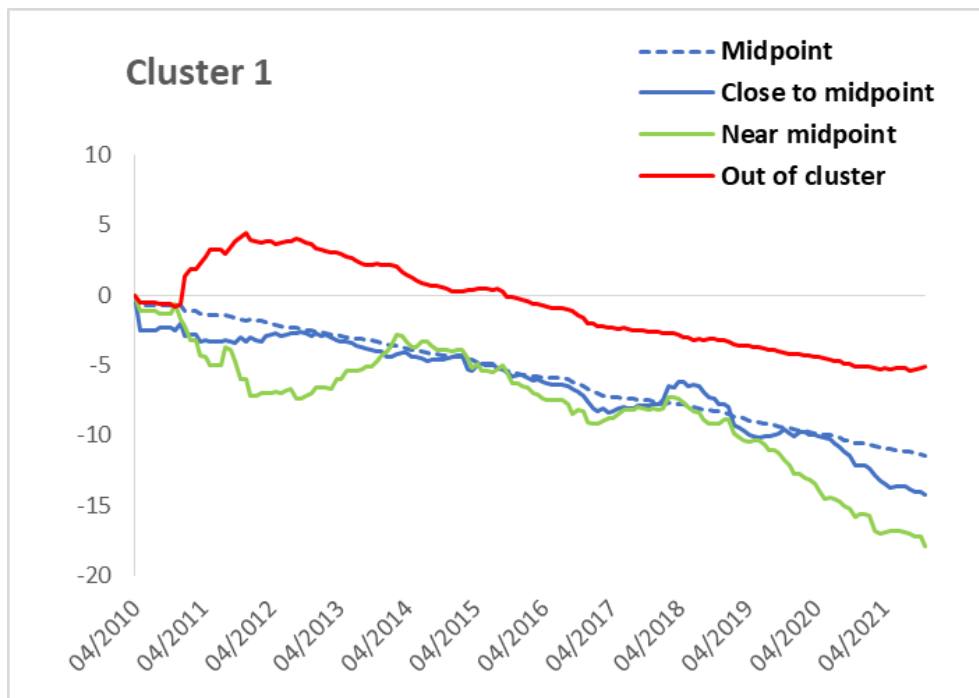

Figure 7: Example of time series at several distance (see main text for definition) from the midpoint of a cluster. Note that the curve denoted by 'near midpoint', in green color,

has a distance value which is near the threshold defining exclusion from cluster. The curve in red color has distance value greater than such threshold.

Note that the first described algorithm variant provides an element of the dataset as a midpoint for each cluster, which can be viewed as a representative element, whereas the second approach returns a vector (whose components are the average of the corresponding ones of all the other vectors) which in general does not match any of those belonging to own cluster.

The first variant of the k-means algorithm was used to identify, for each data set, the midpoint vectors of two clusters, one associated with subsidence and the other with uplift, which allowed us to analyze the spatial correlation trend between the values of displacement-time curves with the (geographical) distance between monitored points. Instead, in order to recognize common trends between data, it was decided to use the second variant of the k-means algorithm illustrated above, as it follows a more traditional approach whose validity is widely established. The cluster analysis was carried out, in a first phase, assuming that there were three clusters (we recall that in the k-means method the number of clusters to be searched for is a known datum of the problem; e.g., (Ertel, 2011)), nevertheless the results highlighted the occurrence, in each data set, in addition to a cluster of uplift curves, of two others of subsidence ones, which are substantially superimposable and which are probably the result of splitting of a single cluster. Therefore, for all the data sets this algorithm was applied to search for two clusters, one of uplift curves (less numerous) and one of subsidence curves.

2.4.1. *Preliminary data treatments for cluster analysis*

In order to assess whether the subsidence/uplift trend shows systematic variations in correspondence of buildings which have undergone reconstruction interventions or different levels of damage, the dataset has been divided into five categories based on the damage class, which were further divided into two further categories (for a total of 10

categories), i.e., reconstructed and non-reconstructed buildings. The data consist of arrays of 158 vertical displacement values (in mm) for each monitored point, sampled in the time interval from April 14, 2010 to November 30, 2021, at rather regular but not equally spaced time intervals. For each site, the data is presented with a noise that confers a certain irregularity to the displacement-time curves. This noise is the effect of multiple competing phenomena, such as measurement inaccuracy and seasonal alterations. The latter may likely be due to seasonal variations in the aquifer, as well as other effects of climate variations, including thermal expansion of buildings. The study of seasonal oscillations, although very interesting, does not fall within the scope of the present study and will be the subject of future research. Therefore, in order to achieve data distributed at regular time intervals, to mitigate the disturbance, as well as remove seasonal variations, each array was preliminarily regularized by performing a time average as follows: starting from April 14, 2010, the vertical displacement value is calculated every 26 days as the average of the values recorded in the previous and following six months (when there are any), thus obtaining an array of 158 values at equally spaced time intervals. In order to improve the data set reliability, data showing coherence values greater than or equal to an opportunely chosen threshold (Sect. 3.1.2.) were selected for the most numerous data sets, i.e., those relating to non-reconstructed buildings and, among the reconstructed ones, to the damage class only DG3. For the other kinds of reconstructed buildings, this selection was not applied otherwise it would have made the statistical sample too small.

A further preliminary treatment of the data set consists in normalizing the array values, dividing the components of each vector $y_j(t)$ by the associated average yearly velocity. This allowed to compare displacement vs time curves in terms of local inflections and slopes rather than net displacements or, namely, to compare these curves in terms of shape (i.e., of time trend). The data processing is summarized in Figure 8.
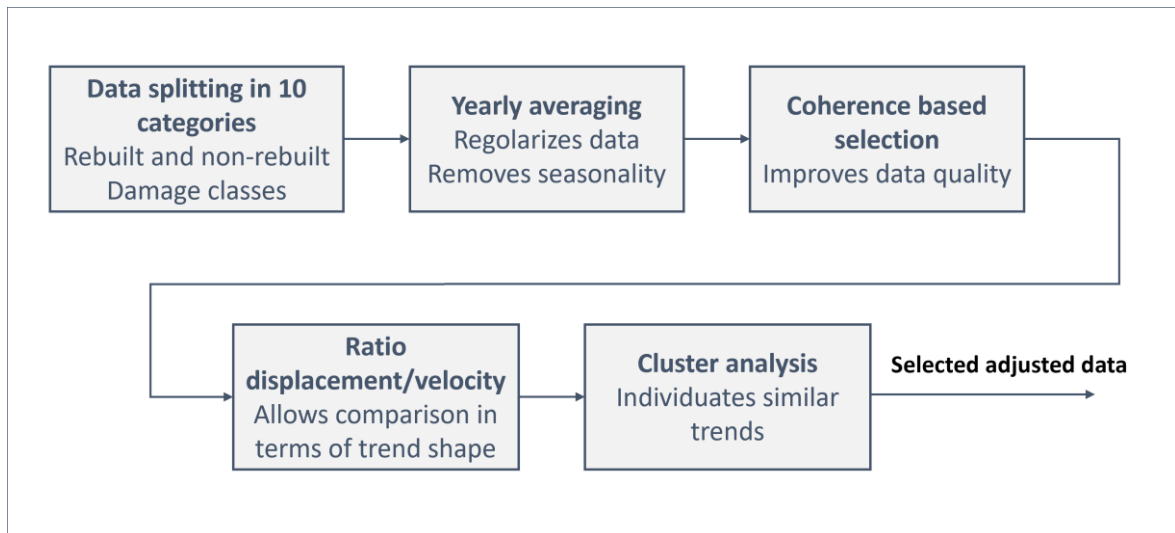
Figure 8: Flowchart illustrating data processing.

2.4.2. Subsidence velocity statistical analysis

In order to confirm or exclude a possible correlation between subsidence velocity and building damage intensity, these velocity values have been grouped by damage category and by kind of intervention (i.e., reconstructed and not reconstructed) of the related buildings, for a total of 10 categories. Then, the 95% confidence intervals, according to the Student's random variable, of the average of velocity values for each category were calculated. This analysis only involved values belonging to the cluster associated with subsidence, previously identified through cluster analysis. This made it possible to compare velocity values belonging to a homogeneous sample, thus discarding any anomalous values, outliers, etc.

3. Results

3.1. Recent and historical earthquake data

The 311711 PSs resulting from the processing of COSMO-SkyMed images are shown in the in Figure 9.
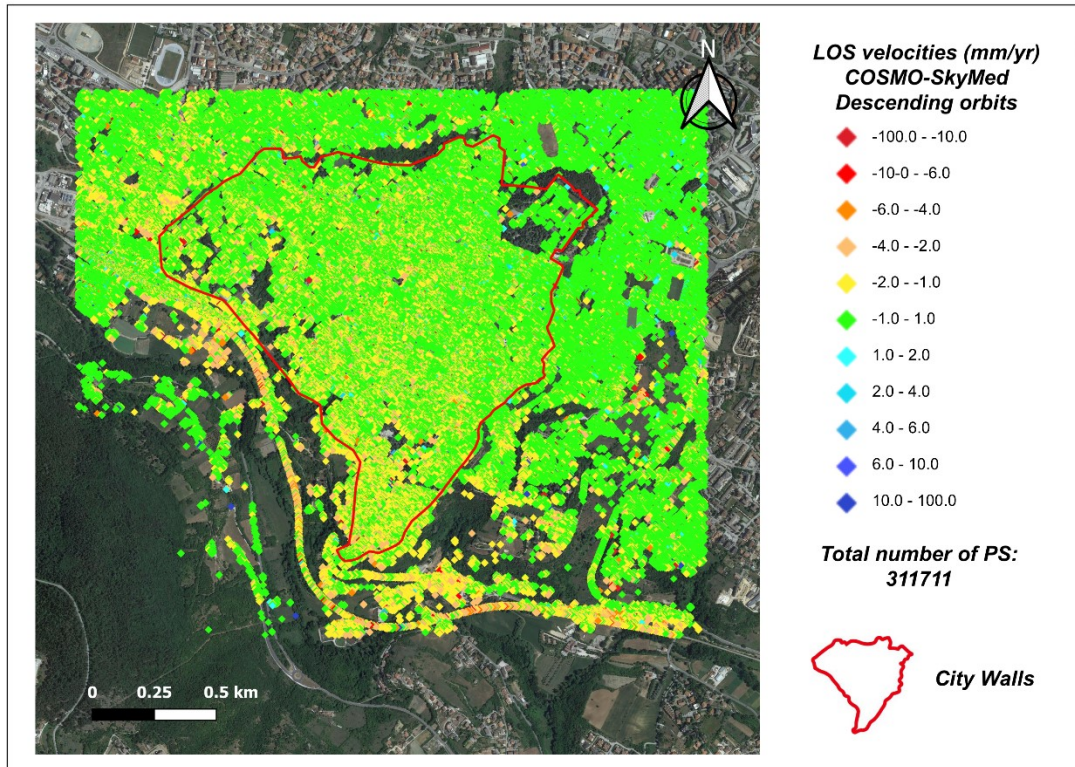
Figure 9: A-DInSAR map resulting from the processing of April 14, 2010, to November 30, 2021 descending orbit images. The study's primary focus, as illustrated in Figure 10, is the area contained within the boundaries of the city wall.

However, the interferometric map was limited to the ancient city, bounded by the medieval walls, which is the specific area of focus in this study (Figure 10). The study area shows relatively slow deformation velocities, typically ranging between +0.5 and - 2.5 mm/year, and seldom exceeding - 5 mm/year. Existing literature (Antonielli et al., 2019; Bozzano et al., 2018) commonly reports measurement accuracy for COSMO-SkyMed datasets to be around ±1.5 mm/year. Nevertheless, as demonstrated by (Bozzano et al., n.d.) and (A. Ferretti et al., 2014) the precision of millimetric measurements depends on factors such as the observed period, satellite revisit frequency, and satellite characteristics, particularly the wavelength.

Thanks to the densely urbanized nature of the natural targets (man-made structures) with high backscattering quality and the extended revisit time of approximately 10 years provided by COSMO-SkyMed, we were able to extract a wealth of information from

our results. This refinement has led to a scale reduction in the displacement rates of PSs, resulting in an instrumental error of approximately 0.3 mm/year.

For this reason, the same A-DInSAR map in Figure 10 is visualized using two different scale (in panel a and b). In the first one green PSs are those with deformation velocity from -1.0 to 1.0 mm/year, in panel b stability value (green PSs) is in the range from -0.5 to 0.5 mm/year. Also, the transition from yellow to red (PSs moving away from the satellite) and from light blue to dark blue (PSs moving towards the satellite) is described, in the two maps, by different velocity intervals. Furthermore, it is emphasised that in the statistical analyses illustrated below, the variability of the average velocities is quantified using 95% confidence intervals. Therefore, the precision of the single measurement assumes a secondary role, as the confidence interval width provides a direct estimate of the aforementioned variability (Sect. 3.1.4.).
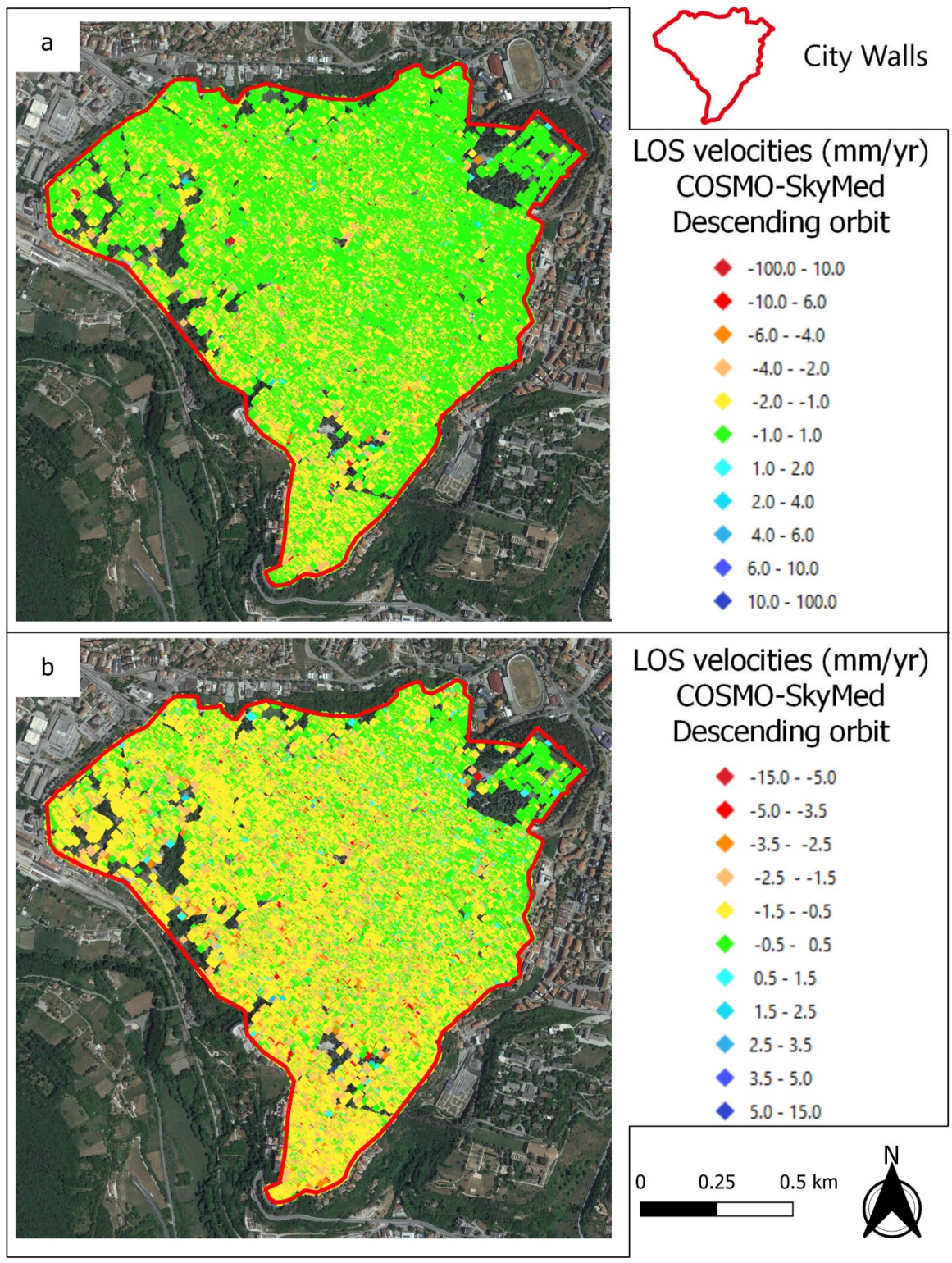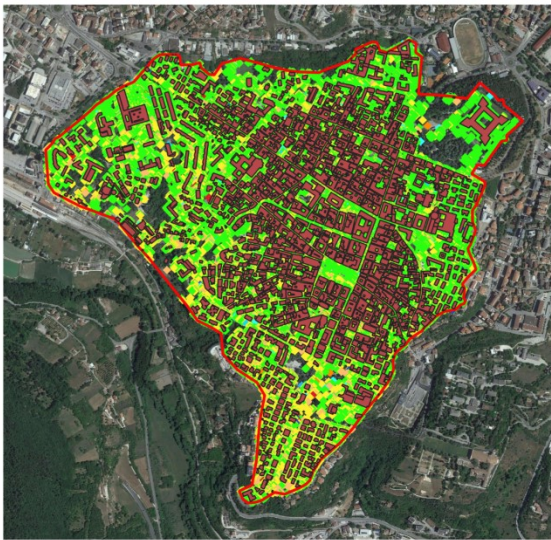
Figure 10: Two different color scales are used to represent the PS points in the study area. In the map in panel a, the range of deformations within the interval of -1.5 to 1.5

mm/year is considered as stable. In panel b, however, the instrumental error threshold is lower, and the PS points in green (stable points) are associated with a deformation of +- 0.5 mm/year.

The interferometric map obtained from the processing of images acquired by COSMO-SkyMed between 2010 and 2021 (Figure 9 and 11) has allowed to analyze the building damage distribution resulting from two seismic events that devastated the L'Aquila downtown: the M_w 6.3 earthquake on April 6, 2009, and the historic earthquake of 1703 with M_w between 6.0 and 6.9 [1,7]. The PS scale in the maps (Figure 9 and 11) ranges from red to blue, where warm colours indicate points moving away from the satellite along the Line Of Sight (LOS), and cool colours indicate points moving towards the satellite, i.e., with positive deformation velocity. Green PSs represent measuring points with displacement velocities ranging between -1 mm/year and 1 mm/year.

The A-DInSAR map highlights more pronounced deformations in the southern and southwestern sectors of the study area. We divided the A-DInSAR data into two categories: ground points (hereinafter GP) and building points (hereinafter BP) to analyze them separately (Figure 11). Of all points, 71.96% are located on the buildings, with the remaining 28.04% being localized scatterers on the ground. The statistical distribution of cumulative displacement values recorded over 11 years along the satellite's LOS was calculated for both types of points. BP show an average cumulative displacement of -9.53 mm with the first and third quartiles respectively equal to -13.57 mm and -4.76 mm. GP displacement values are only slightly different from those of BP, with an average of -9.4 mm, a maximum of -13.37 mm, and a minimum of -4.77 mm.

Ground Points

Building Points

Persistent Scatters

PS on the ground ■ PS on buildings

**LOS velocities (mm/yr)
COSMO-SkyMed
Descending orbits**

City Walls

Buildings

- -100.0 - -10.0
- -10.0 - -6.0
- -6.0 - -4.0
- -4.0 - -2.0
- -2.0 - -1.0
- -1.0 - 1.0
- 1.0 - 2.0
- 2.0 - 4.0
- 4.0 - 6.0
- 6.0 - 10.0
- 10.0 - 100.0

0   0.5 km
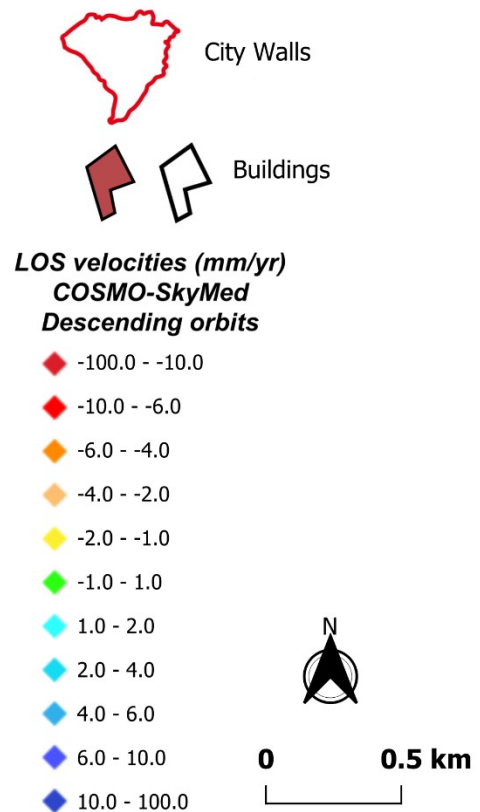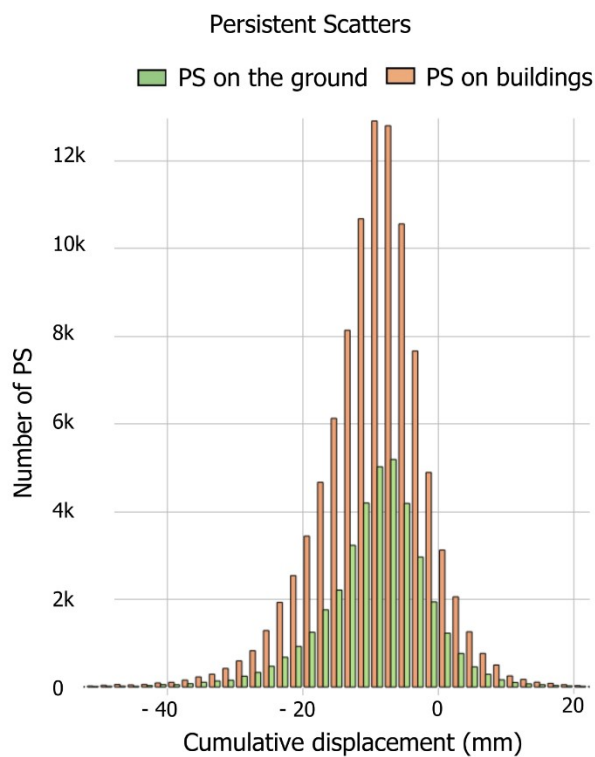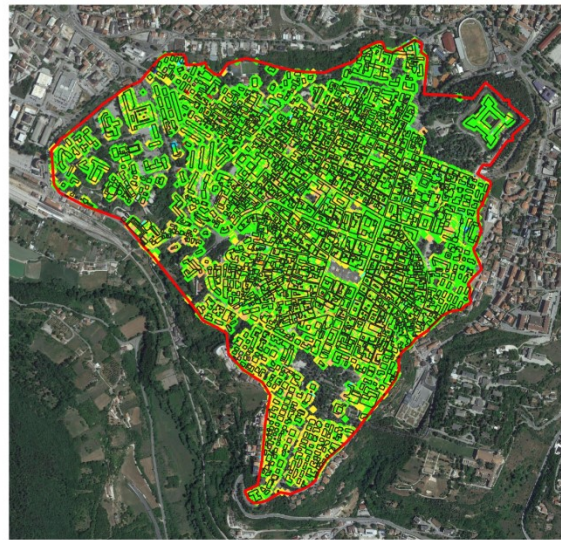
Figure 11: A-DInSAR maps, obtained using COSMO-SkyMed images acquired in descending orbit between 2010 and 2021, are clipped with buildings boundary polygons showing Ground Points (on the left) and Building Points (on the right). Green PSs are considered as stable; yellow-red PSs are moving away from the satellite; cyan-blue PSs

are moving toward the satellite. The buildings in the center of L'Aquila (represented in reddish brown polygons in the Ground Point map and with trasparent with black border polygons in the Building Point map) have been used as a mask to crop the interferometric dataset for a separate calculation of deformations on the buildings (BP) and ground points (GP). In the graph (left down), the x-axis represents the cumulative displacement (in mm), while the y-axis represents the number of Persistent Scatterers (PSs).

We utilized the damage map in Figure 2 to calculate the average velocity and cumulative displacement values recorded by the satellite over the 11 years following the earthquake on April 6, 2009, for buildings with different DG.

Table 4 illustrates the calculated average velocity and cumulative displacement values for buildings ranging from DG1 to DG5. These data provide an overall picture of the correlation between average velocity and damage category. A more quantitative analysis, involving the estimate confidence intervals, is illustrated below, in Section 3.1.3.

Table 4. The table presents the average velocity and mean cumulative displacement computed from the descending COSMO-SkyMed map for each damage class associated with the buildings in L'Aquila's historic center, resulting from the 2009 earthquake.

Damage Grades	Average velocity (mm/y)	Average cumulative displacement (mm)
1	- 0,66	- 7,78
2	- 0,74	- 8,76
3	- 0,83	- 9,79
4	- 0,90	- 10,62
5	- 0,85	- 9,90

The statistical distribution of cumulative displacement values for each damage class is shown in Figure 12. Severe damage, corresponding to a damage level of 3 or higher, was observed in 72.01% of the buildings. Among the severely damaged buildings, the majority (54.3%) belonged to DG3, followed by 14.25% in DG4, and 3.42% in DG5. Buildings with negligible to slight damage (DG1) accounted for 6.55%, while those with moderate damage (DG2) represented 21.41% of the total.

DG 1

DG 2

DG 3

Cumulative displacement on DG 1 buildings

Cumulative displacement on DG 2 buildings

Cumulative displacement on DG 3 buildings

DG 4

DG 5

Cumulative displacement on DG 4 buildings

Cumulative displacement on DG 5 buildings

Measurement points
on buildings with different
grades of damage
(2009 earthquake)

LOS velocities (mm/yr)
COSMO-SkyMed
Descending orbits

-100.0 - -10.0

-10-0 - -6.0

-6.0 - -4.0

-4.0 - -2.0

-2.0 - -1.0

-1.0 - 1.0

1.0 - 2.0

2.0 - 4.0

4.0 - 6.0
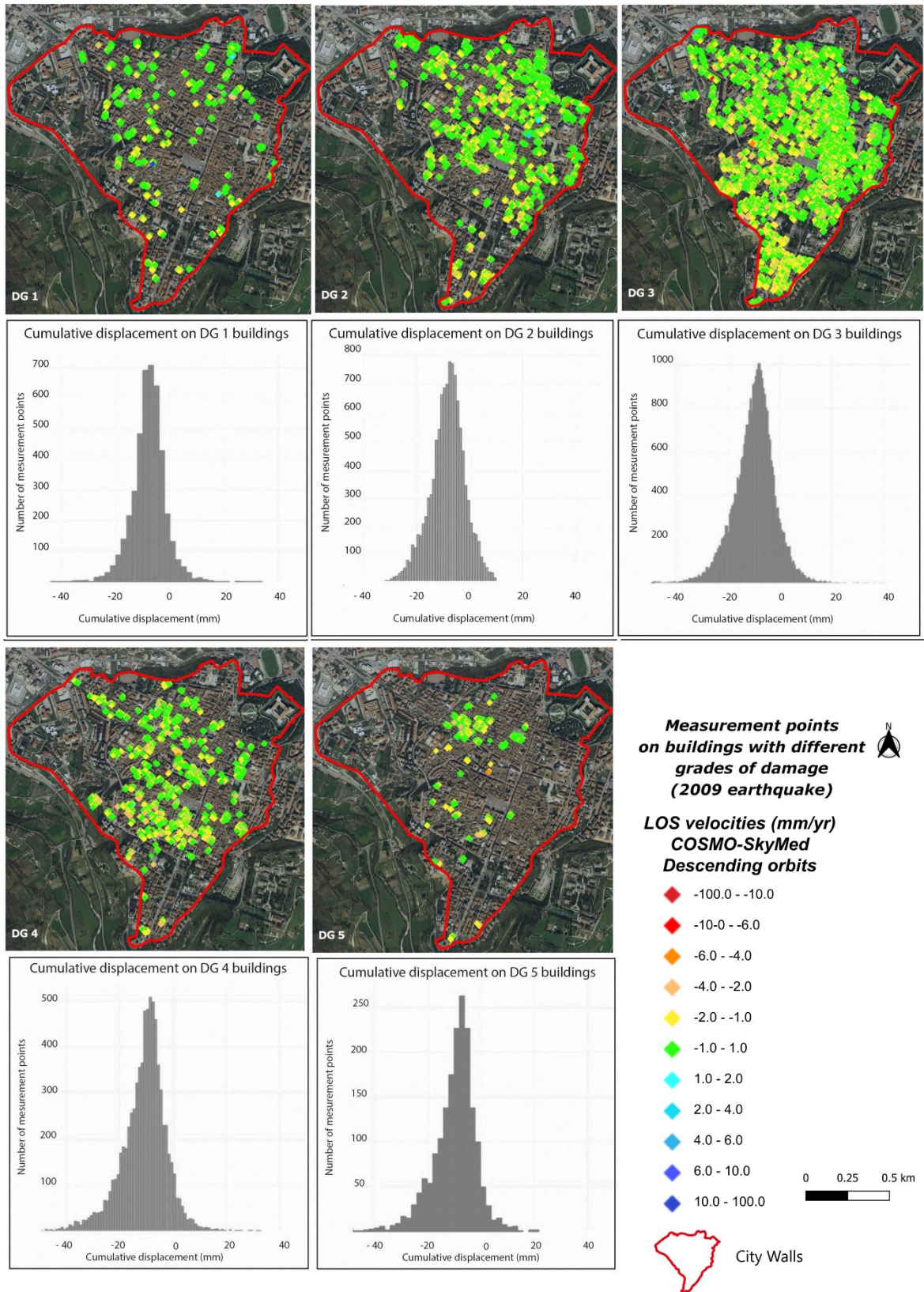
6.0 - 10.0

10.0 - 100.0

City Walls

Figure 12: Statistical distribution of cumulative displacement values for each damage grade. The distribution of damage is depicted by the placement of Persistent Scatterers (PS) in this figure, which are divided into damage classes. Each category is then associated with a Cumulative Displacement/Number of PS graph, which describes the deformations corresponding to the respective damage grade. The colour scale used in the A-DInSAR maps refers to the legend in the figure, noting that negative velocity values correspond to displacements along the satellite's Line of Sight (LOS). Conversely, positive velocities indicate points moving towards the sensor.

The comparison of the vulnerability map of the buildings with the distribution of deformations recorded by the satellite was also performed. The analysis involved the evaluation of average cumulative displacement data recorded by COSMO-SkyMed for each vulnerability class (as described in Table 1). The results have been summarized in Figure 13, panel b.

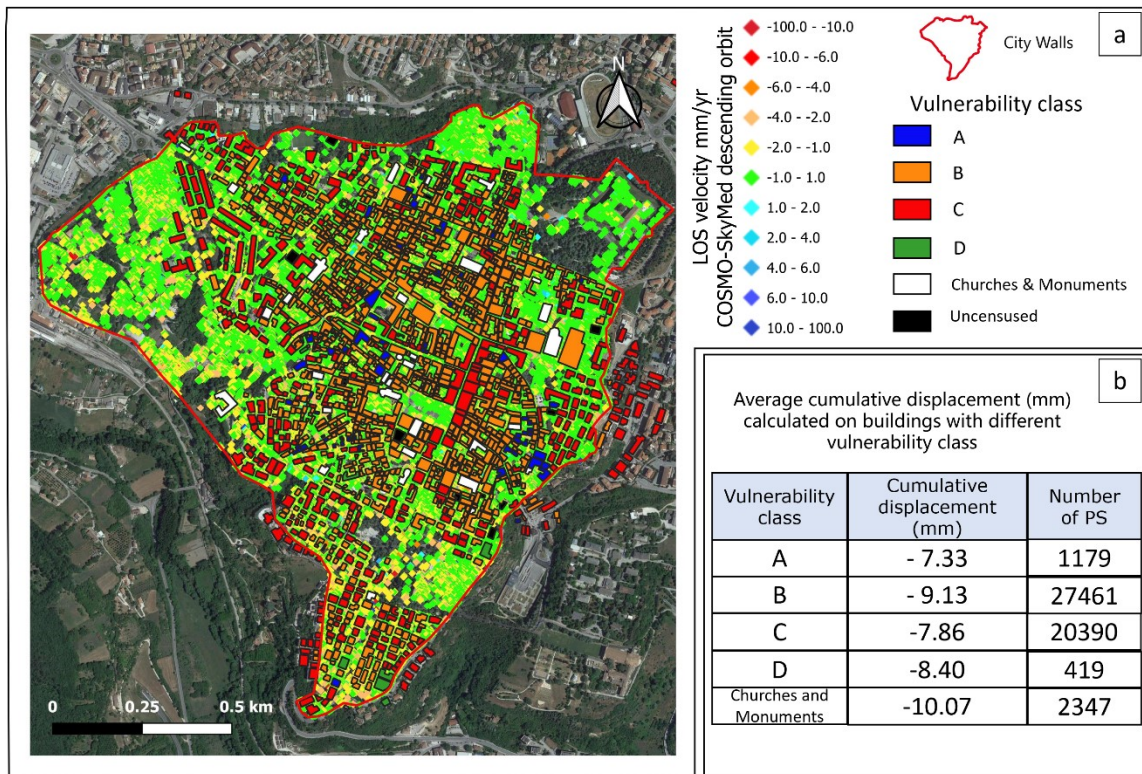| Vulnerability class	Cumulative displacement (mm)	Number of PS
A	- 7.33	1179
B	- 9.13	27461
C	-7.86	20390
D	-8.40	419
Churches and Monuments	-10.07	2347

Figure 13: a) Descending COSMO-SkyMed deformation map with classification of buildings based on their vulnerability. The color scale used in the map for PSs

44

representation refers to the legend, noting that negative velocity values correspond to displacements along the satellite's Line of Sight (LOS). Conversely, positive velocities indicate points moving towards the sensor. b) average cumulative displacement data recorded by Cosmo-SkyMed for vulnerability class. A description of specifical characteristics of each vulnerability class is reported in Table 1.

3.1.1. GeostatisticalAnalysis

In order to characterize the spatial pattern of LOS displacement values (primarily subsidence) for the monitored points, we initially calculated the variogram of the annual average velocities (Diggle, P. J. and Ribeiro, 2007). By way of example, Figure 14 displays the variogram of the most abundant dataset, specifically for buildings with DG3 on non-reconstructed structures. Unlike what is observed in the most widespread spatial process related geostatistical models, in which the variogram appears as an increasing curve, our data exhibit a variogram with an irregular and moderately decreasing trend with distance. The subsidence rates associated with nearby points show little correlation (associated with high variance) whereas the variance shows a slight decrease between values in points increasingly distant from each other. Therefore, usual geostatistical models are not applicable to our data.
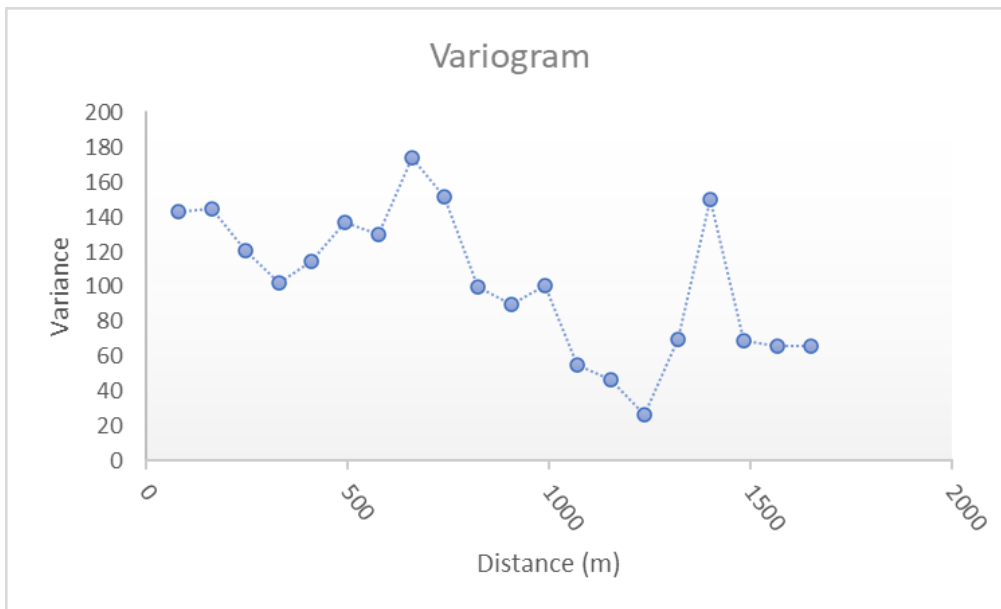
Figure 14: The variogram of the data pertaining to non-rebuilt buildings with damage category 3 is shown. The ordinate axis represents the variance of the differences in average velocity, expressed in mm/year, (z_i - z_j) between two points separated by a geographical distance L, on the abscissa.

3.1.2. Cluster Analysis

For all PS (persistent scatters) located on buildings with DG3 or higher (damage classes with higher deformation velocities along the LOS), we further analyzed the interferometric dataset by distinguishing between reconstructed buildings (approximately 13% of the total) and non-reconstructed buildings (87%). Concerning the PS located on reconstructed buildings, the time series underwent a preliminary cleaning process. This involved removing the deformation interval prior to the reconstruction phase, also including minor intervention (e.g., adding new coats or materials as part of routine maintenance) capable of producing macroscopic variations (e.g., a few cm) between one measurement and the next, ensuring that only relevant data

points were considered as PS. For this purpose, we accessed a database that provides extensive information about the buildings located in the L'Aquila downtown. Preliminary statistical analyses involving reconstructed and non-reconstructed buildings revealed an average displacement velocity (in mm/year) of -0.85 for the reconstructed category and -0.99 for the non-reconstructed buildings. The average cumulative displacement amounts to -9.95 mm and -11.59 mm, respectively.

In Figure 15, the COSMO-SkyMed A-DInSAR deformation map is displayed with a mask that delineates the buildings in the historic center. The mask distinguishes between buildings that have undergone restoration (in blue) and those that have been reconstructed (in pink) following the earthquake.
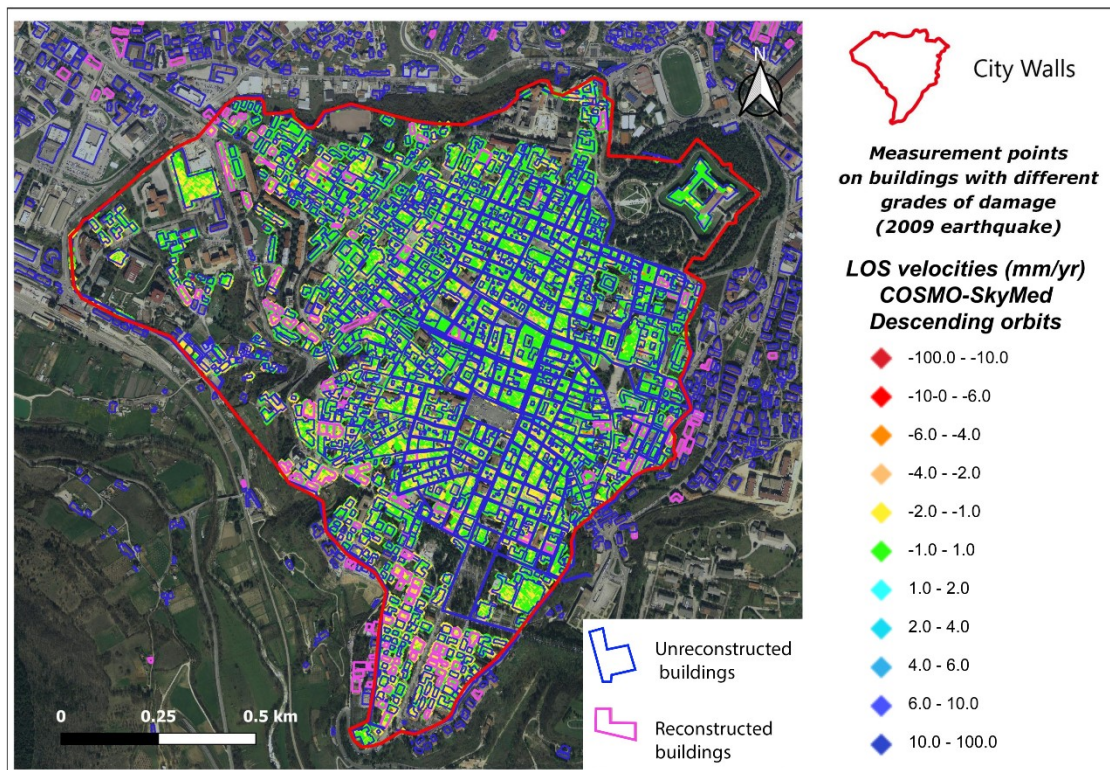

Figure 15: COSMO-SkyMed A-DInSAR deformation map is displayed with a mask that delineates the buildings in the historic center. The mask distinguishes between buildings that, following the 2009 earthquake, have undergone restoration (in blue) and those that have been reconstructed (in pink). The color scale used in the map for PSs

representation refers to the legend in the figure, noting that negative velocity values correspond to displacements along the satellite's Line of Sight (LOS). Conversely, positive velocities indicate points moving towards the sensor.

Since the reconstructed buildings exhibit higher LOS deformations than the non-reconstructed ones, a Cluster Analysis has been carried out, in order to identify potential differences in temporal trends between the time series of reconstructed and non-reconstructed buildings.

For data arrays indicated in Section 2.3.1. a coherence filter of 0.6 was preliminarily applied. Each data array is associated with a coherence value in the range (0-1), which can be viewed as a measure of data quality. It is observed that below the value of 0.6 the scattering increases significantly and two value clusters are detected with subsidence or uplift rates of more than 15 mm/year (Fig. 16). The two clusters corresponding to extreme positive and negative values are associated with anomalous deformations compared to the average values recorded in the area, most likely due to phenomena in which we are not interested. Therefore, we considered such values, associated with coherence < 0.6, as outliers. On the other hand, data filtering according to too high coherence values results in data selection which may lead to small samples. The value of 0.6 was chosen because it offered the best compromise between data homogeneity and sample size.
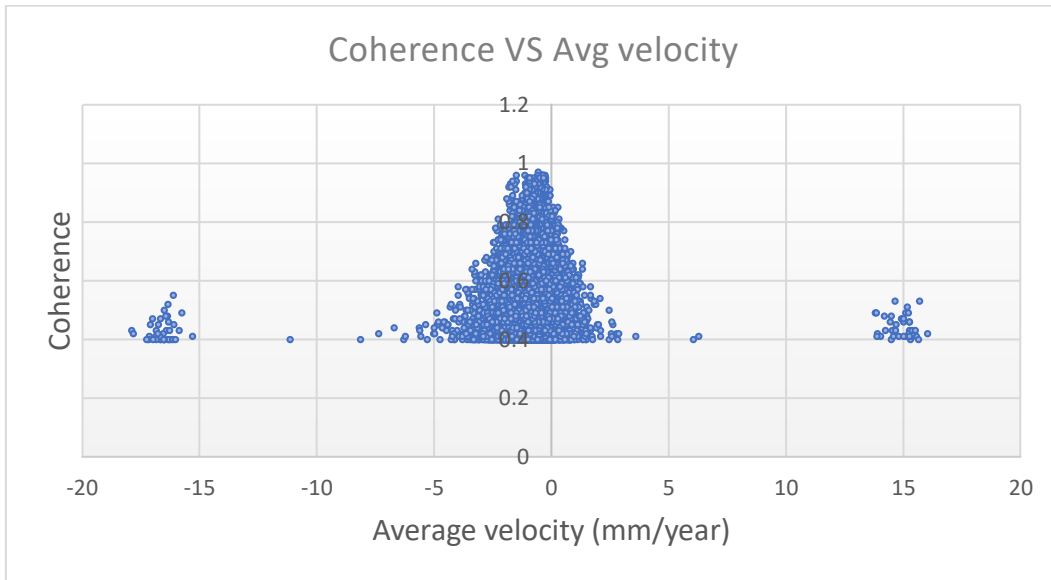
Figure 16. Coherence vs average velocity (mm/year) for non-rebuilt damage class 3 buildings. Considering consistency as a measure of data quality, it is observed that below the value of 0.6 the scattering increases significantly and two groupings of suspected outliers are detected with rates of over 15 mm/year.

Figure 17 illustrates the results of the analysis carried out according to the two different approaches described in Sect. 2.3, in which two clusters of curves were identified in the dataset relating to buildings with damage class 3 and reconstructed, one of subsidence curves and one of uplift. The two methods gave substantially similar results.
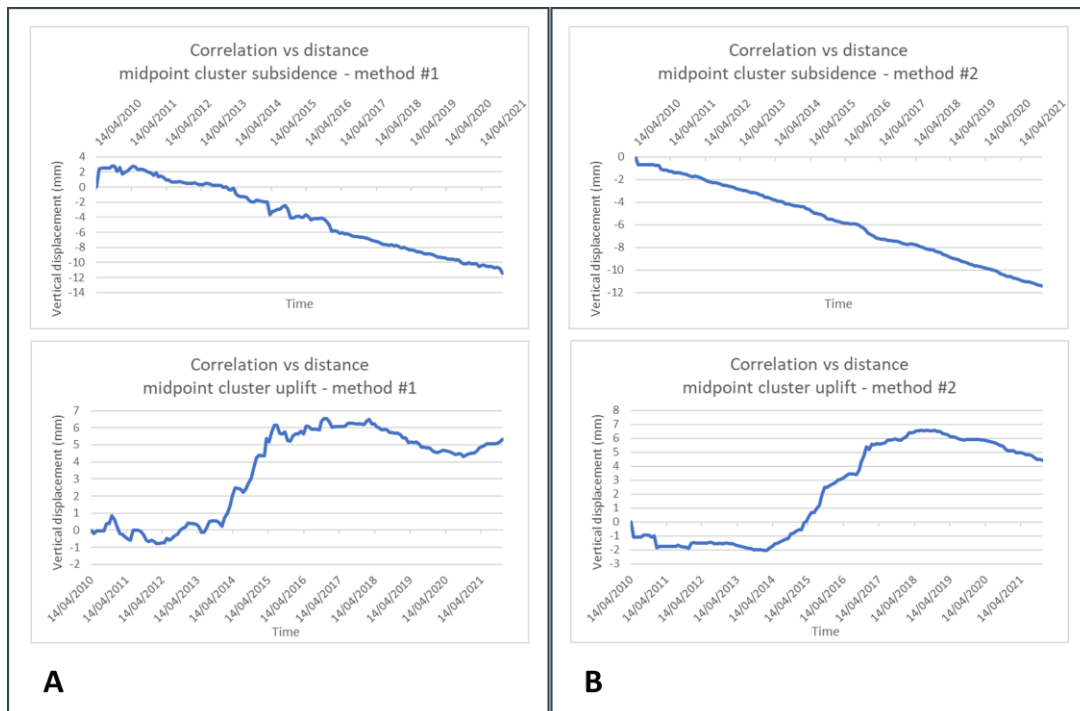
Figure 17: Midpoint of the two subsidence and uplift clusters identified according to the two approaches illustrated in Sect. 2.3. A) Results following the first described variant of the k-means algorithm. B) Results according to the second illustrated variant.

The midpoint vectors achieved by means of method I (Sect. 2.3.) allowed us to examine the correlation between the displacement-time curves and the geographical distance between monitored points (PS of COSMO-SkyMed descending map). Figure 18 depicts the correlation between the subsidence values recorded at the subsidence cluster midpoint and those of all other monitored sites, including those outside the cluster. This analysis specifically focuses on the dataset related to non-reconstructed buildings with DG3. Notably, the correlation values remain close to unity, indicating similar temporal trends among the curves, even for sites located at significant distances from each other. On the other hand, anti-correlation can be observed also among neighbouring (or not far) sites.
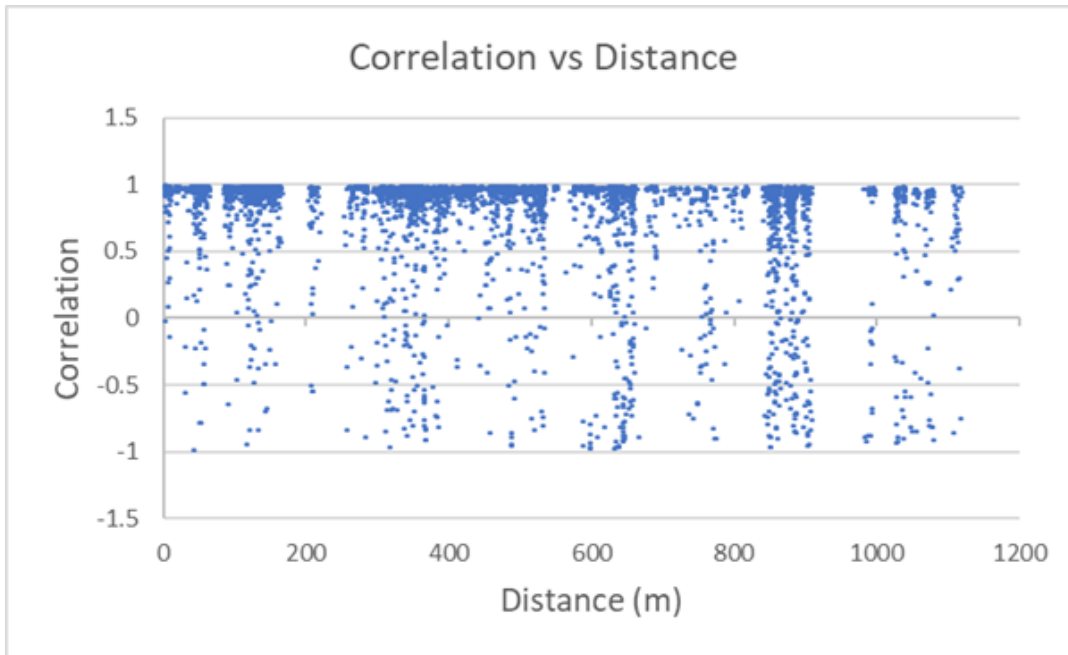
Figure 18: Correlation between displacement-time curves in the dataset related to non-reconstructed buildings with damage class D3. In the diagram, each point represents the correlation between the subsidence values recorded, on the same date, at the most representative PS within the subsidence cluster and all other PSs, including those outside the cluster. The horizontal axis denotes the reciprocal distance between these points, while the vertical axis represents the correlation value.

Figures 19 and 20 depict the midpoint curves of uplift and subsidence, achieved by means of the above illustrated method II (i.e., obtained as arithmetic average of the components of each vector belonging to the cluster, for each date). Figure 19 illustrates results related to non-reconstructed buildings, while Figure 20 to reconstructed ones.

Figure 19: Diagrams showing average vertical displacement (mm) vs time, for each cluster, for all DG (damage grade) of non-rebuilt buildings. Each curve represents the midpoint of its own cluster. Red circles outline an observed anomaly in subsidence trends. The two vertical dashed lines highlight the time range August-November 2016, in which the Amatrice-Norcia seismic sequence occurred. As the uplift curves are rather irregular (being achieved from small samples), such anomaly is not well recognisable. It should be remembered that the data relating to each curve have been preliminarily normalized with respect to the average velocity. Therefore, these curves only provide

information about the shape of the subsidence trend and not about the cumulative displacement.
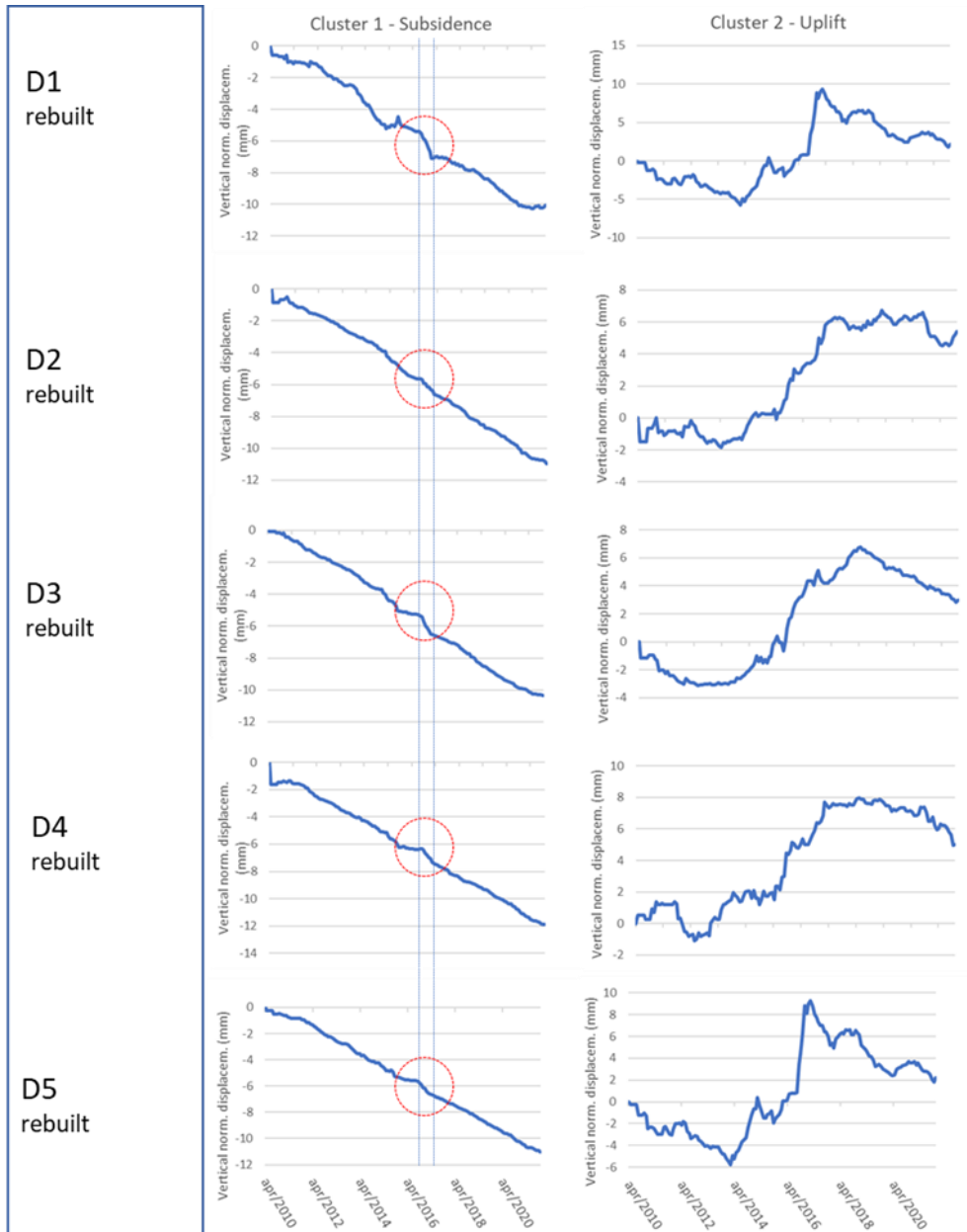
Figure 20: Diagrams showing average vertical displacement (mm) vs time, for each cluster, for all DG (damage grade) of non-rebuilt buildings. Each curve represents the midpoint of its own cluster. Red circles outline an observed anomaly in subsidence trends. The two vertical dashed lines highlight the time range August-November 2016,
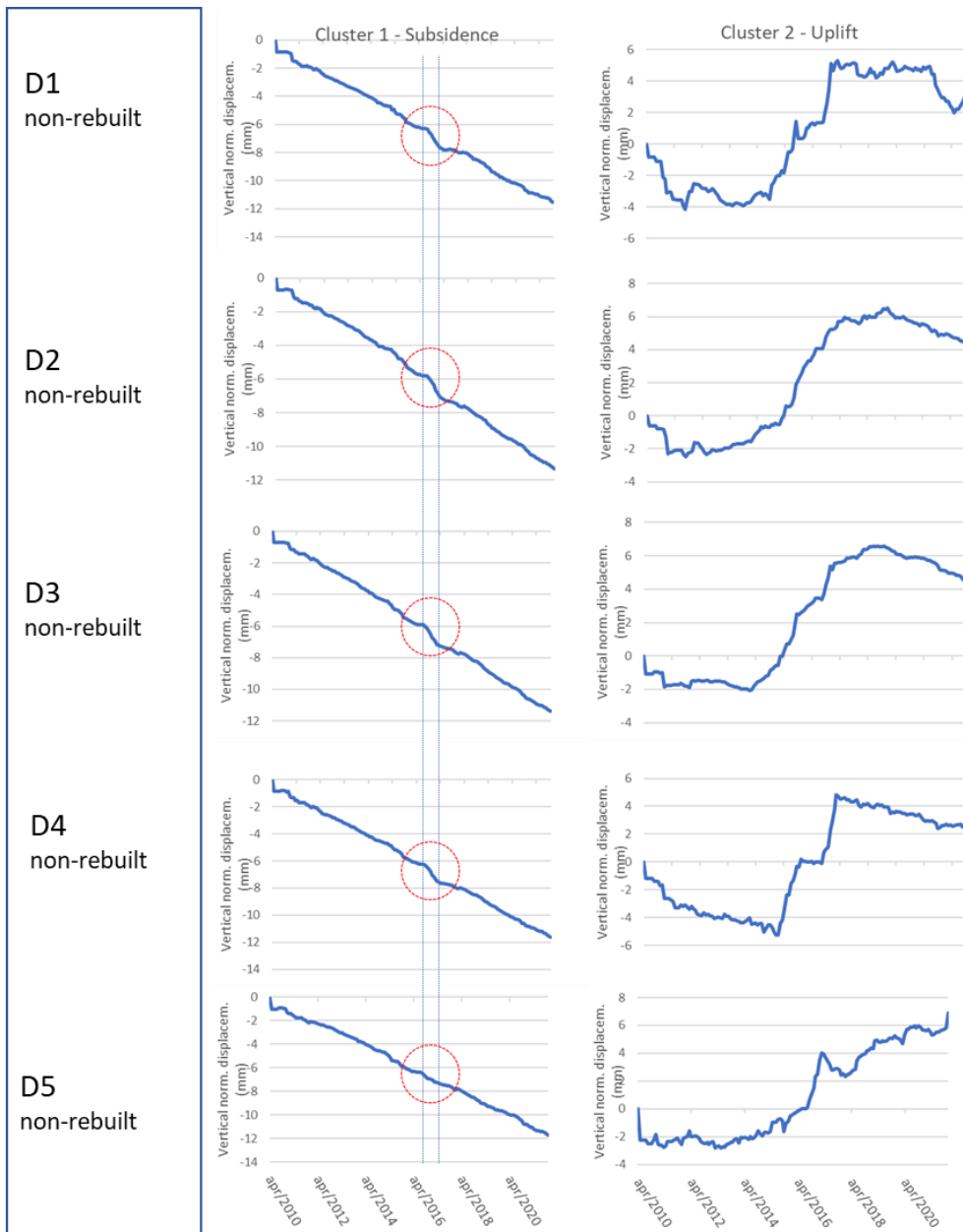
in which the Amatrice-Norcia seismic sequence occurred. As the uplift curves are rather irregular (being achieved from small samples), such anomaly is not well recognisable. Analogously to the case of non-rebuilt buildings, these curves only provide information about the shape of the subsidence trend and not about the cumulative displacement.

From this analysis, the following observations can be made:

i. For all 10 categories, the shape of the displacement-time curves, associated with midpoint of clusters, are analogue regardless of the damage class and the kind of maintenance undergone by the buildings (renovation/reconstruction). Therefore, subsidence/uplift phenomena show different intensities but a common trend, for different building categories and damage classes.

ii. Uplift curves exhibit an initial phase of modest displacements with possible sign changes, followed by a second phase of significant displacements, and a third phase of modest displacements with slight subsidence.

iii. Subsidence curves, on the other hand, show a relatively consistent and constant trend (in statistical terms).

iv. There is an anomaly in the subsidence curves close the time range associated with the Amatrice-Norcia seismic sequence (the anomaly is highlighted by a red circle, the time range August-November 2016, by means of two vertical dashed lines, in Figures 19 and 20). Therefore, it is plausible that such an event may have conditioned the subsidence trends or may be somehow related to these anomalies (i.e., both could have a common cause). This is a very interesting issue and will be of course subject of future research.

3.1.3. Subsidence velocity vs. damage intensity

The statistical analysis carried out highlights a significant variation (in inferential sense) of the average subsidence velocity values with the various damage classes, as well as for reconstructed buildings and not. As regards the average uplift values, in many cases the statistical sample is small and, therefore, it is not possible to identify significant variations due to a considerable sample uncertainty on parameter estimates. Figure 21A shows the average subsidence rate values (mm/year), with the respective 95% confidence intervals (which are not clearly visible because they are very narrow), for the non-reconstructed buildings, and for time series belonging to cluster 1. With the exception for data relating to damage classes D4 and D5, whose intervals show overlapping (i.e., the difference between average values is not significant), the confidence intervals appear well distinct and highlight an increase in average subsidence velocity as the damage intensity increases. For the reconstructed buildings (time series belonging to cluster 1), as there are fewer samples, the 95% confidence intervals overlap (Fig. 21B). Figure 21C compares the mean rates of subsidence for reconstructed and unreconstructed buildings. Between these two categories, the confidence intervals are well separated, pointing out an average difference of about 0.2-0.4 mm/year. A more accurate average value of such difference has been calculated as follows. The difference between cumulate displacement, over the studied time range, of rebuilt and non-rebuilt buildings for each damage class, has been weighted by using as weight function the inverse of standard deviation of the most uncertain value, (i.e., associated with the non-rebuilt category). Then, a weighted average of these five values have been calculated, which yielded a value of about 2 mm over 11 years. This is of course comparable (using, e.g., current legislation design values for buildings) to the deferred building deformation , given by the superposition of contraction of the vertical structures and bending of the floor on which the PS rest, as well as of the foundation soil in reloading conditions. Therefore, the difference in rate of subsidence between rebuilt and non-rebuilt buildings is to be considered as not relevant.
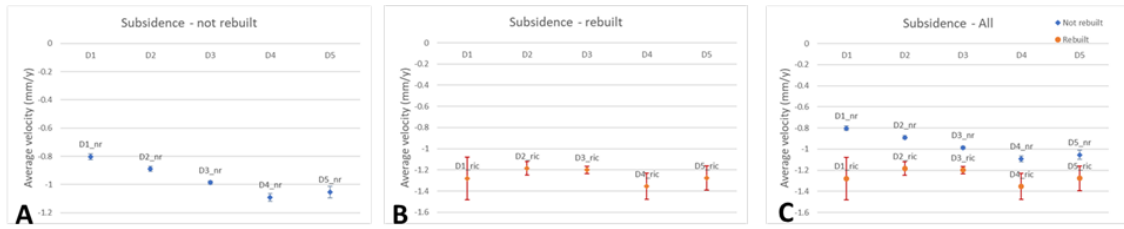
Figure 21: A) Average values, with related 95% confidence intervals, of vertical subsidence velocity (mm/year) for all categories of not rebuilt buildings; B) Average values, with related 95% confidence intervals, of vertical subsidence velocity (mm/year) for all categories of rebuilt buildings. C) Comparison of rebuilt and not-rebuilt building data. It should be noted as the confidence intervals for non-rebuilt building are very narrow. This also outlines as opportune sampling and an effective statistical analysis considerably reduce uncertainties in subsidence A-DInSAR data.

3.1.4. Measurement errors and reliability of the inferential statistical analysis

The partition of data into damage categories and clusters, as well as data cleaning and processing (Sect. 2.3.1.), have allowed to carry out a parametric statistical analysis on well-selected and homogeneous datasets. This brings to light a systematic average subsidence velocity increase as damage severity increases, for non-reconstructed buildings. Here, we emphasize that the statistical significance of the observed dependence of subsidence rate on building damage severity is guaranteed by the fact that the 95% confidence intervals of the observed statistics are well-separated. It is worth recalling that the mean of a sample of random variables (in this case, subsidence rates) is itself a random variable, characterized by its own statistical variability described by the standard deviation. This latter, due to the well-known central limit theorem, is a function of the standard deviation of (individual) velocity values belonging to each analysed cluster. Therefore, the effect of each cause which confers variability to each velocity measurement, such as, e.g., spatial variability, measure inaccuracy, is accounted for by the estimate confidence interval. Since a 95% confidence interval guarantees that the true value of the estimated statistic - here, the average subsidence rate associated with each cluster in each building category - is very

unlikely to be outside that range, we can state that the estimates reported in Fig. 21A are actually different, except for those associated with the DG4 and DG5 classes, whose intervals overlap.

3.2. February 02, 1703 earthquake

By utilizing the post-earthquake damage map from 1703 produced by (Colapietra, 1978) and geo-referenced for this scope, we were able to carry out a comparative analysis with interferometric data achieved from COSMO-SkyMed (covering the time interval of 2010-2022). The descending COSMO-SkyMed deformation map was specifically cropped using polygons representing three distinct building types: destroyed buildings, damaged buildings, and undamaged buildings (Colapietra, 1978) (Figure 22). For each of these categories, we calculated the average deformation velocity (in mm/year) and the respective 90% confidence intervals. The obtained values are reported in the following Table 5.

The statistical distribution of cumulative displacement values for each damage class is shown in the histograms in Figure 23 Total collapse ("destroyed buildings" class) was observed in 48.26 % of the buildings, damaged buildings represent the 45.65% and only the 6.08% of total structures suffered no damage.

Table 5. The table shows the average velocity and related 90% confidence interval upper and lower limits, computed from the descending COSMO-SkyMed map for buildings which were destroyed, damaged and undamaged following 1703 earthquake.

Building Type	Average deformation velocity (mm/year)	Confidence interval 90% lower limit	Confidence interval 90% upper limit
Destroyed buildings	- 0,86	- 0,69	- 0,79
Damaged buildings	- 0,81	- 0,79	- 0,83
Undamaged buildings	- 0,74	- 0,84	- 0,88
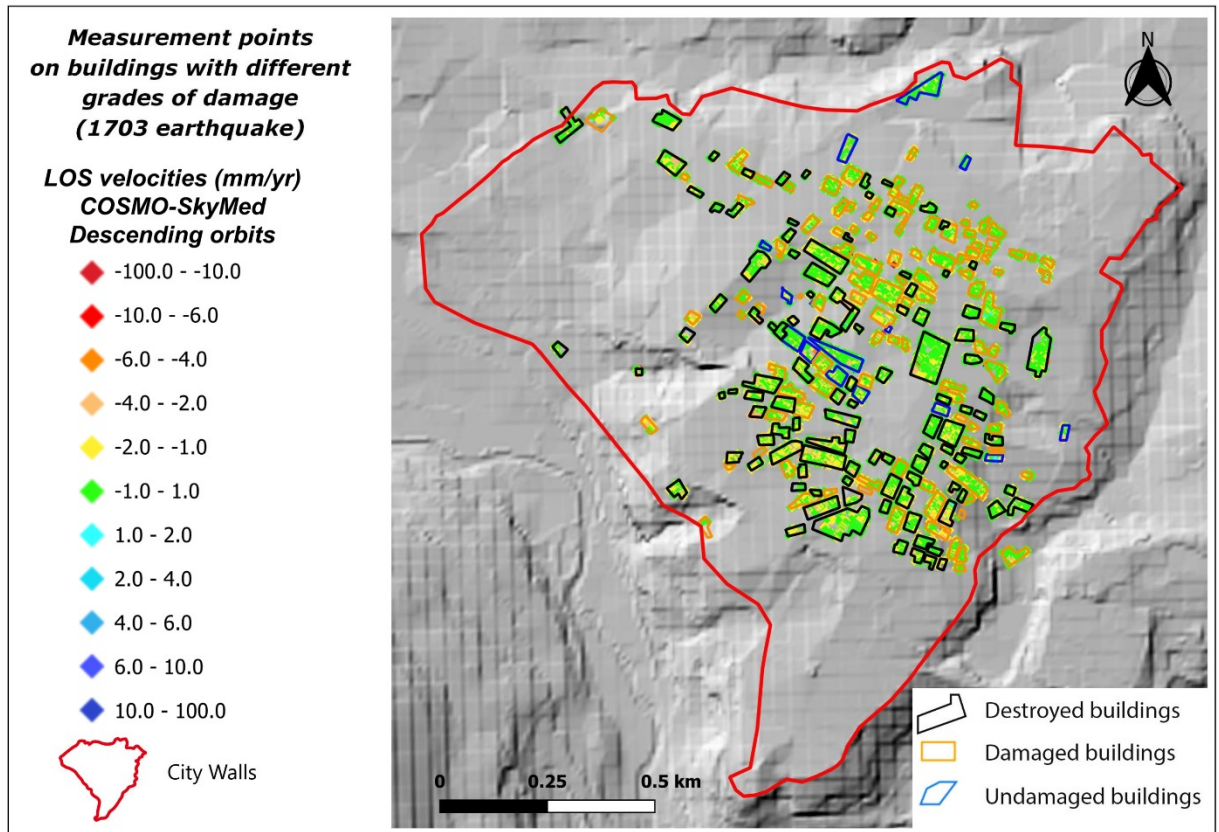
Figure 22: Descending COSMO-SkyMed deformation map, cropped using polygons representing three distinct building types: destroyed, damaged, and undamaged. The color scale used in the map for PSs representation refers to the legend, noting that negative velocity values correspond to displacements along the satellite's Line of Sight (LOS). Conversely, positive velocities indicate points moving towards the sensor.
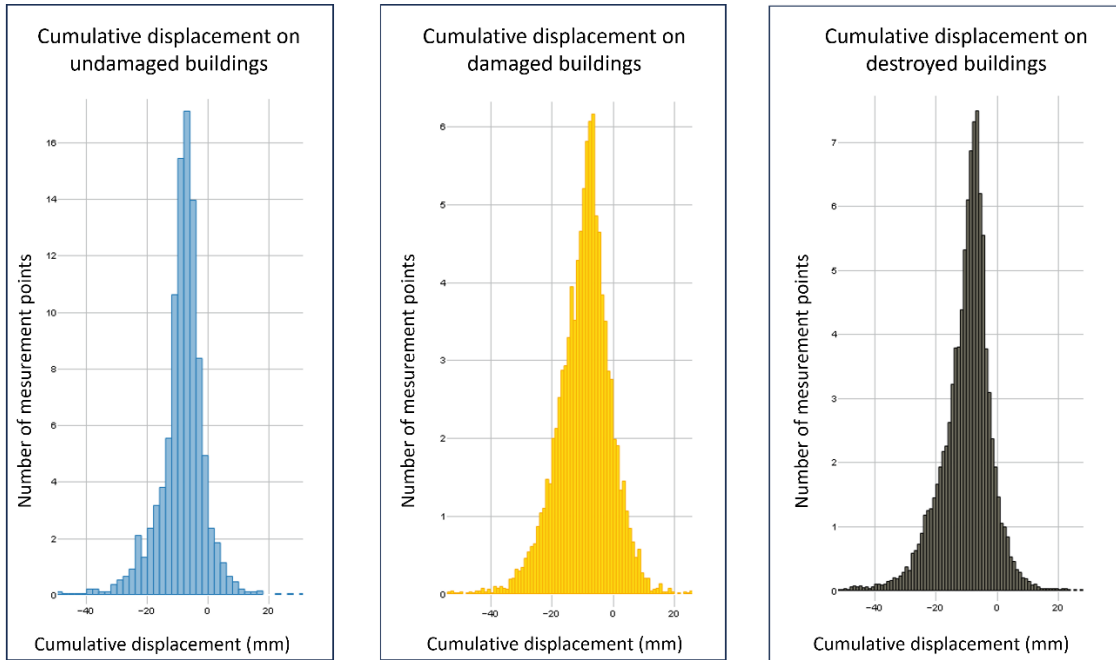
Figure 23: Statistical distribution of cumulative displacement values for each 1703 seismic damage grade. The distribution of damage is depicted by the placement of Persistent Scatterers (PS) in figure 22, which are cropped by means of polygons whose colors are associated with the three damage classes. For each 1703 seismic damage category the diagram illustrating Number of PS vs. Cumulative Displacement, is reported.

Even for the case of the 1703 seismic event, the average velocity values associated with the different damage classes have non-overlapping confidence intervals. This corroborates the hypothesis that the average subsidence velocity increases systematically as the intensity of damage to buildings increases. It should be noted that, since the damage data set for the 1703 seismic event is less extensive than that for 2009,

the analysis was conducted according to a more simplified procedure than those illustrated in sections 3.1.2. to 3.1.4. In particular, the data were not selected on the basis of coherence or through cluster analysis, to avoid working with too few statistical samples. Furthermore, the 90% rather than 95% confidence interval was considered, as it was taken into account that the statistical sample was of lower quality. Therefore, the analysis relating to the 1703 seismic event presents results affected by greater uncertainty compared to that conducted on 2009 data and could benefit from future studies carried out according to more effective statistical methodologies. Although the conclusions reached regarding the correlation between subsidence velocity and degree of damage, relating to the 1703 seismic event, are weaker than in the case of the 2009 event, they strengthen this working hypothesis.

4. Discussions

The use of satellite SAR interferometry for the study of deformations that characterized L'Aquila downtown in the decade following the 2009 earthquake (the most recent seismic event that severely damaged the city) has revealed the presence of subsidence rates with velocities reaching and rarely exceeding -5 mm/year. Considering the remarkable precision of the employed A-DInSAR map (which benefits from an extensive PSs coverage and is generated using a 10-year-long time series of regularly obtained images), the deformation analysis has transcended the conventional instrumental threshold (set at ±1.5 mm/year). Following the footsteps of previous works by [44] and [45], and despite the low deformation rates, this approach has allowed for the identification of a progressive increase in cumulative displacement of about -1 mm for each damage grade class. The building damages caused by the 2009 and 1703 earthquakes match with the deformations recorded by the satellite between 2010 and 2021. Satellite data consistently show that the most heavily damaged structures (D3, D4, D5 – for the 2009 earthquake - Destroyed and Damaged buildins– for the 1703 earthquake) exhibit the highest levels of deformation. In particular, a systematic increase in subsidence rate has been observed as the damage level increases. Consistent with the previously mentioned cumulative displacement data, a difference in velocity of

approximately 0.1 mm/year has been observed for each damage grade class from DG 1 to DG 4. The average velocity values (and consequently, cumulative displacement) associated with damage classes DG 4 and DG 5 show overlapping confidence intervals, indicating that the observed difference is not statistically significant. In a similar vein, even though the urban sprawl in 1703 was considerably more limited than today, with areas like the southern sector of the city undergoing urbanization only in the past 80 years (A. Tertulliani et al., 2012), the findings revealed that the zones surrounding buildings destroyed by the 1703 earthquake exhibited higher levels of deformation captured by COSMO-SkyMed over the preceding decade. This stands in contrast to regions where structures had experienced only minor damage. Furthermore, there was a distinct reduction in deformation observed in areas that had remained undamaged during the 1703 event. Since the intensity of damage can be interpreted as an indicator of the intensity of local seismic strain intensity, the increase in subsidence rate can be attributed to a rise in seismic shacking. Considering that the zones exhibiting higher subsidence rates also suffered more extensive damage from both the 2009 and 1703 earthquakes and taking into account the substantial differences in urban layout between these two events, it's plausible to hypothesize that there exist geological and/or tectonic conditions influencing the structural damage across various areas of the city. Indeed, the significant impact of surface geology on the dispersion of damage, not only for the 2009 earthquake but also for the 1703 earthquake, have already recognized (Tallini et al., 2020). The damage increased with thickness of soils exhibiting higher compressibility was observed (Tallini et al., 2020). If, on one hand, the study carried out by (Tallini et al., 2020) focused on the effects of varying thickness of such lithologies on different types of buildings (e.g., reinforced concrete and masonry), the recognition of the absence of a difference in velocity between GP and BP (by mean A-DInSAR COSMO-SkyMed analysis) suggest that the deformations may not be directly influenced by buildings' specific characteristics (Fig. 11). This observation it's also validate by the comparison of vulnerability map of the buildings with the distribution of deformations recorded by the satellite (Fig. 13). With exception of churches and monuments, it doesn't appear to be a direct correlation between vulnerability and satellite-recorded deformations for the rest of the buildings. Namely, cumulate displacement does not

exhibit systematic variation as vulnerability increases. The different values detected at churches and monuments, are likely attributed to their reconstruction using rubble after the 1703 earthquake [41], and furthermore, as these are heavy buildings, in many cases associated with structures showing very high concentrated loads, such as towers and bell towers. The cluster analysis, which identified recurring trends in the time series of both reconstructed and non-reconstructed buildings, further supports the hypothesis that geological conditions influence deformation. Despite recording varying velocity and cumulative displacement values for different damage and intervention categories, in terms of the shape of subsidence curves, these exhibit similar patterns across the five damage classes, irrespective of whether buildings underwent renovation or reconstruction. Conversely, if the deformation phenomenon were determined by the building type, the shape of the displacement time series curves would differ from one building to another. The differences in cumulative displacements associated with reconstructed and non-reconstructed buildings align with the typical delayed settlements of reinforced concrete structures.

The observed geostatistical data reveals a widespread subsidence motion throughout the investigated area (see subsidence curves of cluster midpoints in Figures 19 and 20), with deformations exhibiting similar trends even for distant sites, while also displaying scattered values for neighbouring points (as highlighted in Figures 14 and 18). The spatial variability of subsidence/uplift rates appears as a local phenomenon superimposed on a prevailing subsidence process, common for the whole area. Furthermore, the cluster analysis revealed the existence of a distinct cluster of Persistent Scatterers exhibiting uplift. These curves exhibit shared patterns but with varying degrees of internal variability. The recorded displacements in the uplift related cluster are relatively small. It's worth noting that this cluster represents a mere 2% of the total dataset. The observed geostatistical data show a subsidence motion extended to the entire investigated area, with local variability and possible change of sign (uplift). Generalized subsidence can be associated with deformation of lithological layers present below the whole area. However, it cannot be excluded that the subsidence is extended to a regional scale and possibly associated with deformation of deeper layers. Local variations in subsidence rates are likely associated with local variations of

lithology in the more superficial layers. The underlying cause for these deformations cannot be definitively determined, except to attribute them to the data processing involved in generating the A-DInSAR map. This process involves selecting a stable reference point to serve as the baseline for all other PS.

A further result of our analysis concerns the observation of an anomaly in subsidence rates during the period through the second half of 2016 and first half of 2017 (highlighted by the midpoint curves of the clusters in Figures 19 and 20). One possible cause that may have contributed to this anomaly is the seismic sequence of Amatrice-Norcia, which occurred in central Italy between August 2016 and January 2017. Although explaining these anomalies lies well beyond the scope of this work, this is a very interesting finding and will be object of future research. It should also be noted that the interferometric map used displays deformation values recorded along the satellite's Line Of Sight (LOS) in descending orbit. For a better understanding of the observed flex in the various curves, it would be beneficial to evaluate the deformations recorded in ascending orbit and perform a decomposition of the deformations into their vertical and horizontal components. However, the coverage of COSMO-SkyMed images for the study area during the relevant period is limited, making such analysis unfeasible.

5. Concluding remarks and perspectives

The main conclusions arising from the interferometric analysis carried out in the decade following the seismic event that struck L'Aquila in 2009 are summarized below:

i. Post- seismic deformation pattern, acquired by means of A-DInSAR instrumental measurement, matches with both the damage map for 2009 and 1703. A systematic and statistically significative increase of subsidence rate (as well as cumulate displacement) has been observed as building damage level increases.

ii. Therefore, since deformation identified by COSMO-SkyMed between 2010 and 2021 appears as not solely matching with 2009 seismic event effects but,

rather, as characterizing risk features of the studied area in general, our findings pave the way for a new utilization of long-term time series of satellite SAR data in high-risk seismic areas, as a powerful tool aimed at mapping most vulnerable regions and effectively mitigating seismic risks. This would be a relevant goal, as this methodology allows large areas to be monitored at low cost. In this regard, in view of future research, this method may benefit from validation based on pre-seismic data (when they will be available).

The lack of differences in velocities between ground-level (GP) and building-based PS (BP) indicates that subsidence rates are not affected by building features and/or its presence. Furthermore, displacement spatial analysis outlines a locally variable displacement field (also exhibiting local uplift), overlying to a generalized subsidence, involving the whole studied area. These evidences corroborate the hypothesis that vertical ground displacement are mainly controlled by underground geological structure. A detailed study of such dependence lies beyond the scope of this work. Future studies will delve into a more comprehensive analysis of geological and geomorphological factors that impact deformation distributions within L'Aquila downtown, in order to reach a deeper understanding of the complex interplay between seismic events, geological features, and deformations in this area.

Further interesting evidence, issued by our analysis, regards an anomaly in subsidence rate, for all here considered building categories, along the time range associated with the Amatrice-Norcia 2016 seismic sequence, which will be subject of future research.

Appendix 1. Recalls about the k-means method

The k-means algorithm is a Machine Learning criterion able to identify clusters of elements in a given metric space, which is not to be confused with the Euclidean space, but which denotes a Cartesian system made up of variables of any nature. Our data consist of vectors with 158 components (i.e., 158 vertical displacement measurements recorded, for each PS, over about 12 years), each associated with a point in the

monitored area. In these hypotheses two curves yj(t) are considered coincident if the arrays yj(t) have all the components equal, "close" if the differences between the components are moderate and "distant" if these differences are significant. The algorithm progresses according to the following steps:

1) The number of clusters to be identified is initially fixed (this is a known parameter of the problem).

2) Plausible initial values are assigned for the coordinates of the cluster midpoints.

3) By using an appropriate criterion, the elements (in our case, the vectors $yj(t)$) belonging to each cluster are identified. In this case, an element is considered to belong to a cluster if its distance (defined as described above) is less than a desired threshold value. Otherwise, the element is considered outside the cluster.

4) The midpoint for each cluster is recalculated, and the process described in step #3 is repeated.

5) The process is repeated until, for each cluster, the distance between the midpoint calculated in the previous step and the current one is below a desired threshold value (or if they coincide).

This algorithm usually converges rather quickly. The choice of the criterion to measure the distance between two data arrays plays a key role in the analysis design. In this work, two alternative definitions of distance are used, and the related algorithms are conventionally denoted as method I and method II. In method I the distance between two vectors y_j and y_k is defined as ($D = 1 - $ Correlation(yj(t), yk(t))). An array is considered to belong to a cluster if D is less than a predetermined threshold value (e.g., $D < 0.2$) and the cluster midpoint is given by the vector for which the sum of the distances from all its other arrays is minimum. In method II the components of each vector yj (t) have been preliminarily re-scaled by dividing by the mean subsidence/uplift rate (mm/year) corresponding to each vector. This allowed us to compare time series showing similar trend shape, independently from their subsidence size. In such method, the distance between two vectors y_j and y_k is calculated as a Euclidean distance, in the

158-dimensional space $\left(D_{jk} = \sqrt{\Sigma_n(y_j(n) - y_k(n))^2}\right)$, and the midpoint of the cluster is the barycentre in that space, i.e., the array y(t)* whose components are equal to the arithmetic average of those of the arrays of the cluster itself. Furthermore, an element is considered to belong to the cluster if the distance from the midpoint is less than a desired threshold value and not to belong to it, otherwise.

Chapter III - Geological and Hydrogeological Drivers of Seismic Deformation in L'Aquila, Italy: Insights from InSAR Analysis

1. Background and state of the art

The study of pre- and post-seismic ground behavior is of increasing importance in the context of seismic risk mitigation and predicting the local seismic effects induced by earthquake is of course crucial for urban planning. For this reason, the use of Advanced Synthetic Aperture Radar Interferometry (A-DInSAR) (Berardino et al., 2002; Alessandro Ferretti et al., 2001) has become increasingly common, especially in urban contexts (Lanari et al., 2010; Martino et al., 2022). This technology offers advantages such as relatively low costs, the ability to cover extensive areas, millimetric accuracy, and the capability to investigate long temporal periods (Cigna et al., 2011; Ezquerro et al., 2020; Nappo et al., 2020; Tomás et al., 2014).

Therefore, in this presented case-study, the comparison of A-DInSAR data of L'Aquila historic center, hit by the April 6, 2009 (Mw: 6.29) near source earthquake, and its geological and hydrogeological very fine-scale setting were carried out with the goal to analyze in-depth the effectiveness of this Radar Remote Sensing technique to the mitigation of seismic risk of Italian historic urban area, such as L'Aquila downtown, characterized generally by low seismic building vulnerability and high Cultural Heritage value.

The historic center of L'Aquila (i.e. medieval urban area located inside the walls, in the following LAHC), focus of this study, is situated on a flat terraced hill, and the ground has elevations ranging between 630 and 730 meters. It is crossed by the Aterno River, which flows from northwest to southeast, and the Raio Stream, a right bank tributary of the Aterno River, which flows eastward (Antonielli et al., 2020b; Tallini et al., 2020). The city is built mainly on limestone breccias known as the "L'Aquila Breccia" (LAB), covered by a variable thickness (ranging from a few meters to 20-30 meters) of fine-grained colluvium (Red Soils - RS) (Antonielli et al., 2020b; Magaldi & Tallini, 2000; Nocentini et al., 2017a). RS formed through karst weathering of the upper Pleistocene limestone substrate (LAB) and cover, mantling discontinuously, the top of the highly

irregular LAB paleosurface (Tallini et al., 2020). In this study, with respect to L'Aquila earthquake, the post-seismic time series (2010-2021) was analyzed. Located in a high seismic risk area (Figure 1), during time, the city has been struck by numerous earthquakes that have caused severe damage or destruction. Among these, the most significant were those in November 27, 1461 (Mw: 6.5) and February 2, 1703 (Mw: 6.7) (Galadini et al., 2003; Andrea Tertulliani et al., 2009), whose effects can be compared to the more recent and destructive near source earthquake of April 6, 2009, with a magnitude of 6.29 (Anzidei et al., 2009; Atzori et al., 2009; Chiarabba et al., 2009; Tallini et al., 2019). Through an interferometric analysis conducted on L'Aquila downtown, (Sciortino et al., 2023) recognized an increase in deformations recorded by Cosmo-SkyMed in the decade following the April 6, 2009, event, proportional to the seismic damage. The correspondence between deformation intensity and damage, observed for both the recent 2009 earthquake and the historical 1703 earthquake, suggests the presence of geological factors that make some areas more susceptible than others. This study aims to clarify the geological and geomorphological conditions that determine the distribution of deformation in the study area. Indeed, a deep understanding of geology is essential for interpreting InSAR maps (Nappo et al., 2020; Tosi et al., 2009) and investigating deformations induced by geological processes (Cigna et al., 2011; Nappo et al., 2020). Furthermore, several previous studies (Amoroso et al., 2018; Del Monaco et al., 2013; Durante et al., 2017; Mannella et al., 2019; Martelli et al., 2012; Nocentini et al., 2017a; Tallini et al., 2020) have shed light on the influence of the variability (both spatially and in terms of thickness) of continental deposits, which represent the city's substrate, on seismic site amplification (Macerola et al., 2019). These insights, combined with a comprehensive database of geological and geophysical surveys conducted in the city of L'Aquila (many of which were carried out after 2009 to expand knowledge of seismic site amplifications in the urban area), enable us to assess the satellite deformations recorded by Cosmo-SkyMed between 2010 and 2021, while examining subsurface geology from a new perspective. In this study, we have (i) identified the most relevant geological - geomorphological factors for deformation analysis; (ii) reanalyzed existing surveys in the historic center of L'Aquila to produce a detailed geological map; (iii) used Pearson's correlation

coefficient (PCC) analysis to assess the influence of factors such as the thickness of the Red Soils (RS), depth of regional aquifer, terrain slope, and surface geology on InSAR deformations; (iv) evaluated the correlation between precipitation and seasonal ground deformation.
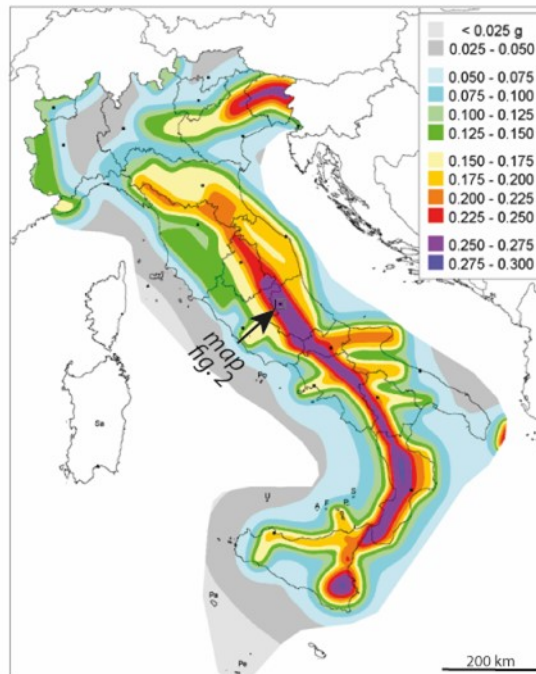
Figure 1: Map of the Seismic Hazard of Italy, showing peak ground accelerations (g) that have a 10% chance of being exceeded in 50 yr (Meletti and Montaldo, 2007). The arrow refers to L'Aquila area.

1.1 Geological setting

The study area is located in the western portion of Middle Aterno R. intermontane basin, which formed during the Plio-Quaternary extensional regime that affected the Central Apennines (Boncio et al., 2004; Cavinato et al., 2002; Cosentino et al., 2017). This region is characterized by a fold-and-thrust mountain chain responsible for crustal shortening. The post-orogenic extension led to the formation of a network of intermontane basins situated on the hanging wall of normal fault structures, oriented NW-SE and N-S (Cosentino et al., 2010). These basins are filled by mainly Quaternary

continental detrital deposits pertaining to slope, lacustrine and alluvial environments and reaching up to several hundreds of meters in thickness. Within this context lies the Middle Aterno R. basin, bordered by normal faults SW-dipping, which are responsible for historical and current seismic activity (Paolo Galli et al., 2010; Storti et al., 2013)). The Middle Aterno R. basin consists mainly of two partially interconnected secondary basins: the L'Aquila - Scoppito basin (ASB) and the Paganica-San Demetrio-Castelnuovo basin (PSC) (Cosentino et al., 2017; Giaccio et al., 2012; Nocentini et al., 2017a, 2018; Spadi et al., 2016), as shown in Figure 2, panel a. The ABS, where the study area is located, is a half-graben filled with approximately 600 meters of continental deposits (Giaccio et al., 2012; Mancini et al., 2012; Nocentini et al., 2017a; Tallini et al., 2019), characterized by complex stratigraphic relationships. It overlies the substrate formed by Meso-Cenozoic marine carbonate pre - orogenic formations and upper Miocene synorogenic terrigenous formation (Tallini et al., 2019).

During the Piacenzian to Gelasian age, the carbonate sedimentation in the ASB (L'Aquila-Scoppito basin) comprises the deposition of S. Demetrio-Colle Cantaro (CCF) system (Cosentino et al., 2017; Nocentini et al., 2017a, 2018; Spadi et al., 2016), heterometric breccias with a clayey-silty matrix. The CCF system and the underlying bedrock are unconformably overlain by the sands and clays of the Madonna della Strada formation (MDS). The MDS represents the development of a fluvial environment with alluvial plains and extensive marshy areas near meandering river channels during the Early Pleistocene (Agostini et al., 2012; Storti et al., 2013). The Fosso di Genzano unit, incised into the earlier deposits or meso-Cenozoic bedrock, is primarily associated with distal portions of alluvial fans, which laterally transition to braided alluvial plains during the Middle Pleistocene.

Above these geological layers, there are 20-100 meters of L'Aquila Breccia (LAB) (Tallini et al., 2020). LAB consists mainly of heterometric carbonate clasts with sizes ranging from centimeters to meters, poorly sorted, and set within a sandy-clayey calcareous matrix that can vary in color from white to yellowish. Covering the top of the LAB are the Red Soils (RS), which formed during a humid and warm interglacial phase of the Late Pleistocene (MIS 5e, Eemian). These red clays include paleosols and

epikarst deposits and exhibit highly variable thickness, reaching up to 30 meters (Magaldi & Tallini, 2000; Tallini et al., 2006). The LAHC buildings lay chiefly on LAB and Red Soils (RS).

Lastly, the uppermost deposits that have filled the ASB consist of fluvial deposits of the Fosso Vetoio system (FVS) (T1 – Early Upper Pleistocene), slope deposits of the Colle di Pile system (CPB) (Late Upper Pleistocene), Holocene colluvial deposits, and alluvial deposits of the Aterno River (ATF).

In Figure 2b a schematic geological section of ASB from (Nocentini et al., 2017a, 2018) is provided.

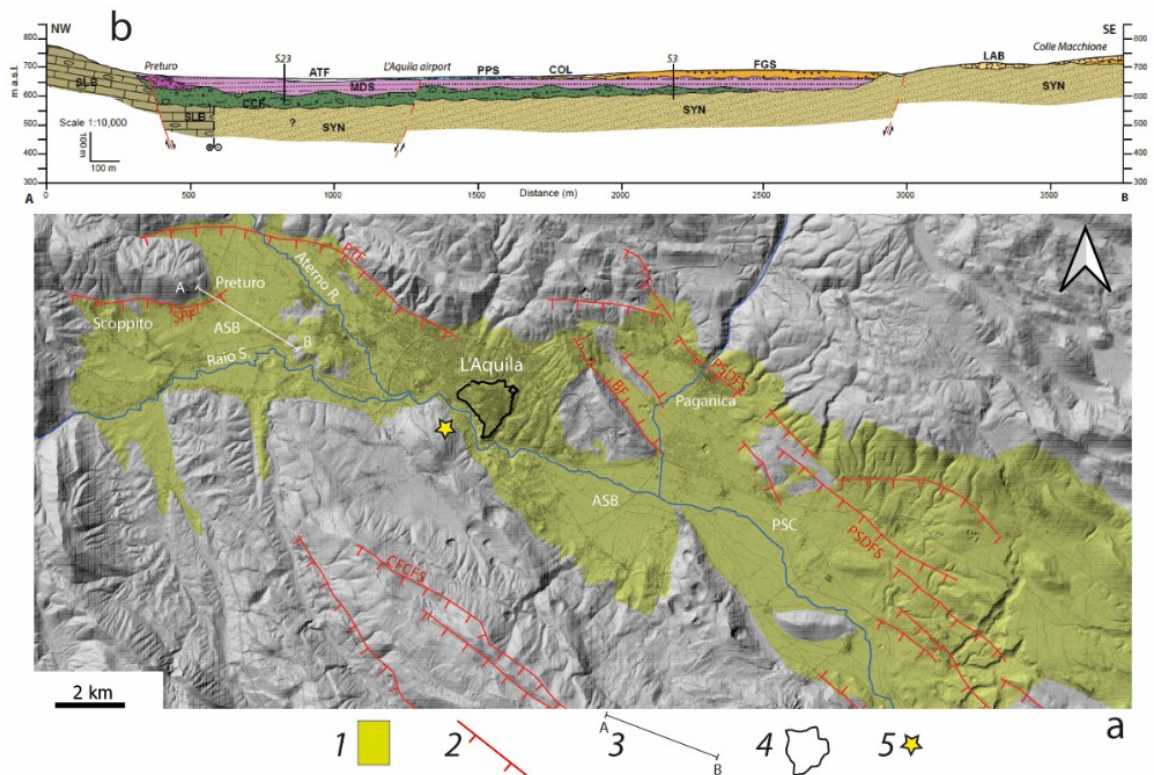Figure 2: In panel a L'Aquila area simplified geological map. 1) Quaternary detrital deposit of the Middle Aterno R. intermontane basin (ASB: L'Aquila-Scoppito Basin; PSC: Paganica-San Demetrio-Castelnuovo Basin sensu (Nocentini et al., 2017a, 2018)); 2) Main Quaternary active faults; SPF: Scoppito-Preturo fault; PTF: Mt. Pettino fault; CFCFS: Colle Cerasitto-Campo Felice-Ovindoli fault system; BF: Bazzano-Fossa fault;

71

PSDFS: Paganica-San Demetrio fault system; 3) geological section of panel b 4) the studied area: L'Aquila historic downtown located inside the medieval walls perimeter (LAHC); 5) April 6, 2009 Mw: 6.29 L'Aquila earthquake epicenter; b) geological section from (Nocentini et al., 2017a). ATF - Aterno Synthem (Holocene): mixed fine- and coarse-grained alluvial deposit; COL: colluvium; PPF - Ponte Peschio Synthem (Upper Pleistocene): coarse-grained alluvial deposit; LAB - Colle Macchione-L'Aquila Synthem (upper Middle Pleistocene): calcareous breccia; FGS- Fosso Genzano Synthem (Middle Pleistocene): coarse-grained alluvial deposit; MDS- Madonna della Strada Synthem (Calabrian): fine grained alluvial deposit; CCF- Colle Cantaro-Cave Formation (upper Piacentian-Gelasian): coarse-grained alluvial deposit; SYN: Neogene syn-orogenic formations sandstone and pelite; SLB: Meso-Cenozoic carbonate formations.

2. Materials and Methods

2.1. Multi-Satellite A-DInSAR Displacement Data

In this research, we harnessed the power of Advanced Differential Synthetic Aperture Radar Interferometry (A-DInSAR) technique (Hanssen, 2001) to investigate the historical ground displacement rates within the L'Aquila municipality. A-DInSAR relies on the time gap between two radar satellite observations of the same location. These Synthetic Aperture Radar (SAR) images are analyzed to detect variations in the radar signal phase reflected from the Earth's surface. These phase changes directly correlate with surface deformations, enabling the creation of precise high-resolution deformation maps. The A-DInSAR technique is increasingly being employed to study the temporal evolution of ground displacements using time series, particularly for objects with consistent reflectivity over time, referred to as Persistent Scatterers (PS) (Alessandro Ferretti et al., 2001).

The PS-InSAR technique extracts information from a collection of SAR satellite images, forming an interferometric stack that enables the derivation of displacement patterns. We utilized datasets from two active satellite SAR missions, namely Sentinel-1

(by ESA) and Cosmo-SkyMed (by ASI), both offering historical archive data for scientific research. These datasets differ in terms of resolution, both spatial and temporal, as well as in acquisition bandwidth (C- and X-bands respectively). Sentinel-1 (S1) boasts a pixel resolution of 5x20 m on the ground, whereas Cosmo-SkyMed (CSK) offers a resolution of 3x3 m (specifically for the Interferometric Wide images available in the archive). The revisit time of the S1 constellation is shorter than that of CSK. The former operates with a revisit time of approximately 6 days, while the latter has an average revisit time of 16 days. This distinction is due to CSK's dual-purpose mission for both civilian and military applications, and it may result in sporadic gaps in data availability.

For this study area, we had to use two different satellite constellation datasets because in the CSK archive, there was a significant lack of images that would have made the multi-temporal analysis less valid. The datasets were processed using the PS approach (Kampes, 2006) based on a total of 547 SAR images. The selected time frame spans from 2010 to 2022 for both ascending and descending orbital geometries:

Ascending orbital geometry: 386 images in Single Look Complex (SLC) format acquired by the Sentinel-1 (S1) satellites from 20 October 2014 to 03 August 2022.

Descending orbital geometry: 161 Single Look Complex (SLC) format images obtained by Cosmo-SkyMed satellites from April 14, 2010, to November 30, 2021.

For each geometry, we conducted two separate analyses. A master image was chosen as the reference for calculating phase differences in other images within the dataset. The displacement rate values (expressed in mm/year) estimated by the A-DInSAR analysis were relative to the selected reference point. Additionally, we calibrated and validated our analyses using displacement data obtained from GNSS stations. Notably, the higher ground resolution of Cosmo-SkyMed SAR images resulted in a denser coverage of PS compared to the Sentinel-1 products.

The PS-ToolBox Suite within QGIS, developed by NHAZCA S.r.l. (NHAZCA, n.d.) was employed for post-processing. Within this suite, we primarily utilized the time

series visualization tool to understand the temporal evolution of displacement and the following two main post-processing analysis: Spatialization and Data Fusion.

Spatialization is a tool that enables the spatial conversion of point data into continuous maps through interpolation. The interpolation methodology used is based on the Inverse Distance Weighting (IDW) algorithm, which directly generates spatially continuous velocity or deformation maps. The algorithm calculates velocity or deformation values at each point in space by considering a weighted average that accounts for both the distance of PS points from the point of interest and other relevant qualitative parameters. The formula used to estimate the value at a point P is expressed as:

$$Vp = \sum Vi * (\, Pi \; di \,) \,/ \sum (\, Pi \; di \,)$$

Where Vp is the value at point P, Vi is the value of measurement point i within the influence radius, Pi is the weight of each measurement point within the radius, and di represents the distance of measurement point i within the influence radius from the interpolation point.

Data Fusion is a tool that allows the merging of data from multiple satellites and their decomposition into vertical and horizontal directions using Line of Sight (LOS) data as a starting point. To enhance the reliability and spatial coverage of displacement information, we combined the data from Sentinel-1 and Cosmo-SkyMed. This approach leverages measurements from multiple sources with distinct orbital geometries and employs the strain tensor method (Guglielmino, F., Bignami, C., Bonforte, A., Briole, P., Obrizzo, F., Puglisi, G., ... & Wegmüller, n.d.) through the ESISTEM (Extended Simultaneous and Integrated Strain Tensor Estimation from Geodetic and Satellite Deformation Measurements) (Francesco, Guglielmino; Giuseppe, Nunnari; Giuseppe, Puglisi; Spata, n.d.) method to create synthetic datasets incorporating multi-band information. The estimated displacement (DLOSkXp) for each synthetic data point (Xp=(xp,yp)) along the Line of Sight (LOS) is formulated using a first-order Taylor polynomial:

$$D_{LOS}^k(XS_d) = D_{LOS}^k(X_p) + \nabla D_{LOS}^k(X_p)\Delta XS_d$$

Here, *Sd* represents the direction cosine of the LOS, while ΔXSd contains the relative distances between the components of *XSd* points and the synthetic point *Xp*. The data fusion formulation takes into account two parameters: the maximum distance used for selecting nearby PS measurements to estimate deformations and the locality factor that weights each measurement's contribution based on its distance from the point being estimated. The synthetic datasets for Up-Down and East-West components are then derived into a regular grid of squared cells from the vector decomposition of the displacement map along the multi-satellite LOS.

For the study of A-DInSAR maps, the starting point was the identification of all factors that can cause ground deformation. For this purpose, recent papers were taking in to account and a geomorphological and hydrogeological study was carried out through the analysis of a digital terrain model (DEM) and the piezometric level.

2.2. *Collection and processing of geological – geomorphological, hydrogeological and geophysical data*

For the geological and seismic characterization of the study area all relevant geological, hydrogeological and geophysical data was collected. A total of 142 Shear Wave Velocity (Vs) in-situ measurements, pertaining to the shallow lithologies within LAHC but acquired also from neighboring areas, were compiled from bibliographic sources (Amanti et al., 2020; Amoroso et al., 2018; Del Monaco et al., 2013; di Giulio et al., 2014; Lanzo et al., 2011; Macerola et al., 2019; Pagliaroli et al., 2020). To conduct a comprehensive site geology analysis, the log from an extensive dataset of 573 boreholes, many of which were drilled after the 2009 earthquake to facilitate the reconstruction of LAHC buildings, were integrated with geological data from the literature (such as [9,12]). In Figure 3, the location of the 573 boreholes and 54 water wells acquired from the ISPRA (Istituto Superiore per la Protezione e la Ricerca Ambientale) database and used in this study is shown.
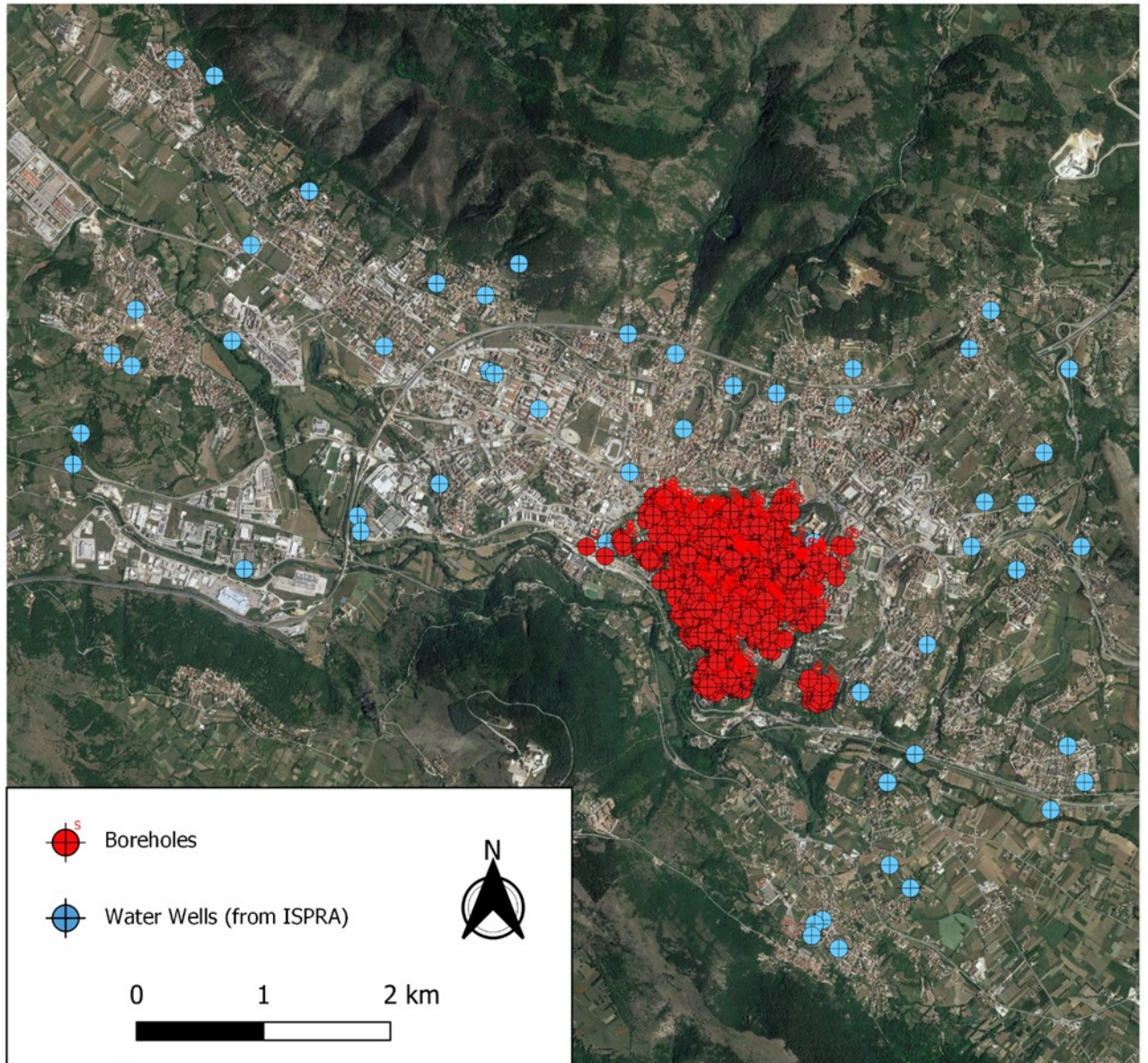
Figure 3: database of 573 boreholes (in red) from USRA (Ufficio Speciale per la Ricostruzione dell'Aquila) and 54 water wells from ISPRA (Istituto Superiore per la Protezione e la Ricerca Ambientale) database.

The collected data formed a substantial database that facilitated numerous GIS (Geographical Information Sistem)-based analyses and processing, aimed to redefine the surface geology with high accuracy and to determine the RS thickness. Due to their

high compressibility, RS have been recognized in various previous studies as lithology responsible for site-specific seismic amplifications (Amoroso et al., 2018; Del Monaco et al., 2013; Durante et al., 2017; Mannella et al., 2019; Martelli et al., 2012; Nocentini et al., 2017a; Tallini et al., 2020).

The produced geological map was rasterized, assigning a Vs (Shear Wave Velocity) value to each lithology based on literature data from Downhole (DH) and Multichannel Analysis of Surface Waves (MASW in situ measurements (Amanti et al., 2020; Amoroso et al., 2018; Del Monaco et al., 2013; di Giulio et al., 2014; Lanzo et al., 2011; Macerola et al., 2019; Pagliaroli et al., 2020). Quartiles (first, second, and third quartiles) were calculated for the collected Vs values.

Quartiles are statistical values that divide an ordered dataset into four equal parts. They are widely used to analyze the distribution of a dataset and identify variability within it. The three main quartiles are:

- First Quartile (Q1): This value divides the lowest 25% of the data from the remaining 75% of the higher data. It indicates the point where 25% of the data is below, and 75% of the data is above.

- Second Quartile (Q2) or Median: This value divides the dataset into two equal parts, with 50% of the data below and 50% of the data above. It is the central value of the distribution.

- Third Quartile (Q3): This value divides the lowest 75% of the data from the top 25% of the data. It indicates the point where 75% of the data is below, and 25% of the data is above.

Quartiles are useful statistical tools for understanding the distribution and variability of data in a numeric dataset.

The assigned Vs value to the lithologies is the median (Q2).

Values of the RS thickness, as well as the groundwater level were interpolated using the Inverse Distance Weighted (IDW) method. The result of these interpolations is two

raster, depicting the variation of the RS thickness and piezometric level across the entire area within the city medieval walls.

A Digital Elevation Model (DEM) with a 5-meter resolution became necessary for assessing the elevation differences and calculating slopes. This was achieved using the dedicated "Slope" analysis algorithm available in the open-source software QGIS. Furthermore, through a subtraction operation between DEM and the groundwater elevation raster, carried out using raster calculator, it was possible to estimate the depth of the water table relative to the ground surface.

2.3 *Calculation of the Pearson correlation coefficient*

The PCC, often denoted as "*r*," is a statistical measure used to assess the linear relationship between two variables. It measures the strength and direction of the relationship between two continuous variables.

The formula to calculate the Pearson correlation coefficient (r) is as follows:

$$r = \frac{\sum[(X_i - \bar{X})(Y_i - \bar{Y})]}{\sqrt{\sum(X_i - \bar{X})^2 \sum(Y_i - \bar{Y})^2}}$$

Where:

r is the Pearson correlation coefficient

Xi and Yi represent each value respectively in the first and second dataset

$\bar{X}$ and $\bar{Y}$ are the mean of values respectively in the first and second dataset.

The PCC takes values between -1 and +1

$r = 1$ indicates a perfect positive correlation (when one variable increases, the other increases linearly)

$r = -1$ indicates a perfect negative correlation (when one variable increases, the other decreases linearly)

$r = 0$ indicates no linear correlation (the variables are not linearly related)

To calculate PCC between PF and SAR deformation, it was necessary to create a grid with a 10 m x 10 m mesh and spatialize data, in order to create continuous surfaces that were sampled at the centroids of each grid cell (Figure 4). In this way, each pixel was assigned a value for cumulative and vertical displacement, ground slope, RS thickness, piezometric level and Vs.

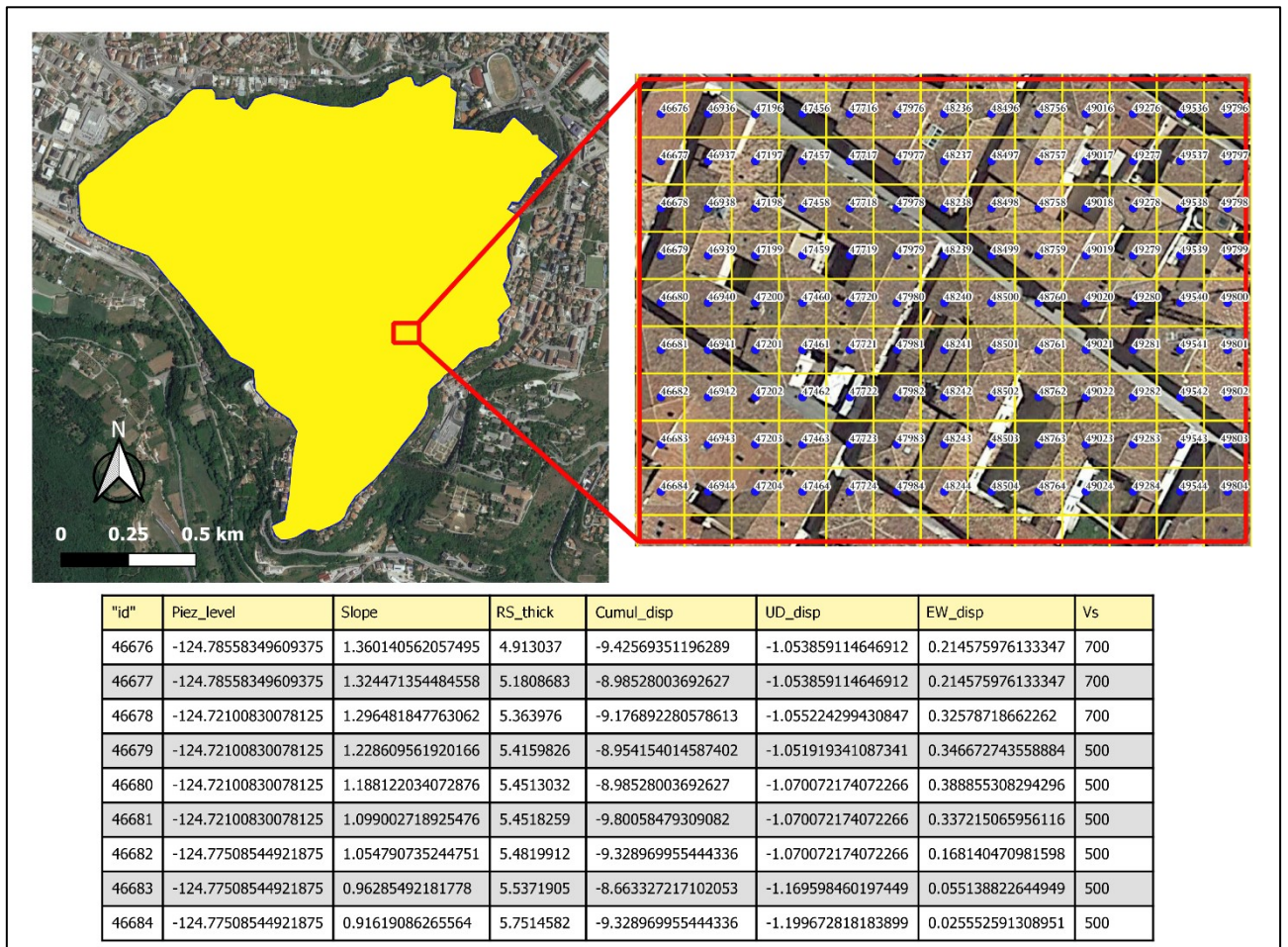| "id"	Piez_level	Slope	RS_thick	Cumul_disp	UD_disp	EW_disp	Vs
46676	-124.78558349609375	1.360140562057495	4.913037	-9.42569351196289	-1.053859114646912	0.214575976133347	700
46677	-124.78558349609375	1.324471354484558	5.1808683	-8.98528003692627	-1.053859114646912	0.214575976133347	700
46678	-124.72100830078125	1.296481847763062	5.363976	-9.176892280578613	-1.055224299430847	0.32578718662262	700
46679	-124.72100830078125	1.228609561920166	5.4159826	-8.954154014587402	-1.051919341087341	0.346672743558884	500
46680	-124.72100830078125	1.188122034072876	5.4513032	-8.98528003692627	-1.070072174072266	0.388855308294296	500
46681	-124.72100830078125	1.099002718925476	5.4518259	-9.80058479309082	-1.070072174072266	0.337215065956116	500
46682	-124.77508544921875	1.054790735244751	5.4819912	-9.328969955444336	-1.070072174072266	0.168140470981598	500
46683	-124.77508544921875	0.96285492181778	5.5371905	-8.663327217102053	-1.169598460197449	0.055138822644949	500
46684	-124.77508544921875	0.91619086265564	5.7514582	-9.328969955444336	-1.199672818183899	0.025552591308951	500

Figure 4: on the top is the 10m x 10m grid covering the entire historic center within the medieval city walls, which was used to sample the rasters for correlation purposes. Below, the table displays the values for each grid centroid, including piezometric level, RS thickness, terrain slope, cumulative vertical and horizontal displacement, and Vs of the outcropping lithologies.

2.4   *Analysis of seasonal ground movements and correlation with meteorological data*

Since any variations in the groundwater level, associated with seasonal variations in precipitation, lead to changes in pore pressure in the soil/rock column underlying the studied area, we expect to observe a correlation between seasonal variations in subsidence velocities and rainfall intensity values. In order to study such correlation, we used precipitation data provided by NASA (NASA, n.d.), in the form of daily and monthly time series. Both meteorological and subsidence data were preliminarily processed.

The time series of PS cumulative displacement values utilized here consist of an array in which each value is given by the average displacement of all PSs, located on the ground, in a certain time. The PSs locate on buildings have been excluded from this analysis, to remove the effect of seasonal thermal strain of buildings on the measured vertical PSs displacements. Such series have been analyzed by means of a detrended approach. Indeed, in addition to the water table oscillations, subsidence is associated with post-seismic consolidation phenomena of underlying soil and/or rocks, which evolve over time. To remove the effects of non-climatic factors, thus isolating seasonal variations, the oscillations of the series values compared to the long-term trend were considered. In particular, the deviations, or residuals, compared to a linear trend were considered. These deviations were then standardized as follows:

$$s = (r - m)/\sigma$$

where, *s* represents the standardized residual, *r* the values of the residuals, *m* and σ, respectively, their mean and standard deviation, calculated over the studied time range. Standardization makes the data independent of the unit of measurement adopted, thus allowing data series of different nature (such as rain intensity and cumulated displacements) to be compared.

As regards the precipitation data, the quarterly averages were calculated starting from the daily intensity values, i.e., the average of the intensity values of the previous three months was associated with each month. By way of example, the May quarterly average is equal to the average of daily intensities of March, April, and May. These values were also standardized according to the aforementioned formula, considering the

residuals with respect to a horizontal trend (i.e., compared to the average value of the whole series). Since only the water that actually infiltrates the ground feeds the aquifer, the daily data was preliminarily further corrected, according to a model that took into account the fact that in case of intense rainfall, the flow of runoff water increases. In order to determine a first approximation estimate of the proportion between infiltration and runoff water, the following simple linear model with saturation was utilized:

$p = i$, for $i <= i_{tr}$;

$p = i_{tr}$, for $i > i_{tr}$;

where p denotes the flow rate per m^2 of infiltrated water, i the rainfall intensity and i_{tr} an appropriate threshold value to be determined. Namely, according to this model, when the intensity is lower than the threshold value, all the rainwater infiltrates. When the intensity exceeds the threshold value i_{tr}, only the quantity equal to i_{tr} infiltrates, whereas the excess forms runoff water. Based on these corrected intensity values, quarterly averages were calculated.

Then, the cross-correlation was carried out between time series of average precipitation intensity and average monthly cumulative displacement of all ground PSs, for the entire monitoring period (from April 2010 to November 2021). The unknown variables to be determined through this analysis were the i_{tr} threshold value and the time shift between the two series. These values were determined by finding the pair of values, in the (*itr*, shift) plane that maximized the correlation between the two considered series.

3. Results

The A-DInSAR map obtained from Cosmo-SkyMed images acquired between April 2010 and November 2021 in the descending orbit shows more pronounced deformations in the south and southwest LAHC. In Figure 5, the interferometric data has been interpolated to spatialize the deformation over the study area, and from this map, areas characterized by deformation of more than -1 mm/year have been extracted.

P1 and P2 serve as two selected measurement points to illustrate the deformation trends of the PSs in the eastern-northeastern and southern-southwestern sectors of

LAHC. Deformations recorded along the satellite's Line of Sight (LOS) exhibit significant variation from north to south, ranging from no deformation to a cumulative displacement exceeding -25 mm over an 11-year period. In the map depicted in Figure 5, stable areas are shown in green, while areas moving away from the satellite are indicated by colors ranging from yellow to orange.
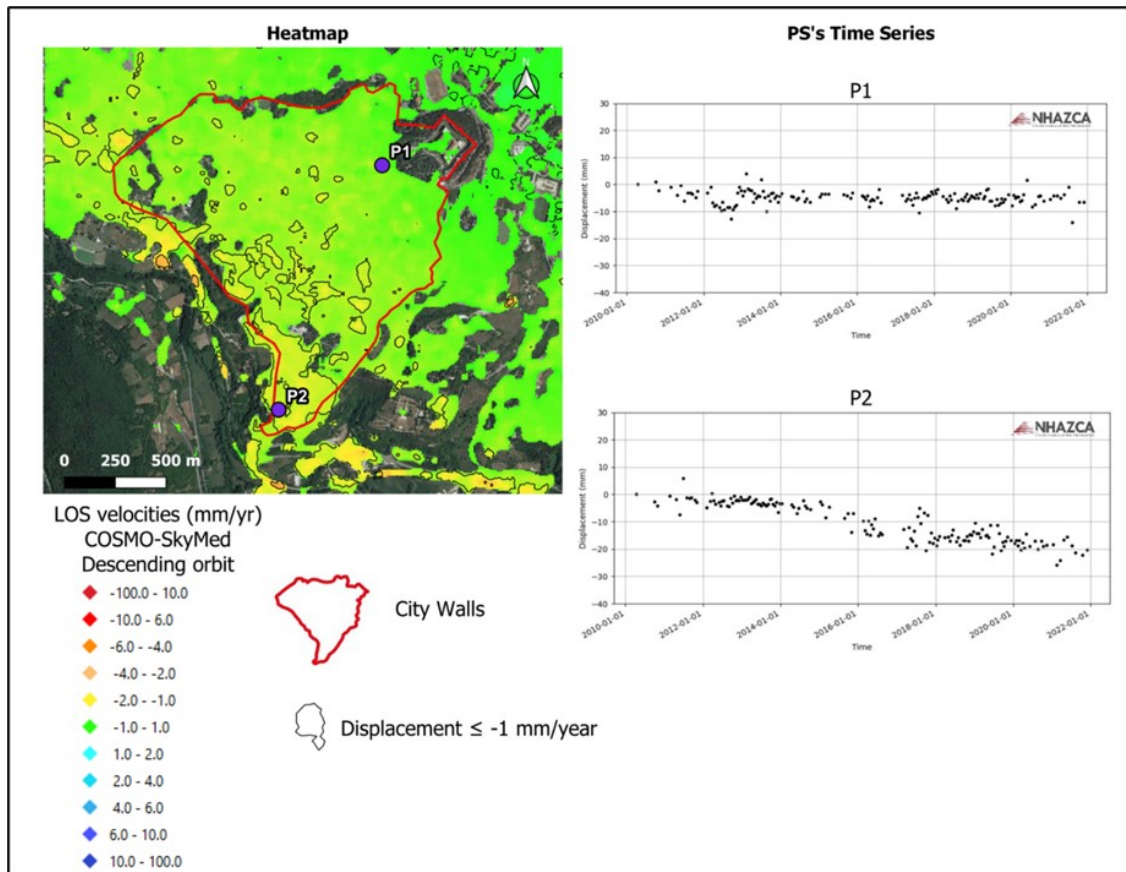

Figure 5: A-DInSAR map obtained from Cosmo-SkyMed images acquired between 2010 and 2021 in the descending orbit and interpolated to spatialize the deformation. Stable areas are shown in green, while areas moving away from the satellite are indicated by colors ranging from yellow to orange. Black line indicates areas characterized by more pronounced deformation (more than -1 mm/year). Blue points (P1 and P2) are two PSs used for illustrating deformation trend in northern and southern sector of the study area.

3.1. Horizontal and vertical deformation of L'Aquila hill

In order to assess the horizontal and vertical components of PSs displacement, the data fusion between Cosmo-SkyMed and Sentinel-1 images were carried out. More detailed information about the algorithm and the number of images used is reported in the Materials and Methods chapter (2.1). The results of decomposing the deformation into its two components, horizontal and vertical, are depicted in the maps in Figure 6. in which the color scale used to represent vertical and horizontal PSs displacement is the same of that of Figure 5. In the vertical displacement map, warm colors indicate PSs experiencing subsidence (i.e., those with negative velocity, moving away the satellite), while cool colors represent points exhibiting uplift (i.e., with positive velocity, approaching to satellite). As for the horizontal displacement map, PS with negative velocity (ranging from yellow to red) are associated with westward movement, while those with positive velocity (ranging from cyan to blue) indicate eastward movement. In both maps, points with mild deformations falling within the range of -1 to 1 mm/year are represented in green.
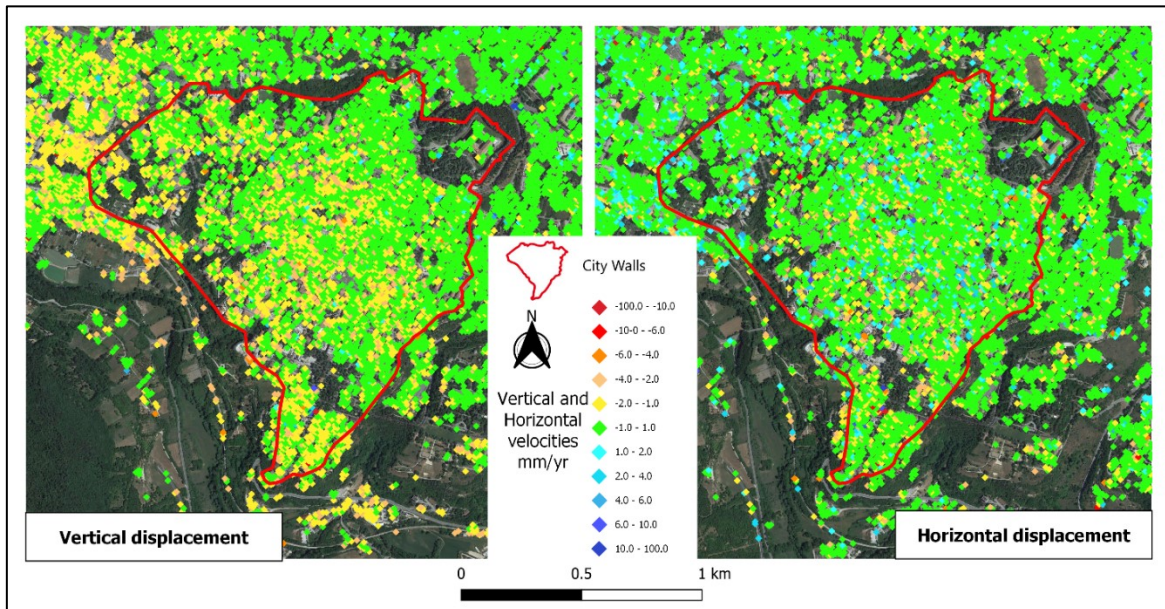

Figure 6: vertical and horizontal A-DInSAR map obtained from the data fusion between COSMO-SkyMed descending April 2010 – November 2021 and Sentinel-1 ascending October 2014 – August 2022 images. For the representation of vertical velocities warm colors indicate PSs experiencing subsidence, while cool colors represent points

exhibiting uplift. In the horizontal map points with positive velocities, depicted in cyan and blue, are the ones moving eastward, while PSs with negative velocities, depicted in yellow and orange, represent points moving westward.

From the map in Figure 6, it can be observed that subsidence is distributed across the entire study area, with a more pronounced character in the southwestern LAHC sector. In contrast, horizontal displacement is characteristic of a smaller number of PS and does not exhibit a preferred direction. For this reason, the horizontal displacement map in calculating the PCC has not been used.

3.2 Identification of factors predisposing deformation

To unravel the causes of the ground deformations, we first identified the geological and geomorphological factors that can possibly influence them. We conducted a detailed analysis of the central area of L'Aquila (LAHC) within the medieval walls, which is the focus area for our study.

Considering a careful review of the existing literature it has emerged that the geological characteristics of the substrate upon which the L'Aquila's buildings are constructed can be responsible for various seismic amplification effects and the nature of the rocks and sediments exposed in the study area can have a significant impact on seismic amplification (Amoroso et al., 2018; Del Monaco et al., 2013; Durante et al., 2017; Mannella et al., 2019; Martelli et al., 2012; Nocentini et al., 2017a; Tallini et al., 2020). Moreover, through a geomorphological and hydrogeological study of the area the following predisposing factors (PF) were selected:

- thickness of the Red Soils (RS);

- surface lithology;

- terrain slope;

- water table depth

In considering surface lithology, it is worth noting that only lithology with a minimum thickness of 2 m has been mapped.

The area is situated on a flat top hill where elevations range from 628 m a.s.l. to 736 m a.s.l. (Figure 7a). A difference in elevation of over 100 meters in 2 km² is necessarily accommodated by areas with potentially steep slopes (Figure 7b), a characteristic that can influence displacements. The multilayer porous aquifer of the intermontane plain, in which is located LAHC, constituted by the Quaternary detrital formations, may be represented hydrogeologically with a unique reference water table with centripetal groundwater flowpaths. This aquifer is dominantly recharged by the surrounding carbonate reliefs acting as regional aquifer (Petitta & Tallini, 2003). By observing the section of Figure 8, the carbonate aquifer outcrops in the northern sector, while it is mainly buried in the southern one by the Quaternary formation (LAB and MDS). The coarse-grained L'Aquila Breccia (LAB) and low-permeability fine-grained MDS formation act as local aquifer and aquitard respectively. In the northern sector the carbonate aquifer is unconfined because only the LAB aquifer overlays on top on it with a negligible thickness, while in the southern one the carbonate aquifer is semi-confined due to the overlaying on it of the MDS aquitard with a considerable thickness of 200-400 m. Moreover, in the southern sector, LAB, behaving as a local perched aquifer, overlays the MDS formation so that LAB feeds minor springs in the southern slope of L'Aquila hill [39] (Fig. 8). The water table varies from West to East between 590 and 640 m a.s.l. with the groundwater flowing towards the SE (Fig.7c). It is shallower in the W part of the city and deeper in the NE (Figs. 7,8). MDS aquitard plays an important role in the LAHC hydrogeological setting because it, as well as being groundwater saturated, partly confines laterally the regional carbonate aquifer.
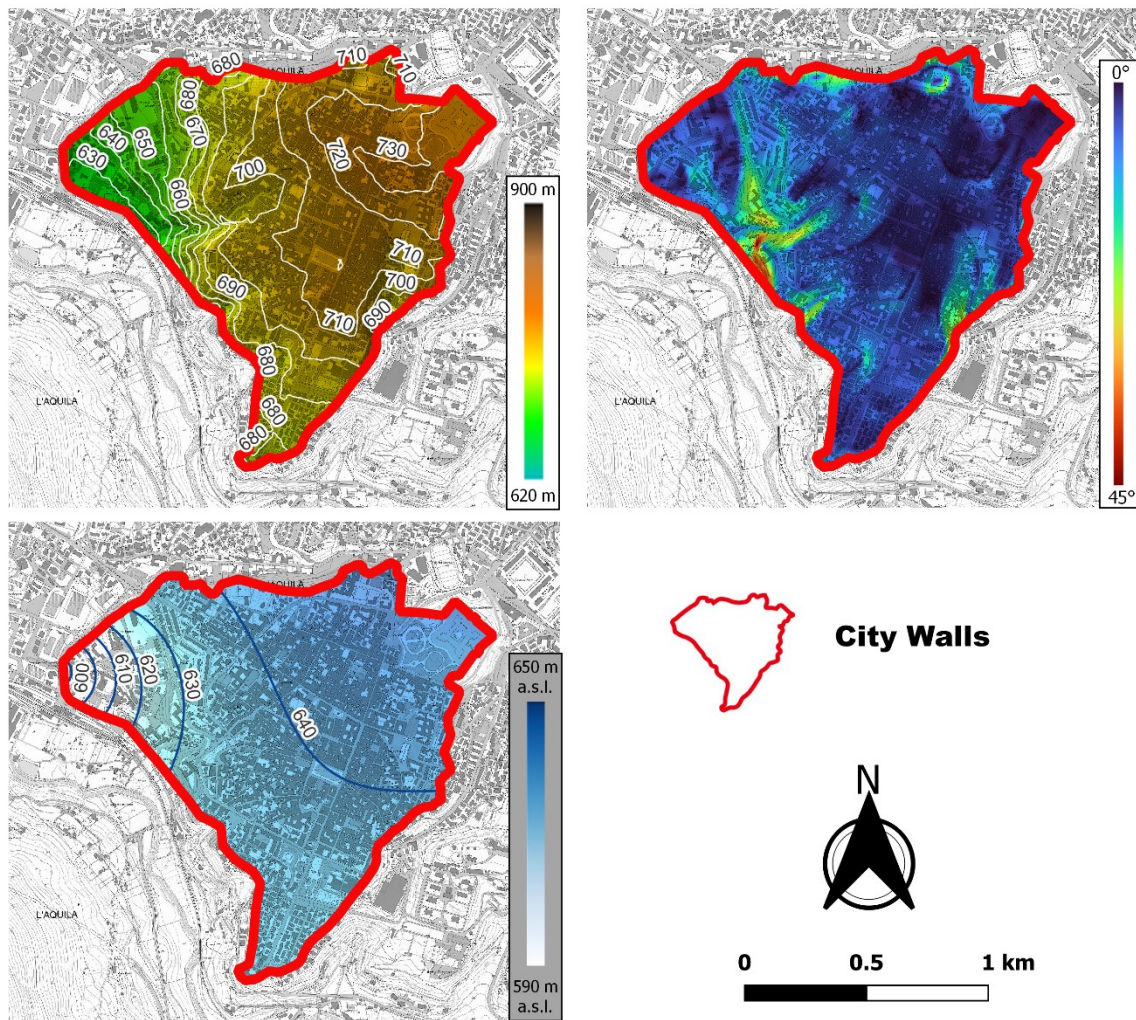
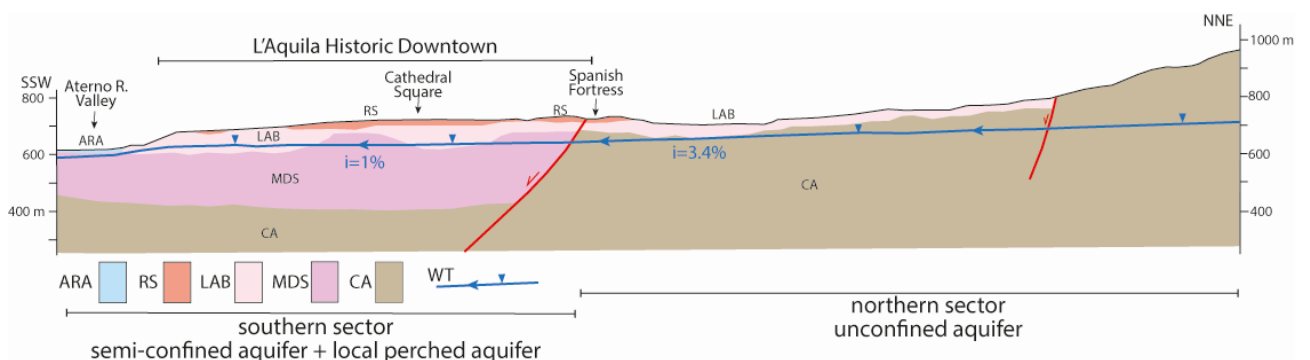Figure 7: a) ground elevation (m a.s.l.); b) terrain slope (°); c) water table (m a.s.l.).

Figure 8: LAHC hydrogeological section. ARA: Aterno River alluvium, gravel, sand, silt (local aquifer); RS: Red Soil (local aquiclude-aquitard); LAB: L'Aquila Breccia,

gravel and breccia mixed with sand and silt (local aquifer); MDS: Madonna della Strada Formation, clayey silt and sand (aquitard); CA: carbonate aquifer; WT: water table; i: hydraulic gradient.

Numerous scientific contributions suggest that the varying amplification effects recorded on LAHC buildings during the 2009 earthquake may be correlated with the extreme variability in terms of thickness and lithology of the continental deposits filling the Plio-Quaternary graben upon which the city was built (Amoroso et al., 2018; Del Monaco et al., 2013; Durante et al., 2017; Mannella et al., 2019; Nocentini et al., 2017a)). In particular, [20,24] considered the RS as a determining factor in the distribution of deformation and observed damage intensity. In (Tallini et al., 2020) through an analysis of HVSR microtremor data, a peak in the mid-frequency microtremor range (f1, 3-13 Hz) was recognized, partly related to the variation in thickness and areal distribution of the RS. In terms of seismic risk, this peak can result in seismic coupling between the frequencies of shallow lithologies and the fundamental frequency of buildings. The authors estimated that 80% of the buildings severely damaged or destroyed by the 2009 earthquake could experience such seismic coupling.

In this context, it is necessary to redefine the LAHC geological map with such detail that it allows for an analysis of deformations at the scale of individual buildings. Indeed, the high number of PSs in the study area and the resolution of SAR images enable us to extend the analysis to a large scale.

3.3 Borehole stratigraphy and redefinition of geological mapping

We analyzed the logs of 573 boreholes of the USRA database (Ufficio Speciale per la Ricostruzione dell'Aquila, n.d.). They were performed in LAHC (Figure 9) and permitted to create a highly detailed geological map capable of accurately representing the lithological differences in the study area. The map allowed us, first and foremost, to describe the spatial variability of the RS thickness.
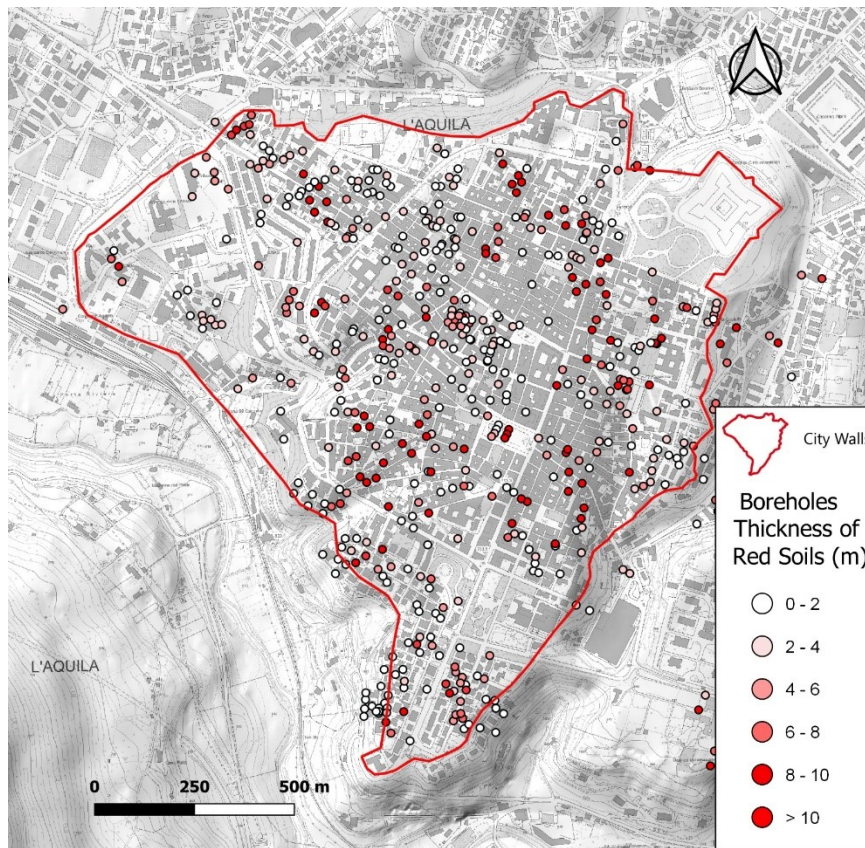
Figure 9: 573 boreholes classified with RS thickness.

By integrating borehole stratigraphy with literature data mentioned above, we produced the geological map in Figure 10 b, which, compared to the map [12] (Fig. 10 a), provides a higher level of detail, allowing for a millimetrically accurate comparison between geological data and A-DInSAR deformations. The main points of novelty are as follows: anthropic deposits (ANT) have been mapped in all areas where it has a thickness of >2 m; a significant reduction of RS was implemented only in areas where they were encountered in boreholes. It's worth noting that the new map is limited to the medieval city wall, the focus of this study (LAHC).

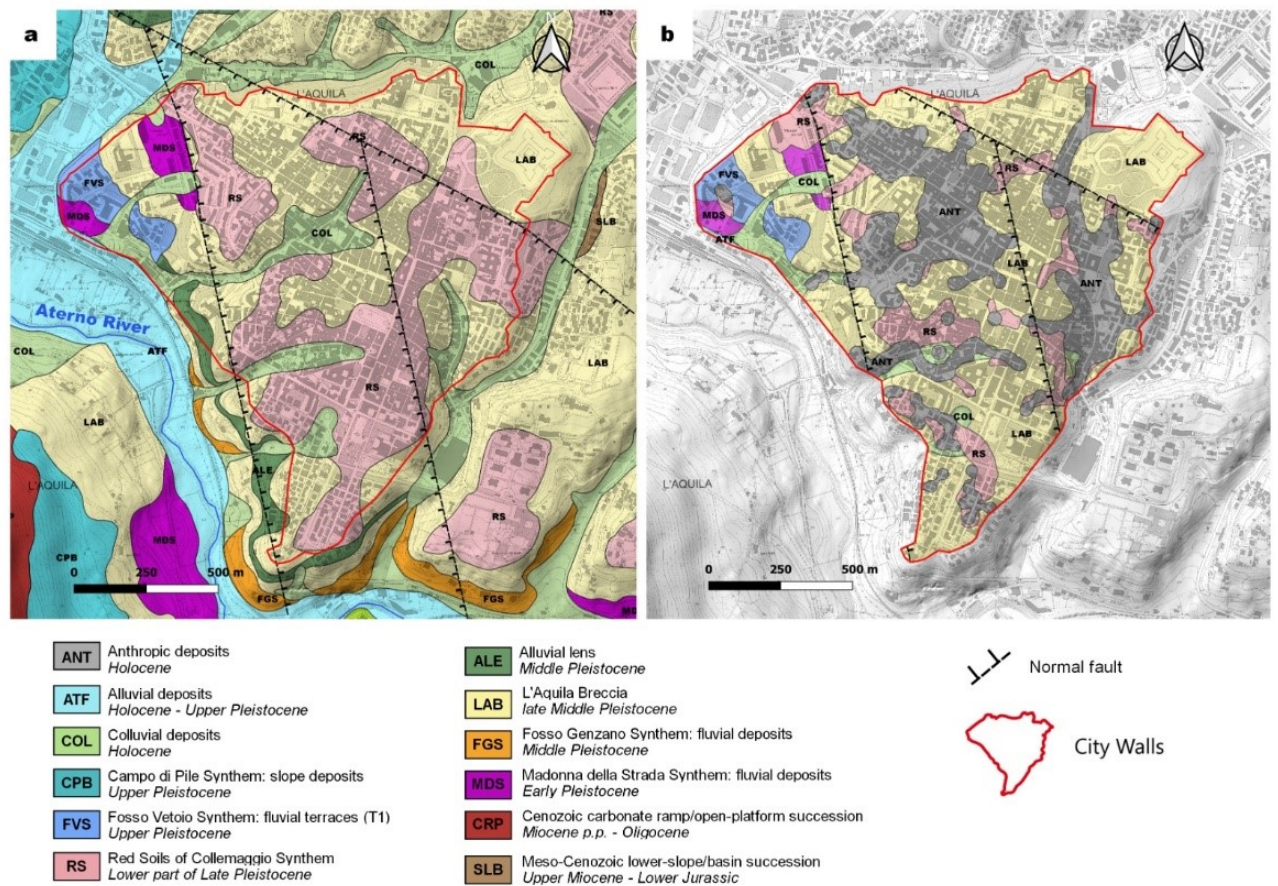| ANT | Anthropic deposits
Holocene | | ALE | Alluvial lens
Middle Pleistocene |
ATF	Alluvial deposits *Holocene - Upper Pleistocene*		LAB	L'Aquila Breccia *late Middle Pleistocene*
COL	Colluvial deposits *Holocene*		FGS	Fosso Genzano Synthem: fluvial deposits *Middle Pleistocene*
CPB	Campo di Pile Synthem: slope deposits *Upper Pleistocene*		MDS	Madonna della Strada Synthem: fluvial deposits *Early Pleistocene*
FVS	Fosso Vetoio Synthem: fluvial terraces (T1) *Upper Pleistocene*		CRP	Cenozoic carbonate ramp/open-platform succession *Miocene p.p. - Oligocene*
RS	Red Soils of Collemaggio Synthem *Lower part of Late Pleistocene*		SLB	Meso-Cenozoic lower-slope/basin succession *Upper Miocene - Lower Jurassic*

Normal fault

City Walls

Figure 10: a) geological map modified from (Nocentini et al., 2017a); b) new detailed geological map resulting from the analysis of 573 boreholes database and literature data.

Therefore, starting from the new geological map, we selected some representative PSs located on RS and exposed LAB, and analyzed their time series.

In the A-DInSAR map created with descending Cosmo-SkyMed images, shown in Figure 11, the blue dots indicate the location of measurement points positioned on LAB, while the red dots represent those on RS. The scatterers for which time series are provided are located near boreholes S566, S544, S339, and S110. The time series of PSs located on RS reveal the presence of similar LOS deformations in different areas of LAHC, with cumulative displacement values reaching -20 mm. Conversely, the time series of the two PS points located on LAB highlight a significant difference in deformation behavior. In the northern sector, where S566 is located, deformations are

mild, with a cumulative displacement value of approximately -5 mm over 11 years. On the contrary, borehole S339, situated southwest of LAHC, exhibits very pronounced deformations, with a cumulative displacement of -28 mm.
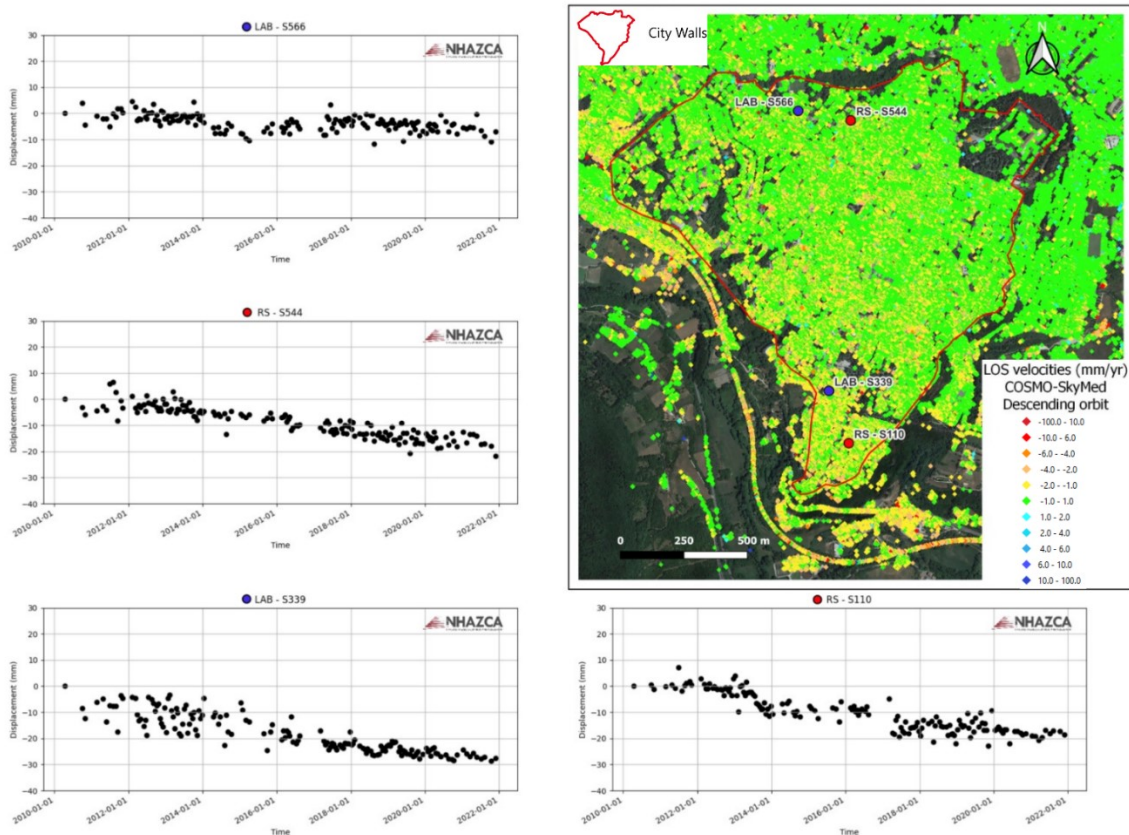

Figure 11: Time series Cosmo-SkyMed descending PSs located on LAB (blue dots) and RS (red dots). In the A-DInSAR LOS descending orbital geometry map green PSs are considered as stable; yellow-red PSs are moving away from the satellite; cyan-blue PSs are moving toward the satellite.

3.4 Geophysical data – Vs

Once the LAHC geology was redefined, it was necessary to assign a numerical value to each outcropping lithology for calculating the correlation between satellite-detected deformations and geology. To achieve this, we use Vs values from literature data (Amanti et al., 2020; Amoroso et al., 2018; Del Monaco et al., 2013; di Giulio et al., 2014; Lanzo et al., 2011; Macerola et al., 2019; Pagliaroli et al., 2020).

Q_1, Q_2, and Q_3 calculated for each lithology based on the Vs data are reported in Table 1 and summarized by the boxplot in Figure 12a. Quartiles provide information about data dispersion and can be used to identify any deviations or significant features in the distribution. The boxplot in Figure 12a illustrates the extreme variability of Vs values within LAB, with values ranging from 200 to 1200 m/s, distributed as shown in the histogram in Figure 12, panel b, where the Vs values of LAB are subdivided into three intervals, defined by red dashed lines in the same figure.

Table 1: Q_1, Q_2, and Q_3 calculated based on the Vs literature data for each outcropping lithology.

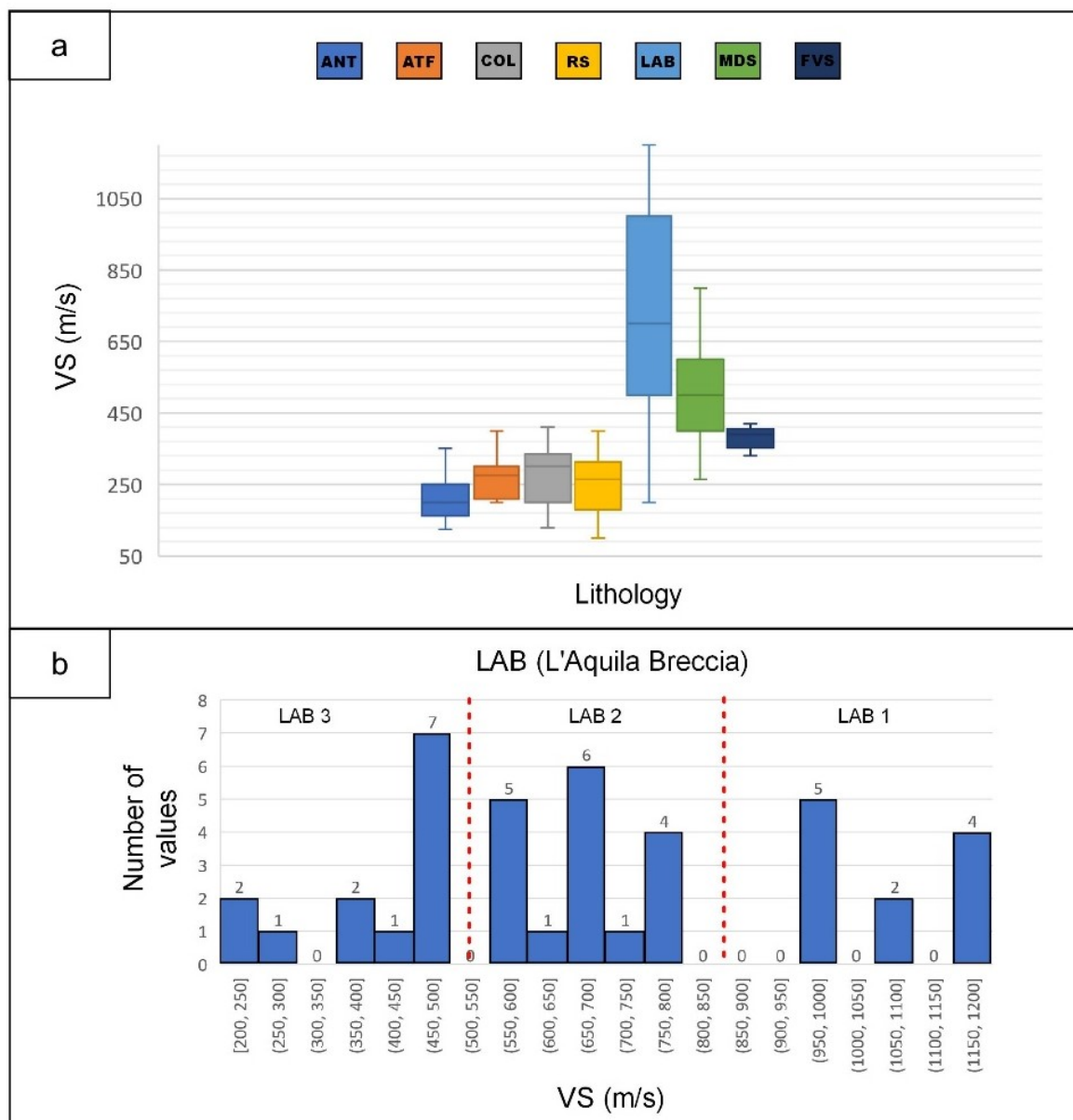| Lithology	Q_1	Q_2	Q_3
ANT	167.5	200	250
ATF	230	275	300
COL	200	300	320
RS	180	265	300
LAB	500	700	1000
MDS	400	500	600
FVS	364.25	390	400

Figure 12: in panel a, the boxplot of Vs data (summarized in table 1) shows high variability of LAB Vs values, ranging from 200 to 1200 m/s. The distribution of Vs values (number of values) is represented in panel b. The dashed red lines separate the Vs of the LAB into three intervals.

For this reason, through a careful analysis of borehole stratigraphy and the lithological characteristics of the LAB in LAHC, we divided LAB into three categories based on the abundance of the fine-grained fraction. In the southern sector, LAB with a significant

silty fraction is exposed (LAB 3), to which Vs values ranging from 200 to 500 m/s have been associated. In the central zone of LAHC, the amount of silt within the LAB decreases, and the Vs values rise to 500 – 800 m/s (LAB 2). Finally, in the northern and northeastern sectors, the silty fraction is almost absent, and the Vs values are higher, ranging from 950 to 1200 m/s (LAB 1). This internal division within LAB is depicted in the geological map in Figure 13, while Table 2 presents the Vs values (Q_1, Q_2, Q_3) calculated for each outcropping lithology, based on the distinction of LAB into three categories, along with the associated VS/lithology boxplot (Figure 14). In Table 2 is also reported the number of Vs measurement used in calculation of Vs median (Q_2).
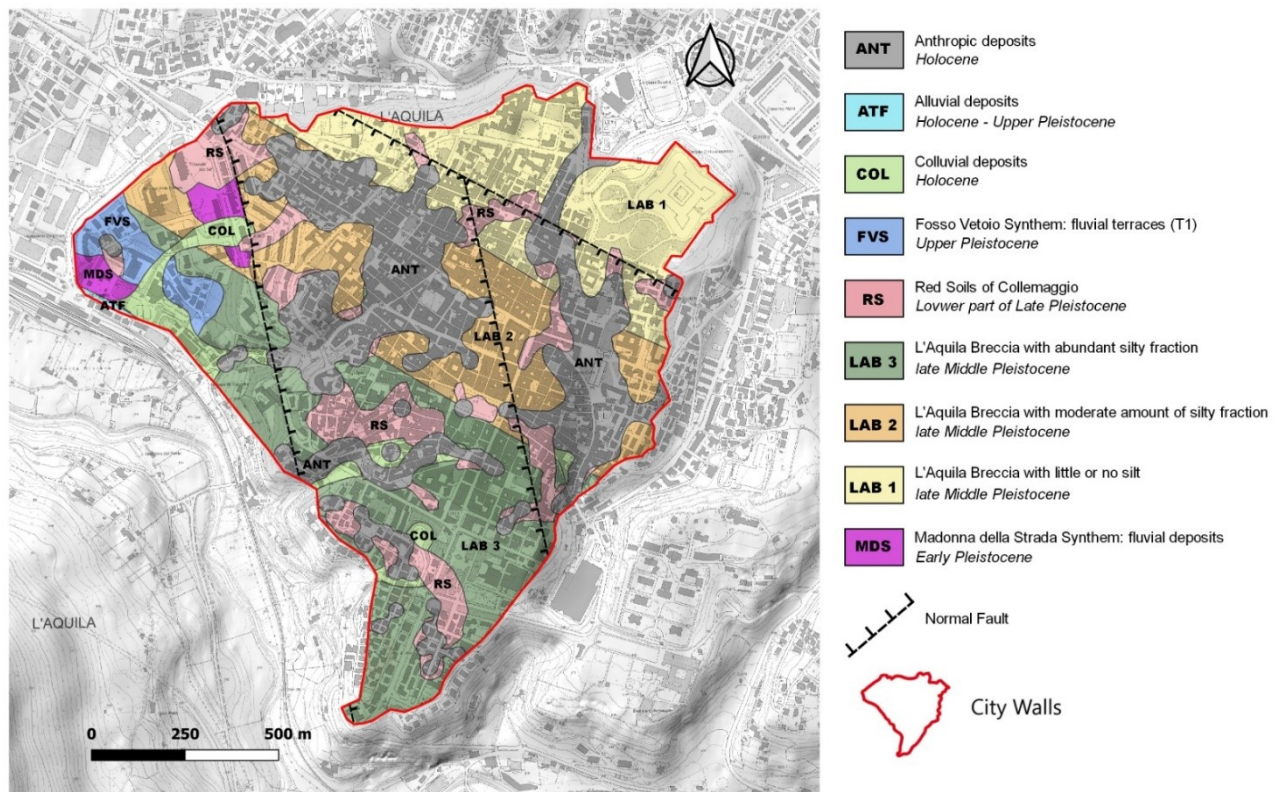

Figure 13: geological map with an internal division of LAB based on the abundance of the muddy-limestone matrix. From LAB 1 to LAB 3 the silt fraction increases and the Vs decreases (cfr. Tab.2).

Table 2: Vs values (Q1, Q2, Q3) calculated for each outcropping lithology, based on the distinction of LAB into three categories (LAB 1, LAB 2, LAB 3), depicted in Figure13.

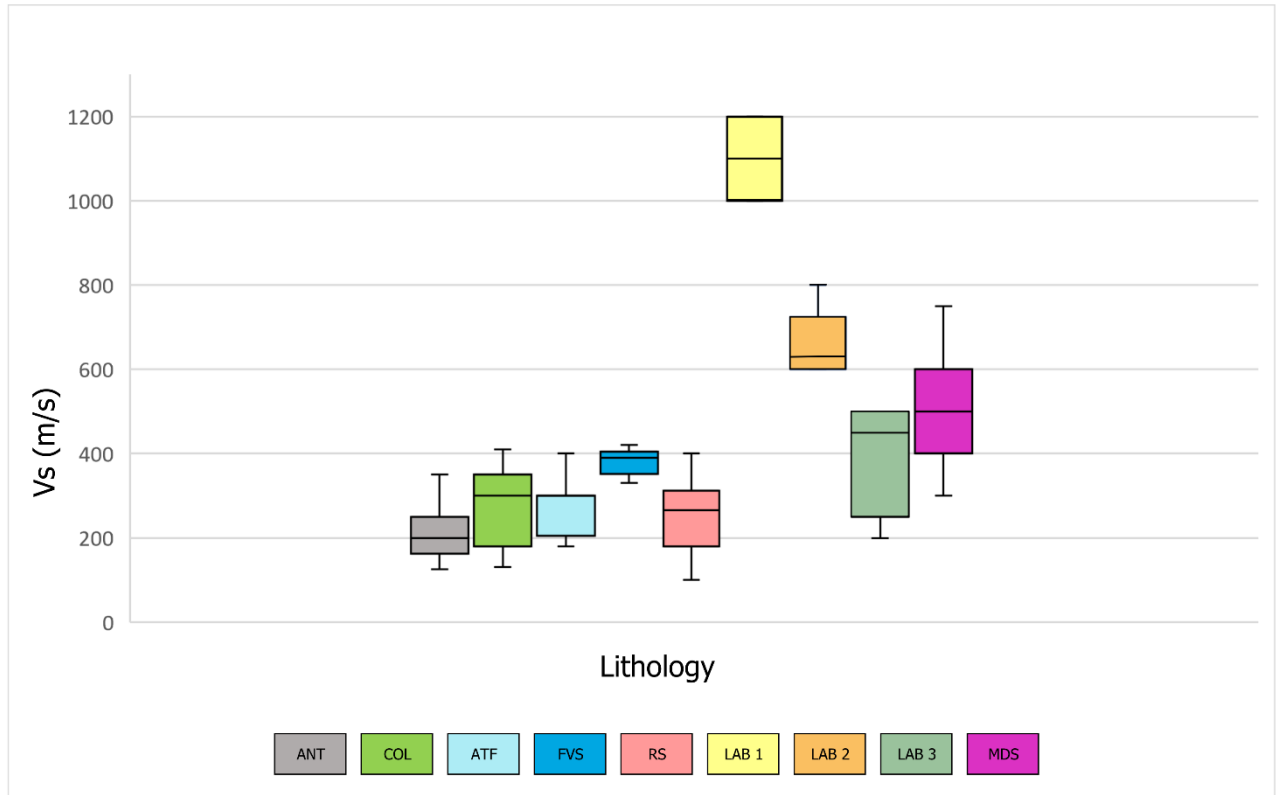| Unit	Number of Vs Data	Q1 (m/s)	Q2 (m/s)	Q3 (m/s)
ANT	16	167,5	200	250
COL	25	200	300	320
ATF	11	230	275	300
FVS	6	364.25	390	400
RS	10	180	265	300
LAB 1	11	1000	1100	1200
LAB 2	17	600	700	750
LAB 3	13	400	500	500
MDS	35	400	500	600

Figure 14: boxplot of Vs data considering the classification of LAB presented in Table 2 and Fig. 13.

3.5 Calculation of Pearson's Correlation Coefficient (PCC)

Through the calculation of the PCC, we verified the relationship between the geological-geomorphological and hydrogeological PF represented in Figure 15 and deformation in LAHC. We compared the cumulative displacement (obtained from the interpolation of Cosmo-SkyMed descending velocity values) and vertical deformation (obtained from the interpolation of velocity values resulting from the decomposition of velocities calculated by combining Cosmo-SkyMed descending and Sentinel-1 ascending) represented in Figure 16, with slope maps, RS thickness, depth of regional aquifer and the Vs of the outcropping geology. For a step-by-step description of the

method used, please refer to the Materials and Methods chapter - Pearson Correlation Coefficient calculation (2.3).
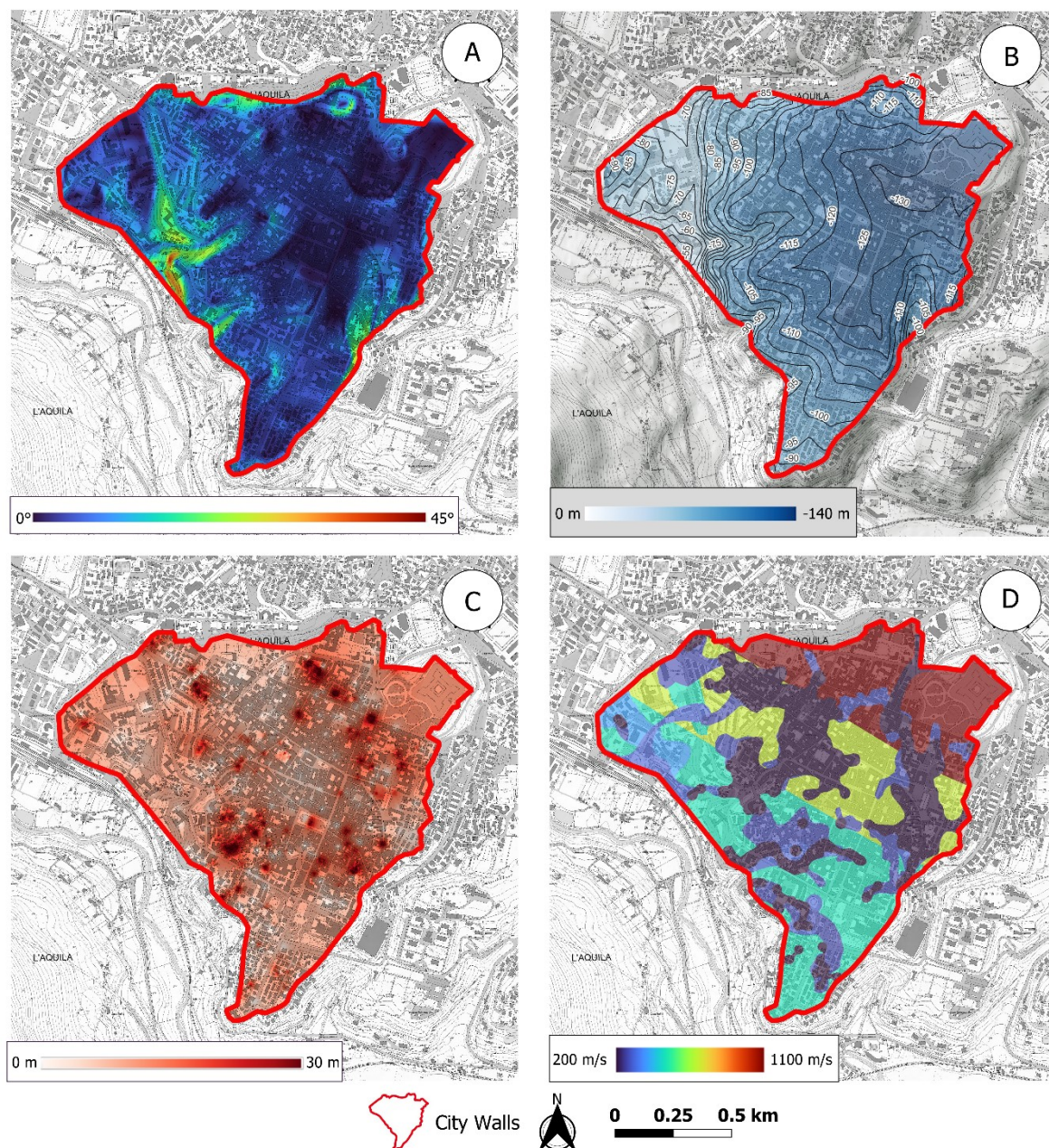

Figure 15: geological-geomorphological and hydrogeological predisposing factors (PF) are represented. Panel A is for ground slope (°); panel B, for RS thickness (m); panel C

for water table depth (m below ground level); panel D for Vs (m/s) of the outcropping lithologies.
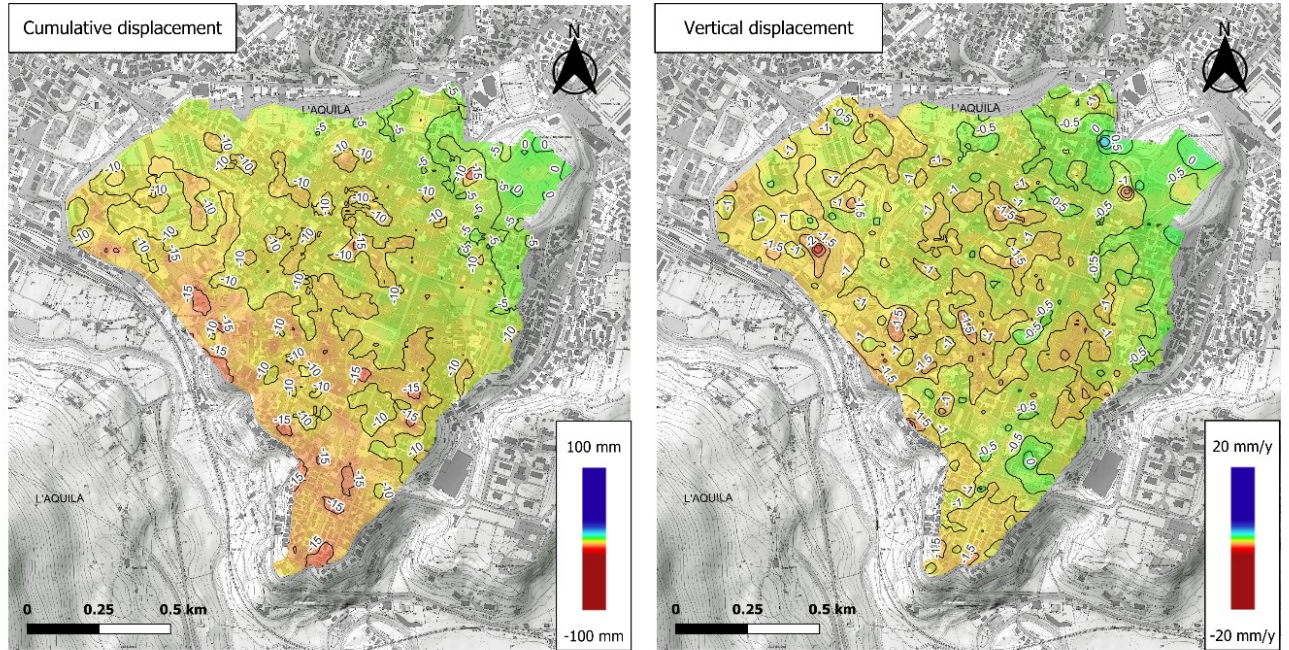
Figure 16: on the left, cumulative displacement map (obtained from the interpolation of Cosmo-SkyMed descending orbit velocity values). Green area areas considered as stable; yellow-red areas are moving away from the satellite; cyan-blue areas are moving toward the satellite. On the right, vertical deformation map (obtained from the interpolation of velocity values resulting from the decomposition of velocities calculated by combining Cosmo-SkyMed descending and Sentinel-1 ascending orbit). In the vertical deformation map warm colors indicate areas experiencing subsidence, while cool colors represent areas exhibiting uplift.

Table 4 shows the results obtained from the correlation between cumulative and vertical displacement, and PF.

Predisposing Factors	Cumulative displacement (mm)	Vertical displacement (mm/a)
Depth of regional aquifer	-0.394609509	-0.521570082
Ground slope	-0.211930302	-0.223682426
Red Soils thickness	0.179659561	0.12674804
Vs of outcropping geology	0.467233498	0.459702848

3.6 Correlation between subsidence fluctuations and precipitations

The figs. 17 A and B show the result of detrending the time series of average displacements (i.e., spatially averaged over the studied area). The values in ordinates in the diagram of fig. 17 B are given by the standardized fluctuations of the curve in fig. 17 A, compared to the trendline. The orange curve in fig. 17 B represents the standardized values of quarterly precipitation. The fig 17 C shows the result of the cross-correlation analysis, involving the corrected and standardized precipitation values (see Section 2.4 in Methods), in which the runoff threshold precipitation and the temporal shift were estimated, by maximizing of the correlation value. The optimal values of these unknowns are given by threshold rainfall intensity of 4.7 mm per day and zero shift (note, however, that the quarterly data is already delayed, as it is a moving average over three months). The July 2018 displacement standardized residual value (circled in red in Fig. 17 A and B) has been removed as it is a suspected outlier. Indeed, it presents the maximum positive deviation of the entire series in a period of the year in which the deviations are systematically negative. The two standardized time series of detrended PS displacement and quarterly precipitation exhibit a notable degree of history matching, thus highlighting a significant relationship between the seasonal variations in subsidence on the rainfall rates of the previous months. Fig. 17 D shows the linear regression, with the relative squared correlation coefficient, between the two considered time series. Each point in the diagram has the displacement value measured

on a certain date as its ordinate, and the precipitation value on the same date as its abscissa (in terms of standardized and corrected values).
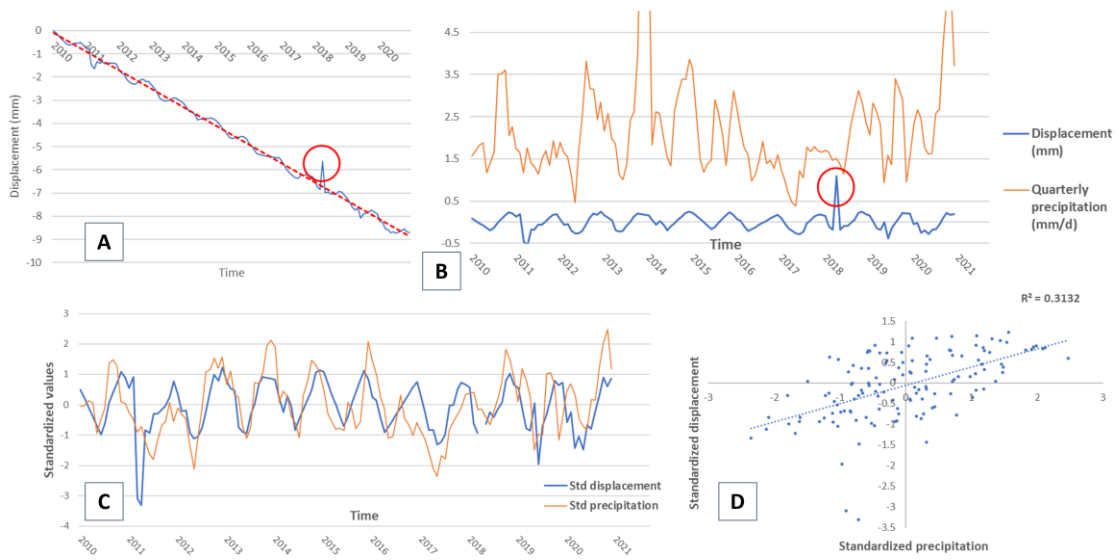

Figure 17: A) and b) result of detrending the time series of average displacements (i.e., spatially averaged over the studied area); B) values in ordinates in the diagram are given by the standardized deviations of the curve panel A compared to the trendline. The orange curve represents the standardized values of quarterly precipitation; C) result of the cross-correlation analysis by maximizing of the correlation value; D) linear regression, with the relative correlation coefficient (R^2), between the two considered time series.

4. Discussions

Many studies suggest that the differences in seismic amplification observed in LAHC buildings during the 2009 and 1703 earthquakes could be associated with the significant variation in the characteristics of continental sediments filling the Plio-Quaternary graben upon which the city was built (Amoroso et al., 2018; Del Monaco et al., 2013;

Durante et al., 2017; Mannella et al., 2019; Martelli et al., 2012; Nocentini et al., 2017a; Tallini et al., 2020). Since (Sciortino et al., 2023), through an A-DInSAR analysis conducted with Cosmo-SkyMed images captured between 2010 and 2021, observe a systematic increase in subsidence rate with increasing seismic damage (for both the 2009 and 1703 events), our results demonstrate that greater damage can be explained by geological and hydrogeological conditions: the PCC (tab. 4) shows a positive correlation between satellite-detected displacements and the Vs values and a negative correlation between InSAR velocities and the depth of regional aquifer. Indeed, the lower the Vs, the greater the InSAR deformation and the greater the depth of the water table, the less the deformation (both in terms of subsidence and cumulative deformation along the LOS).

From the decomposition of PS velocities into H (horizontal) and V (vertical) components, subsidence is recognized as the main deformation feature in L'Aquila, indicating that the primary component of displacement is vertical. The PCC between Vs and Cumulative Displacement and between Vs and Vertical Displacement is almost identical. On the contrary, for the water table depth, there is an anticorrelation, with the highest PCC value observed in the case of vertical displacement rather than cumulative deformation.

The production of a new geological map required the integrated use of site-specific geological and geophysical data from literature. The collection of Vs measurements to associate with outcropping lithologies highlighted significant variability in LAB, whose lithological and textural differences had already been identified by (Antonielli et al., 2020b) but had not been represented in the LAHC geological maps until now. They recognized two different levels in LAB: a lower level with a massive structure and grain-supported, containing blocks ranging in size from decimeters to meters, which directly overlies the bedrock and predates Quaternary deposits; the upper level is mud-supported and contains smaller blocks ranging from centimeters to a few decimeters.

In Figure 18, photos of LAB lithologies encountered in boreholes to the north, center, and south of LAHC are presented, corresponding to S566, S263, and S339, respectively. In the first case, the LAB lithology appears competent (lithoid, with a sparse matrix),

while in the southern breccias, the silty fraction is predominant. The LAB outcropping in the central sector of LAHC represents a transitional zone with approximately 50% silty matrix and 50% clasts.
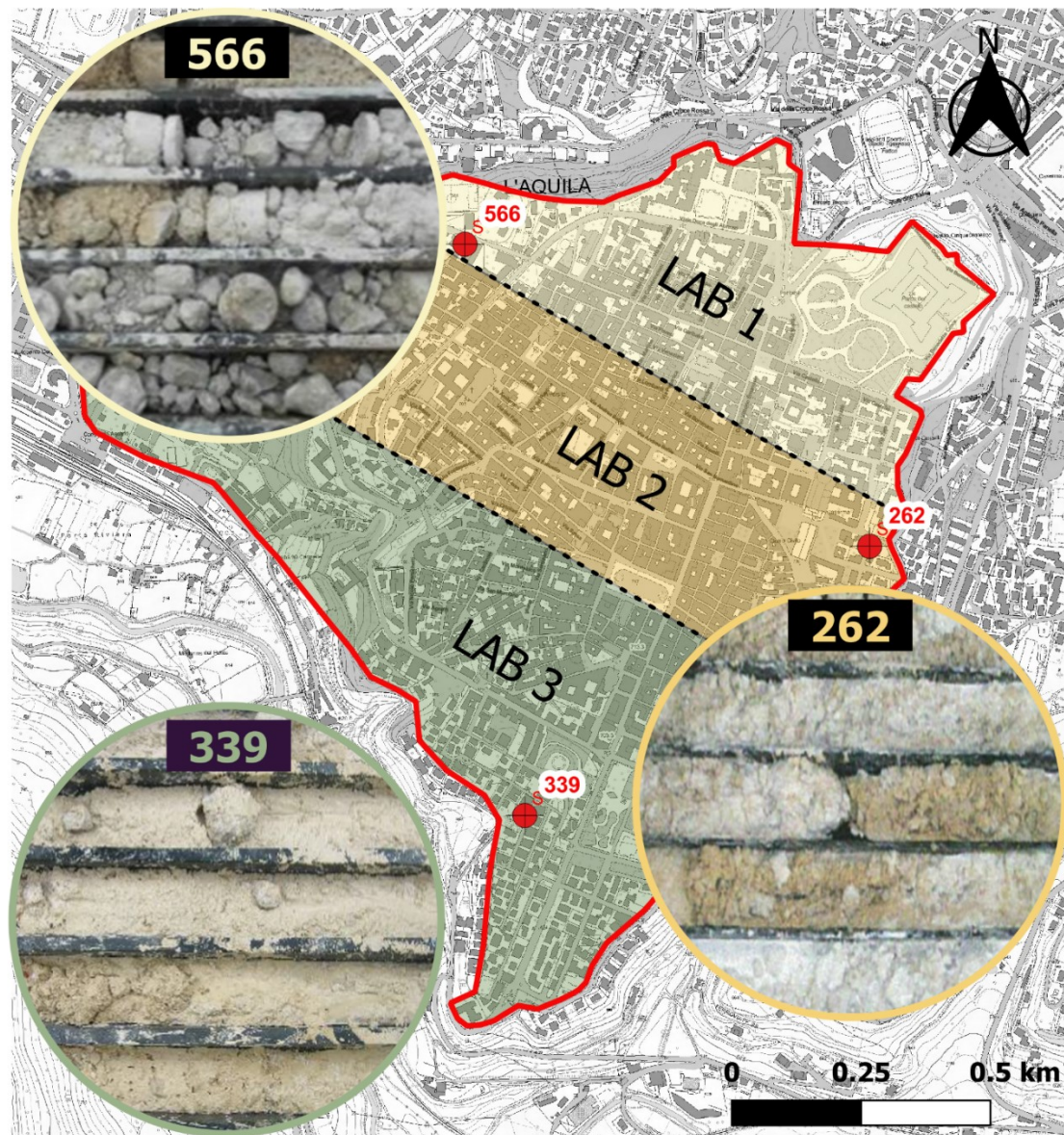

Figure 18: the variation in silty matrix content is shown in photos of the L'Aquila Breccias encountered in boreholes to the north (S566), center (S262), and south (S339) of the study area.

The increase towards South of the silty fraction of LAB is probably due to the emplacement of LAB as a gravitative deposit coming from the north, i.e. from the Gran Sasso chain, in the NW-SE oriented alluvial valley of the paleo Aterno River, which is transversal to the LAB source (Antonielli et al., 2020b). In the distal area of LAB lithosome (LAHC southern sector) the sediment is mixed: the fine-grained and coarse-grained fraction belong to the alluvial sediment pertaining of the paleo-Aterno River and the gravitative deposit, respectively.

The variability in Vs values within the LAB necessitated mapping of this internal lithological difference: in the northeast sector, more compact and lithoid breccias outcrop with a median Vs value of 1100 m/s. In the central sector, where the lithology shows an increase in the silty matrix, the Vs value decreases to 700 m/s. Finally, the LAB that outcrops in the southwest sector are characterized by low Vs values, with a median value of 500 m/s. Different Vs values in the breccias correspond to different ground deformation behaviors, which cannot be considered negligible for the purpose of correlating deformation and lithology. In fact, higher Vs values correspond to areas with less displacement, while the deformation of PS gradually increases southwestwards, where the cumulative displacement can reach up to -25 - -30 mm. This aspect is confirmed by the calculation of the PCC, which has shown a moderately strong correlation between the Vs of outcropping lithologies and cumulative and vertical displacement.

The observed subsidence are the result of competing compaction phenomena of soil and rocks, at different depths and observation scales.

In figure 19 PSs are grouped into the following cumulative displacement classes, appropriately chosen: uplift; 0 -0.3 mm; -0.3, -1mm; -1, -7 mm; -7, -10mm; < -10 mm. The comparison with Fig. 13 shows a clear overlap: the gray points fall on LAB 3, the orange ones predominantly on LAB 2 and the yellow ones fall in an area delimited partly by a main fault and to the SE by the limit between LAB 1 and LAB 2. Therefore, subsidence values appear to be controlled by the kind of breccia. Only near the NE walls is there a small cluster of points showing subsidence tending towards zero or uplift.
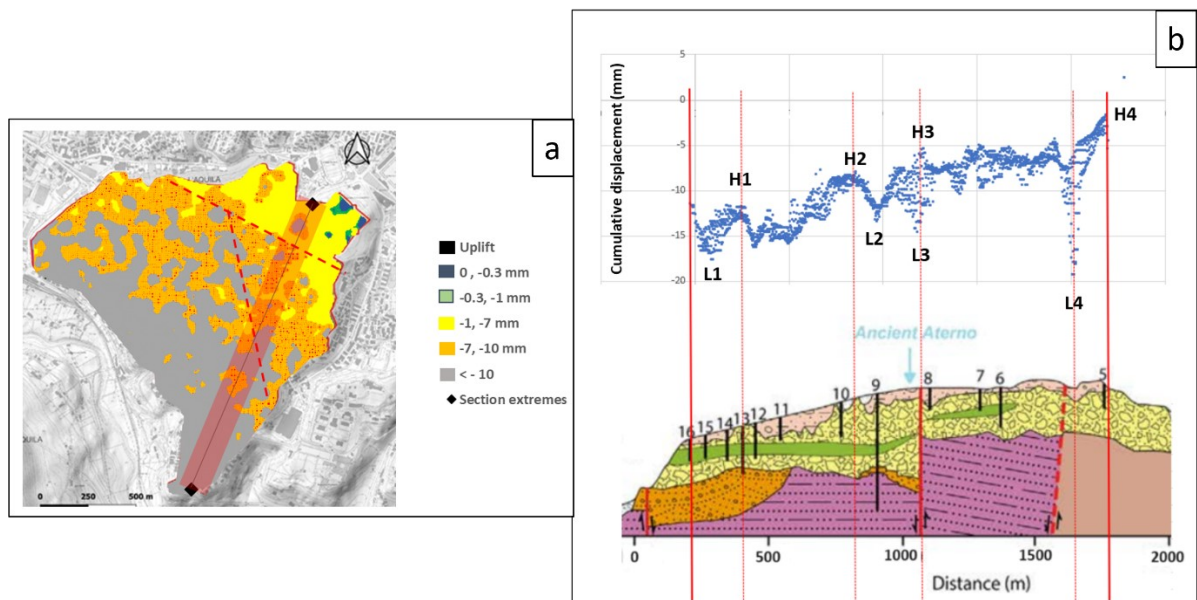
Figure 19: a) PSs grouped in cumulative displacement classes; black line and the associated, 50 m width, semi-transparent red strip is the trace section (panel b); b) the comparison of deformation and subsurface geology is shown through the projection of the cumulative displacement values (mm) of the PSs falling in the red semi-transparent band (in panel a) and the geological section from (Antonielli et al., 2020b).

To achieve a more accurate comparison of displacement data with the subsurface structure, in Fig.19b have been illustrated the values associated with PSs falling in the strip, with a width of 50 m, indicated in semi-transparent red in Fig.19a. This band surrounds an accurate geological section constructed by (Antonielli et al., 2020b), illustrated below, with the same scale. It is highlighted that, although the areal distribution of the lithologies proposed in that article has been determined with greater accuracy in the present work, the geological section proposed by them can be considered reliable, being based on data from several wells well aligned with the section itself. Figs.19a and b (i.e., plan and section) point out that the subsidence decreases going from LAB 3 to LAB 2 and LAB 1. However, the local variations seem to be predominantly controlled by the RS, as the trend of the point cloud in the diagram faithfully follows the thickness of the RS units.

103

Local maxima H1 and H2 occur precisely in areas where the RS is thin or absent. The point cloud minima (i.e., maximum subsidence values) in the interval from L1 to L2 are found where the section displays the greatest RS thicknesses. The local minimum L4 (very high subsidence) is located near the fault, where the section shows an increase in RS depth. This is likely because at the fault, we have both more deformable fault rock and greater erosion, resulting in a deeper RS. The situation with maxima and minima H3 and L3 is a bit more complex. Figure 19A indicates that near the intersection between the geological section and the fault, points with that abscissa falling within the strip exhibit greater subsidence to the right of the section and lower values to the left. Therefore, maximum H3 is associated with the points on the left, whereas L3 corresponds to those on the right side. The geological section (Figure 19b) also shows an increase in RS near the fault. This might be because the fault brought materials with different mechanical properties and erosion susceptibilities into contact, resulting in a more complex situation. What is evident is significant anomalies in displacement values near the two faults. Furthermore, the maxima from H1 to H3, where RS is absent (or significantly thin), follow an increasing trend, likely associated with an increase in LAB thickness in that direction. On the other hand, the maxima in the segment between the two faults show an almost absent trend, with values around -5 mm, consistent with an almost constant LAB thickness. The maximum H4, where subsidence tends towards zero (and transforms into a slight uplift slightly further northeast outside the section), is found where the RS, as well as MDS units, are absent, and LAB 1 directly rests on the carbonate basement uplifted by the fault.

The results illustrated in Figures 19a and b confirm that a significant contribution to the observed subsidence phenomenon is provided by the consolidation of Quaternary units. As hydrogeological behaviour is controlled by lithology (for instance, the abundance of silty-clay matrix influences water filtration), the correlations between InSAR deformation and outcropping lithologies, as well as between InSAR deformation and water table depth, obtained through the calculation of the PCC, represent two sides of the same coin.

In granular soils, seismic shaking produces well-known phenomena of variation in porosity, such as compaction or dilatancy. In the case of saturated fine-grained soils (even above the water table, i.e., in soils saturated by capillarity) a first phase of porosity variation occurs slowly, associated with fluid expulsion (Terzaghi consolidation, Fig. 20), followed by a second phase of secondary consolidation, due to creep phenomena (e.g., (Lancellotta, 2014)). The time evolution of fluid discharge related consolidation in soil and rock depends on both their compressibility and permeability (Guerriero, 2022a; Guerriero & Mazzoli, 2021). In unsaturated soils, the first compaction phase is immediate and is followed by secondary consolidation, which occurs slowly. Note that, as we only have post-seismic data, we cannot detect immediate consolidation effects in unsaturated soils. Therefore, the speed and displacement values of the monitored PS are given by the sum of effects of primary and/or secondary consolidation in saturated soils and the only secondary consolidation of non-saturated ones. Furthermore, large-scale movements of groundwater, involving the fractured carbonates of the basement, contribute to the observed subsidence phenomenon, as assessed by (Marco Moro et al., 2017).

It is known that before a seismic event, the phenomenon of dilatancy occurs at the hanging wall of normal faults (Doglioni et al., 2013; Marco Moro et al., 2017) caused by the opening of fractures and voids that, during the pre-seismic phase, draw groundwater downward, leading to a lowering of water table. Moro et al. (2017) (Marco Moro et al., 2017) conducted a large-scale InSAR analysis that demonstrated that in the months preceding the 2009 earthquake, near to the epicentral area, some of the basins filled with alluvial deposits experienced subsidence phenomena associated with the water table lowering of the Gran Sasso aquifer, to which they are connected. The migration of water from the multi-layer aquifers caused pre-seismic subsidence, while after the earthquake, uplift was recorded in the same areas.

Pore pressure variations can account for the observed fluctuations in the water table, a phenomenon often documented during earthquakes (Doglioni et al., 2013). In fact, during an earthquake, as the hanging wall of a normal fault subsides, interstitial fluids previously accumulated within dilated volumes are expelled. This prior migration of

fluids had led to a gradual increase in pore pressure during the pre-seismic phase. However, with the expulsion of fluids from voids and fractures due to the hanging wall downward movement, pore pressure diminishes, subsequently causing a rise in the water table. The subsequent lowering of the water table to its natural level will occur more rapidly if filtration is favored, and more slowly if water has to pass through lithologies with a low permeability coefficient. The delayed dissipation of pore pressure in the MDS aquitard and LAB 3, low permeability lithologies, can explain the well-recognized negative correlation between subsidence and water table depth in the period following the 2009 earthquake (Figure 20).

Given the highly irregular spatial distribution of the RS, we believe it is indeed the content of silty matrix within LAB 3 (and secondarily within LAB 2) that accounts for the higher subsidence rate within the study area. This lithology, being both characterized by a low S-wave velocity and a low permeability coefficient, explains why the highest ground displacement values are localized in the southern and western areas of the city.
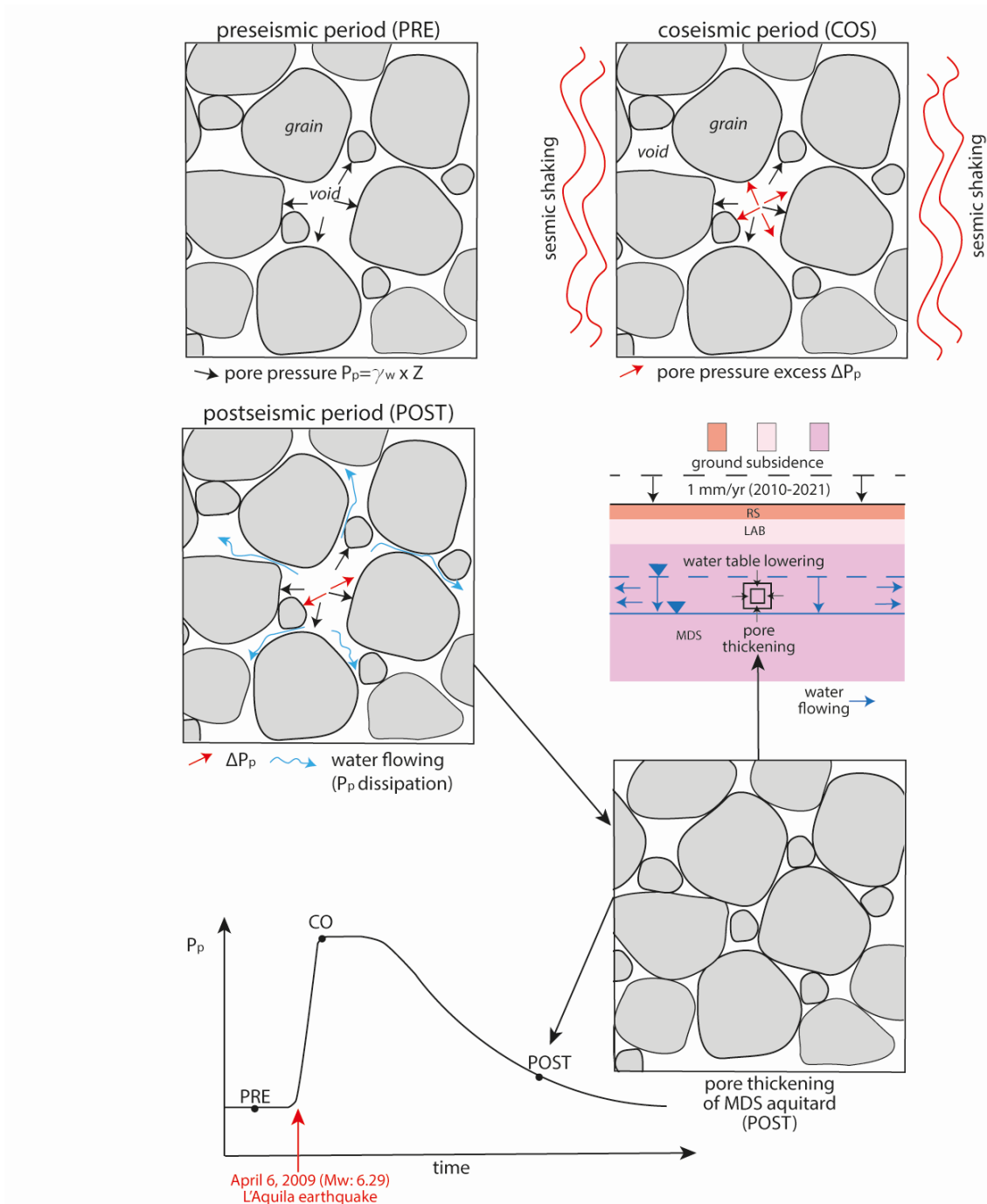
Figure 20: scheme of pore pressure dissipation during the coseismic period of the 6 April 2009 Mw. 6.29 L'Aquila earthquake within above all the low permeability MDS formation and LAB3.

The seasonal cyclicity of precipitation was also taken into account with the goal to assess its potential influence on the monthly variations of InSAR deformations. With this aim, the cross-correlation of the quarterly average precipitation (mm/d) for each month from 2010 to 2021 with the average deformation of all PS resulting from the InSAR analysis using Cosmo-SkyMed descending images during the same period (mm/month), was analysed. In light of the explanations provided regarding interactions between water table oscillation and deformations - where a rise in the piezometric level corresponds to a decrease in the deformation rate – a significant correlation value has been identified, with PCC = 0.560 (i.e., R^2 = 0.313). This highlights a significant connection between the seasonal variations in subsidence on the rainfall rates of the previous months. To verify whether the fluctuations in the groundwater level, resulting from seasonal variations in precipitation, are the only ones responsible for the seasonal variations in the subsidence rate, an analysis carried on via geomechanical modeling would be needed, to quantify variations in effective stress in the subsoil. This kind of analysis is beyond the scope of the present study and will be the subject of future research.

In evaluating the obtained results, it is necessary to remember that reconstructing the outcropping geology in an urban setting is quite difficult, because of building and infrastructure covering, even when a rich database of site investigations is available. Therefore, the correlation value between cumulative displacement and Vs, as well as that with RS thickness, could be different if an even more detailed geological map were available. A 3D geological model of the subsurface would also allow for the assessment of the spatial variability, thickness, and Vs values of the lithologies on which the LAHC buildings are constructed in relation to the deformations detected by Remote Sensing data.

5. Conclusions

Conducting a correlation between satellite and geophysical data represents a novel aspect that sheds light on the potential of interferometry. The satellite records a difference in deformation behavior as the Vs of the outcropping lithology varies. Regarding the LAB, the satellite can even describe internal differences within the lithology, which are well-documented in the literature and supported by a high variability of Vs within this lithology.

The LAB classification based on the amount of silty matrix is the key to comprehending the decade-long deformation phenomena that characterize the historic center. The low permeability coefficient of LAB 3, and LAB 2 introduces a delay in the dissipation of pore pressure within these rock types. Notably, the presence of silty matrix inhibits filtration and retards the decline of the water table. When seismic shaking occurs, the water - previously filling voids and fractures formed at the fault's hanging wall during the pre-seismic phase - is forcefully expelled, causing a sudden rise in the water table. This model of delayed pore pressure dissipation also elucidates the observed correlation between precipitation patterns (which inevitably induce seasonal water table variations) and monthly fluctuations in satellite-detected deformations.

Based on the obtained results and with reference to the insights provided by the study by (Sciortino et al., 2023), it is clear that, it can be stated that the seismic damage to LAHC buildings is strongly influenced by local geological-hydrogeological setting. In fact, greater post-seismic InSAR deformations correspond to more severe damage to buildings, both for 2009 and 1703 earthquake.

Chapter IV – Summary Discussions

The A-DInSAR analysis conducted in this study has allowed the identification of subsidence rates with increasing values from NE to SW of the study area, with velocities reaching and rarely exceeding -5mm/year. From the decomposition of PS velocities into horizontal and vertical components, subsidence is recognized as the main deformation feature in L'Aquila, indicating that the primary component of displacement is vertical. Thanks to the applied approach, a systematic rise in subsidence corresponding to increasing damage classes was discernible for both the 2009 and 1703 earthquakes. The structural damage resulting from both seismic events aligns with areas exhibiting the highest cumulative displacement values between 2010 and 2021. Satellite data illustrates that the most severely affected structures (D3, D4, D5 - for the 2009 earthquake, and Destroyed and Damaged buildings for the 1703 earthquake) are situated in zones experiencing the most pronounced deformation.

In the case of the 2009 earthquake, a gradual escalation in cumulative displacement, averaging -1 mm for each damage class from DG1 to DG4, was noted. Specifically, only the average velocity values related to classes DG4 and DG5 showed overlapping confidence intervals, suggesting that the observed differences lack statistical significance. In a similar vein, even though the urban sprawl in 1703 was considerably more limited than today, with areas like the southern sector of the city undergoing urbanization only in the past 80 years (A. Tertulliani et al., 2012), the findings revealed that the zones surrounding buildings destroyed by the 1703 earthquake exhibited higher levels of deformation captured by Cosmo-SkyMed over the last decade. This stands in contrast to regions where structures had experienced only minor damage. Furthermore, there was a distinct reduction in deformation observed in areas that had remained undamaged during the 1703 event. Since the intensity of damage can be interpreted as an indicator of the intensity of local seismic strain intensity, the increase in subsidence rate can be attributed to a rise in seismic shacking. Due to the substantial differences in the urban layout between the two events, it became evident that the distribution of damage within L'Aquila's historic center is more influenced by geological factors more than by inherent building characteristics. To confirm this hypothesis, the initial phase of the research meticulously evaluated whether A-DInSAR deformations could be

influenced by buildings and post-2009 earthquake maintenance and reconstruction efforts. The findings revealed no disparities in velocities between PS located on buildings and those on the ground. Furthermore, the vulnerability map of buildings did not correlate with the observed seismic damage. The cluster analysis revealed consistent deformation trends in the subsidence curve shapes of both reconstructed and unreconstructed buildings, regardless of their damage classification. This signifies that the progression of deformation behavior is not linked to the structural settling subsequent to refurbishment or reconstruction.

In light of these considerations, the A-DInSAR maps derived from Cosmo-SkyMed descending and Sentinel-1 ascending images have become the key tool to understand the geological-hydrogeological conditions driving the distribution of damage. Many studies suggest that the differences in seismic amplification observed in L'Aquila historic center during the 2009 and 1703 earthquakes could be associated with the significant variation in the characteristics of continental sediments filling the Plio-Quaternary graben upon which the city was built (Amoroso et al., 2018; Del Monaco et al., 2013; Durante et al., 2017; Mannella et al., 2019; Martelli et al., 2012; Nocentini et al., 2017a; Tallini et al., 2020). The geostatistical analysis confirms this theory, as the data reveal widespread subsidence within the investigated area with similar deformation trends even for distant points, while also displaying scattered values for neighboring points. The correlation analysis has demonstrated that ground deformations (and therefore damage) are more significant in areas where the Vs (shear wave velocity) of the outcropping lithologies is low (PCC is 0.46 for vertical displacement and 0.47 for cumulative displacement) and where the water table is shallower (PCC is -0.52 for vertical displacement and -0.39 for cumulative displacement).

The detailed geological characterization of the study area and the collection of Vs data highlighted that the factor driving the increase in subsidence from NE to SW of the historic center is the transition from LAB 1 to LAB 3, marked by an increase in the silty matrix at the expense of the clast percentage. The variability of Vs values within the L'Aquila breccias is extremely significant: in the northeast sector, median Vs value is 1100 m/s; in the central sector, the Vs value decreases to 700 m/s; southwest sector are

characterized by low Vs values, with a median of 500 m/s. Different Vs values in the breccias correspond to different ground deformation behaviors, which cannot be considered negligible for the purpose of correlating deformation and lithology. In fact, higher Vs values correspond to areas with less displacement, while the deformation of PS gradually increases southwestwards, where the cumulative displacement can reach up to -25 - -30 mm. Second-order variations in subsidence appear to be controlled by the thickness of the Red Soils formation, where an increase correlates with higher rates of subsidence. The findings indicate that a significant contribution to the observed subsidence phenomenon stems from the consolidation of Quaternary deposits. The correlation identified between InSAR deformations and the depth of the regional aquifer further confirms this. In fact, hydrogeological behaviour is controlled by lithology (for instance, the abundance of silty-clay matrix influences water filtration). In granular soils, seismic shaking produces well-known phenomena of variation in porosity, such as compaction or dilatancy. In the case of saturated fine-grained soils (even above the water table, i.e., in soils saturated by capillarity) a first phase of porosity variation occurs slowly, associated with fluid expulsion, followed by a second phase of secondary consolidation, due to creep phenomena (e.g., (Lancellotta, 2014)). The temporal progression of fluid discharge-driven consolidation in soil and rock relies on their compressibility and permeability (Guerriero, 2022b; Guerriero & Mazzoli, 2021). In unsaturated soils, initial compaction happens promptly, succeeded by a gradual secondary consolidation. It's important to highlight that this thesis solely examines post-seismic A-DInSAR data, thereby unable to discern immediate consolidation effects in unsaturated soils. Therefore, the speed and displacement values of the monitored PS are given by the sum of effects of primary and/or secondary consolidation in saturated soils and the only secondary consolidation of non-saturated ones. The slow release of pore pressure in the MDS aquitard, LAB 3, LAB 2 and RS lithology, characterized by low permeability, provides a plausible explanation for the widely observed inverse relationship between subsidence and water table depth during the post-2009 earthquake period.

This model of delayed pore pressure dissipation also elucidates the observed correlation between precipitation patterns (which inevitably induce seasonal water table variations)

and monthly fluctuations in satellite-detected deformations. In light of the explanations provided regarding interactions between water table oscillation and deformations - where a rise in the piezometric level corresponds to a decrease in the deformation rate – a significant correlation value has been identified, with PCC = 0.560 (i.e., $R2 = 0.313$). This highlights a significant link between seasonal variations in subsidence and rainfall rates in the preceding months. To ascertain whether fluctuations in the water table level, resulting from seasonal precipitation changes, solely account for the seasonal variations in subsidence rates, an analysis via geomechanical modeling would be necessary. This analysis aims to quantify variations in effective stresses in the subsurface. However, this type of analysis falls beyond the scope of the current study and could be a subject for future research.

Chapter V – Final Remarks

The integrated use of remote sensing data and ground-based information in studying the deformation processes within the historic center of L'Aquila enabled an in-depth analysis of seismic damage distribution and its influencing factors. The methodology employed facilitated an understanding that damage distribution is influenced by the geological and hydrogeological characteristics of the soil beneath the buildings foundations.

The study revealed that the A-DInSAR maps, depicting post-seismic deformations from 2010 to 2021, accurately represent the distribution of damage caused by both the 2009 and 1703 earthquakes. The precision achieved in interferometric data, utilizing a long time series of images, enabled the detection of a gradual increase in subsidence corresponding to the severity of damage. The extensive subsidence identified within the study area exhibits ascending values from the NE to SW sectors of the city, reflecting the significant spatial variability of continental deposits within L'Aquila's historic center. Additionally, geostatistical analysis unveiled a lack of spatial correlation among the velocities of the monitored PS.

Since deformation identified by Cosmo-SkyMed between 2010 and 2021 appears as not solely matching with 2009 seismic event effects but, rather, as characterizing risk features of the studied area in general, the findings of this PhD thesis pave the way for a new utilization of long-term time series of satellite SAR data in high-risk seismic areas, as a powerful tool aimed at mapping most vulnerable regions and effectively mitigating seismic risks. This would be a relevant goal, as this methodology allows large areas to be monitored at low cost and enables the estimation of ground displacement where traditional tools for measuring soil movement may prove inadequate for characterizing the heterogeneity of deformations at urban scale. In this regard, in view of future research, this method may benefit from validation based on pre-seismic data (when they will be available)

Conducting a correlation between satellite and geophysical data represents a novel aspect that sheds light on the potential of interferometry. The satellite records a difference in deformation behaviour as the Vs of the outcropping lithology varies.

Regarding the LAB, the satellite can even describe internal differences within the lithology, which are well-documented in the literature and supported by a high variability of Vs within this lithology. The LAB classification based on the amount of silty matrix is the key to comprehending the decade-long deformation phenomena that characterize the historic center. The low permeability coefficient of LAB 3, and LAB 2 introduces a delay in the dissipation of pore pressure within these rock types. Notably, the presence of silty matrix inhibits filtration and retards the decline of the water table. When seismic shaking occurs, the water - previously filling voids and fractures formed at the fault's hanging wall during the pre-seismic phase - is forcefully expelled, causing a sudden rise in the water table. This model of delayed pore pressure dissipation also elucidates the observed correlation between precipitation patterns (which inevitably induce seasonal water table variations) and monthly fluctuations in satellite-detected deformations.

References

(ASI), A. S. I. (2021). *COSMO-SkyMed Seconda Generazione: System and Product Description*. chrome-extension://efaidnbmnnnibpcajpcglclefindmkaj/https://earth.esa.int/eogateway/documents/20142/37627/COSMO-SkyMed-Second-Generation-Mission-Products-Description.pdf

Agostini, S., Palombo, M. R., Rossi, M. A., Di Canzio, E., & Tallini, M. (2012). Mammuthus meridionalis (Nesti, 1825) from Campo di Pile (L'Aquila, Abruzzo, Central Italy). *Quaternary International*, *276–277*, 42–52. https://doi.org/10.1016/j.quaint.2012.05.013

Amanti, M., Muraro, C., Roma, M., Chiessi, V., Puzzilli, L. M., Catalano, S., Romagnoli, G., Tortorici, G., Cavuoto, G., Albarello, D., Fantozzi, P. L., Paolucci, E., Pieruccini, P., Caprari, P., Mirabella, F., Della Seta, M., Esposito, C., Di Curzio, D., Francescone, M., … Tallini, M. (2020). Geological and geotechnical models definition for 3rd level seismic microzonation studies in Central Italy. In *Bulletin of Earthquake Engineering* (Vol. 18, Issue 12). Springer Netherlands. https://doi.org/10.1007/s10518-020-00843-x

Ameri, G., Massa, M., Bindi, D., D'Alema, E., Gorini, A., Luzi, L., Marzorati, S., Pacor, F., Paolucci, R., Puglia, R. & Smerzini, C. (2009). (2009). The 6 april 2009, Mw 6.3, L'Aquila (Central Italy) earthquake: strong-motion observations. *Seismological Research Letters*.

Amoroso, S., Gaudiosi, I., Tallini, M., Di Giulio, G., & Milana, G. (2018). 2D site response analysis of a cultural heritage: the case study of the site of Santa Maria di Collemaggio Basilica (L'Aquila, Italy). *Bulletin of Earthquake Engineering*, *16*(10), 4443–4466. https://doi.org/10.1007/s10518-018-0356-2

Amoruso, A., & Crescentini, L. (2009). Slow diffusive fault slip propagation following the 6 April 2009 L'Aquila earthquake, Italy. *Geophysical Research Letters*, *36*(24), 1–5. https://doi.org/10.1029/2009GL041503

Antinori, A. L. (1971). *Annali Degli Abruzzi Dalle Origini All'anno 1777* (A. F. E. S. Bolognese (ed.); edizione i).

Antonielli, B., Della Seta, M., Esposito, C., Scarascia Mugnozza, G., Schilirò, L., Spadi, M., & Tallini, M. (2020a). Quaternary rock avalanches in the Apennines: New data and interpretation of the huge clastic deposit of the L'Aquila Basin (central Italy). *Geomorphology*, *361*. https://doi.org/10.1016/j.geomorph.2020.107194

Antonielli, B., Della Seta, M., Esposito, C., Scarascia Mugnozza, G., Schilirò, L., Spadi, M., & Tallini, M. (2020b). Quaternary rock avalanches in the Apennines: New data and interpretation of the huge clastic deposit of the L'Aquila Basin (central Italy). *Geomorphology*, *361*. https://doi.org/10.1016/j.geomorph.2020.107194

Antonielli, B., Mazzanti, P., Rocca, A., Bozzano, F., & Cas, L. D. (2019). A-DInSAR performance for updating landslide inventory in mountain areas: An example from lombardy region (Italy). *Geosciences (Switzerland)*, *9*(9). https://doi.org/10.3390/geosciences9090364

Antonielli, B., Sciortino, A., Scancella, S., Bozzano, F., & Mazzanti, P. (2021). Tracking deformation processes at the legnica glogow copper district (Poland) by satellite insar—i: Room and pillar mine district. *Land*, *10*(6). https://doi.org/10.3390/land10060653

Anzidei, M., Boschi, E., Cannelli, V., Devoti, R., Esposito, A., Galvani, A., Melini, D., Pietrantonio, G., Riguzzi, F., Sepe, V., & Serpelloni, E. (2009). Coseismic deformation of the destructive April 6, 2009 L'Aquila earthquake (central Italy) from GPS data. *Geophysical Research Letters*, *36*(17), 3–7. https://doi.org/10.1029/2009GL039145

Atzori, S., Hunstad, I., Chini, M., Salvi, S., Tolomei, C., Bignami, C., Stramondo, S., Trasatti, E., Antonioli, A., & Boschi, E. (2009). Finite fault inversion of DInSAR coseismic displacement of the 2009 L'Aquila earthquake (central Italy). *Geophysical Research Letters*, *36*(15), 1–6. https://doi.org/10.1029/2009GL039293

Berardino, P., Fornaro, G., Lanari, R., & Sansosti, E. (2002). A new algorithm for surface deformation monitoring based on small baseline differential SAR interferograms. *IEEE Transactions on Geoscience and Remote Sensing*, *40*(11), 2375–2383. https://doi.org/10.1109/TGRS.2002.803792

Bishop, C. M. (2006). Pattern recognition and Machine Learning. In Springer (Ed.), *Pattern recognition and Machine Learning*. http://www.atsjournals.org/doi/abs/10.1164/ajrccm-conference.2013.187.1_MeetingAbstracts.A4272

Boncio, P., Lavecchia, G., & Pace, B. (2004). Defining a model of 3D seismogenic sources for Seismic Hazard Assessment applications: The case of central Apennines (Italy). *Journal of Seismology*, *8*(3), 407–425. https://doi.org/10.1023/B:JOSE.0000038449.78801.05

Bordoni, M., Bonì, R., Colombo, A., Lanteri, L., & Meisina, C. (2018). A methodology for ground motion area detection (GMA-D) using A-DInSAR time series in landslide investigations. *Catena*, *163*(November 2017), 89–110. https://doi.org/10.1016/j.catena.2017.12.013

Bozzano, F., Ciampi, P., Monte, D., Innocca, F., Luberti, G. M., Mazzanti, P., Rivellino, S., Rompato, M., Scancella, S., & Scarascia Mugnozza, G. (n.d.). *SATELLITE A-DINSAR MONITORING OF THE VITTORIANO MONUMENT (ROME, ITALY): IMPLICATIONS FOR HERITAGE PRESERVATION EXTENDED ABSTRACT*. https://doi.org/10.4408/IJEGE.2020-02.O-01

Bozzano, F., Esposito, C., Mazzanti, P., Patti, M., & Scancella, S. (2018). Imaging multi-age construction settlement behaviour by advanced SAR interferometry. *Remote Sensing*, *10*(7). https://doi.org/10.3390/rs10071137

Bru, G., González, P. J., Mateos, R. M., Roldán, F. J., Herrera, G., Béjar-Pizarro, M., & Fernández, J. (2017). A-DInSAR monitoring of landslide and subsidence activity: A case of urban damage in Arcos de la Frontera, Spain. *Remote Sensing*, *9*(8), 1–17. https://doi.org/10.3390/rs9080787

Capes, R., & Teeuw, R. (2017). On safe ground? Analysis of European urban geohazards using satellite radar interferometry. *International Journal of Applied Earth Observation and Geoinformation*, *58*, 74–85. https://doi.org/10.1016/j.jag.2017.01.010

Cavinato, G. P., Carusi, C., Dall'asta, M., Miccadei, E., & Piacentini, T. (2002). Sedimentary and tectonic evolution of Plio-Pleistocene alluvial and lacustrine deposits of Fucino Basin (central Italy). *Sedimentary Geology*, *148*(1–2), 29–59. https://doi.org/10.1016/S0037-0738(01)00209-3

Chiarabba, C., Amato, A., Anselmi, M., Baccheschi, P., Bianchi, I., Cattaneo, M., Cecere, G., Chiaraluce, L., Ciaccio, M. G., De Gori, P., De Luca, G., Di Bona, M., Di Stefano, R., Faenza, L., Govoni, A., Improta, L., Lucente, F. P., Marchetti, A., Margheriti, L., … Valoroso, L. (2009). The 2009 L'Aquila (central Italy) Mw6.3 earthquake: main shock and aftershocks. *Geophysical Research Letters*, *36*(18), 1–6. https://doi.org/10.1029/2009GL039627

Ciampalini, A., Bardi, F., Bianchini, S., Frodella, W., del Ventisette, C., Moretti, S., & Casagli, N. (2014). Analysis of building deformation in landslide area using multisensor PSInSARTM technique. *International Journal of Applied Earth Observation and Geoinformation*, *33*(1), 166–180. https://doi.org/10.1016/j.jag.2014.05.011

Cigna, F., Del Ventisette, C., Liguori, V., & Casagli, N. (2011). Advanced radar-interpretation of InSAR time series for mapping and characterization of geological processes. *Natural Hazards and Earth System Science*, *11*(3), 865–881. https://doi.org/10.5194/nhess-11-865-2011

Colapietra, R. (1978). *L'Aquila dell'Antinori strutture sociali ed urbane della citta'nel sei e settecento. Nella Sede della Deputazione.*

Comerci, V., Vittori, E., Cipolloni, C., Di Manna, P., Guerrieri, L., Nisio, S., Succhiarelli, C., Ciuffreda, M., & Bertoletti, E. (2015). Geohazards Monitoring in Roma from InSAR and In Situ Data: Outcomes of the PanGeo Project. *Pure and*

Applied Geophysics, *172*(11), 2997–3028. https://doi.org/10.1007/s00024-015-1066-1

Cosentino, D., Asti, R., Nocentini, M., Gliozzi, E., Kotsakis, T., Mattei, M., Esu, D., Spadi, M., Tallini, M., Cifelli, F., Pennacchioni, M., Cavuoto, G., & Di Fiore, V. (2017). New insights into the onset and evolution of the central Apennine extensional intermontane basins based on the tectonically active L'Aquila Basin (central Italy). *Bulletin of the Geological Society of America*, *129*(9–10), 1314–1336. https://doi.org/10.1130/B31679.1

Cosentino, D., Cipollari, P., Marsili, P., & Scrocca, D. (2010). Geology of the central Apennines: A regional review. *Journal of the Virtual Explorer*, *36*. https://doi.org/10.3809/jvirtex.2009.00223

Del Monaco, F., Tallini, M., De Rose, C., & Durante, F. (2013). HVNSR survey in historical downtown L'Aquila (central Italy): Site resonance properties vs. subsoil model. *Engineering Geology*, *158*, 34–47. https://doi.org/10.1016/j.enggeo.2013.03.008

Del Soldato, M., Di Martire, D., Bianchini, S., Tomás, R., De Vita, P., Ramondini, M., Casagli, N., & Calcaterra, D. (2019). Assessment of landslide-induced damage to structures: the Agnone landslide case study (southern Italy). *Bulletin of Engineering Geology and the Environment*, *78*(4), 2387–2408. https://doi.org/10.1007/s10064-018-1303-9

di Giulio, G., Gaudiosi, I., Cara, F., Milana, G., & Tallini, M. (2014). Shear-wave velocity profile and seismic input derived from ambient vibration array measurements: The case study of downtown L'Aquila. *Geophysical Journal International*, *198*(2), 848–866. https://doi.org/10.1093/gji/ggu162

Di Traglia, F., De Luca, C., Manzo, M., Nolesini, T., Casagli, N., Lanari, R., & Casu, F. (2021). Joint exploitation of space-borne and ground-based multitemporal InSAR measurements for volcano monitoring: The Stromboli volcano case study. *Remote Sensing of Environment*, *260*(March), 112441.

https://doi.org/10.1016/j.rse.2021.112441

Diggle, P. J. and Ribeiro, P. J. (2007). Front matter. In Springer - Verlag (Ed.), *Model-based geostatistics*. https://doi.org/10.1007/978-0-387-48536-2

Doglioni, C., Barba, S., Carminati, E., & Riguzzi, F. (2013). Geoscience Frontiers Fault on e off versus coseismic fl uids reaction. *Geoscience Frontiers*, *5*, 1–14. http://dx.doi.org/10.1016/j.gsf.2013.08.004

Durante, F., Di Giulio, G., Tallini, M., Milana, G., & Macerola, L. (2017). A multidisciplinary approach to the seismic characterization of a mountain top (Monteluco, central Italy). *Physics and Chemistry of the Earth*, *98*, 119–135. https://doi.org/10.1016/j.pce.2016.10.015

Ertel, W. (2011). *Introduction to Artificial Intelligence* (Springer (ed.)).

Ezquerro, P., Del Soldato, M., Solari, L., Tomás, R., Raspini, F., Ceccatelli, M., Fernández-Merodo, J. A., Casagli, N., & Herrera, G. (2020). Vulnerability assessment of buildings due to land subsidence using insar data in the ancient historical city of pistoia (Italy). *Sensors (Switzerland)*, *20*(10), 1–23. https://doi.org/10.3390/s20102749

Ferlisi, S., Nicodemo, G., Peduto, D. Negulescu, C., & Grandjean, G. (2020). Deterministic and probabilistic analyses of the 3D response of masonry buildings to imposed settlement troughs. *Georisk: Assessment and Management of Risk for Engineered Systems and Geohazards*, *14*(4), 260–279. https://doi.org/10.1080/17499518.2019.1658880

Ferretti, A., Rucci, A., Tamburini, A., Del Conte, S., & Cespa, S. (2014). Advanced InSAR for reservoir geomechanical analysis. *EAGE Workshop on Geomechanics in the Oil and Gas Industry*, *May*, 73–77. https://doi.org/10.3997/2214-4609.20140459

Ferretti, Alessandro, Prati, C., & Rocca, F. (2001). Permanent scatterers in SAR interferometry. *IEEE Transactions on Geoscience and Remote Sensing*, *39*(1), 8–

20. https://doi.org/10.1109/36.898661

Francesco, Guglielmino; Giuseppe, Nunnari; Giuseppe, Puglisi; Spata, A. (n.d.). Simultaneous and Integrated Strain Tensor Estimation From Geodetic and Satellite Deformation Measurements to Obtain Three-Dimensional Displacement Maps. *IEEE Transactions on Geoscience and Remote Sensing*, *49*, 1815–1826. https://doi.org/10.1109/TGRS.2010.2103078

Galadini, F., Galli, P., & Moro, M. (2003). Paleoseismology of silent faults in the Central Apennines (Italy): The Campo Imperatore Fault (Gran Sasso Range Fault System). *Annals of Geophysics*, *46*(5), 793–814.

Galli, P., Galadini, F., Moro, M., & Giraudi, C. (2002). New paleoseismological data from the Gran Sasso d'Italia area (central Apennines). *Geophysical Research Letters*, *29*(7), 38-1-38–4. https://doi.org/10.1029/2001GL013292

Galli, Paolo, Giaccio, B., & Messina, P. (2010). The 2009 central Italy earthquake seen through 0.5 Myr-long tectonic history of the L'Aquila faults system. *Quaternary Science Reviews*, *29*(27–28), 3768–3789. https://doi.org/10.1016/j.quascirev.2010.08.018

Giaccio, B., Galli, P., Messina, P., Peronace, E., Scardia, G., Sottili, G., Sposato, A., Chiarini, E., Jicha, B., & Silvestri, S. (2012). Fault and basin depocentre migration over the last 2 Ma in the L'Aquila 2009 earthquake region, central Italian Apennines. *Quaternary Science Reviews*, *56*, 69–88. https://doi.org/10.1016/j.quascirev.2012.08.016

Gruppo di lavoro CPTI. (2004). *Catalogo Parametrico dei Terremoti Italiani, versione 2004 (CPTI04), INGV, Bologna. http://emidius.mi.ingv.it/CPTI04/*. http://www.arpa.emr.it/cms3/documenti/moniter/quaderni/06_Epidemiologia_Mon iter.pdf#page=75

Guerriero, V. (2022a). 1923–2023: One Century since Formulation of the Effective Stress Principle, the Consolidation Theory and Fluid–Porous-Solid Interaction Models. *Geotechnics*. https://doi.org/https://doi.org/10.3390/geotechnics2040045

Guerriero, V. (2022b). 1923–2023: One Century since Formulation of the Effective Stress Principle, the Consolidation Theory and Fluid–Porous-Solid Interaction Models. *Geotechnics*, *2*(4), 961–988. https://doi.org/10.3390/geotechnics2040045

Guerriero, V., & Mazzoli, S. (2021). Theory of effective stress in soil and rock and implications for fracturing processes: A review. *Geosciences (Switzerland)*, *11*(3), 1–35. https://doi.org/10.3390/geosciences11030119

Guglielmino, F., Bignami, C., Bonforte, A., Briole, P., Obrizzo, F., Puglisi, G., ... & Wegmüller, U. (n.d.). Analysis of satellite and in situ ground deformation data integrated by the SISTEM approach: The April 3, 2010 earthquake along the Pernicana fault (Mt. Etna-Italy) case study. *Arth and Planetary Science Letters*.

Hanssen, R. F. (2001). SAR interferometry. In *Novel Radar Techniques and Applications*. https://doi.org/10.1049/SBRA512F_ch6

Herrera, G., Álvarez Fernández, M. I., Tomás, R., González-Nicieza, C., López-Sánchez, J. M., & Álvarez Vigil, A. E. (2012). Forensic analysis of buildings affected by mining subsidence based on Differential Interferometry (Part III). *Engineering Failure Analysis*, *24*(May 1998), 67–76. https://doi.org/10.1016/j.engfailanal.2012.03.003

Institute, G. S. S. (n.d.). *Open Data Ricostruzione – Interventi*.

Kampes, B. M. (2006). Radar interferometry: Persistent scatterer technique. In *Radar Interferometry: Persistent Scatterer Technique* (Vol. 12). https://doi.org/10.1007/978-1-4020-4723-7

Lanari, R., Berardino, P., Bonano, M., Casu, F., Manconi, A., Manunta, M., Manzo, M., Pepe, A., Pepe, S., Sansosti, E., Solaro, G., Tizzani, P., & Zeni, G. (2010). Surface displacements associated with the L'Aquila 2009 Mw 6.3 earthquake (central Italy): New evidence from SBAS-DInSAR time series analysis. *Geophysical Research Letters*, *37*(20), 10–15. https://doi.org/10.1029/2010GL044780

Lancellotta, R. (2014). *Geotechnical Engineering*. Taylor & Francis.

https://doi.org/https://doi.org/10.1201/9781482265934

Lanzo, G., Tallini, M., Milana, G., Di Capua, G., Del Monaco, F., Pagliaroli, A., & Peppoloni, S. (2011). The Aterno valley strong-motion array: Seismic characterization and determination of subsoil model. *Bulletin of Earthquake Engineering*, *9*(6), 1855–1875. https://doi.org/10.1007/s10518-011-9301-3

Locati, M., Camassi, R., Rovida, A., Ercolani, E., Bernardini, F., Castelli, V., Caracciolo, C. H., Tertulliani, A., Rossi, A., Azzaro, R., Amico, S. D., Antonucci, A., Locati, M., Rovida, A., Antonucci, A., Amico, S. D., Albini, P., Bianchi, M. G., Ciuccarelli, C., … Accordo, A. (2021). *Database Macrosismico Italiano*.

Macerola, L., Tallini, M., Giulio, G. Di, Nocentini, M., & Milana, G. (2019). The 1-D and 2-D seismic modeling of deep quaternary basin (downtown L'Aquila, central Italy). *Earthquake Spectra*, *35*(4), 1689–1710. https://doi.org/10.1193/062618EQS166M

Magaldi, D., & Tallini, M. (2000). A micromorphological index of soil development for the Quaternary geology research. *Catena*, *41*(4), 261–276. https://doi.org/10.1016/S0341-8162(00)00096-5

Mair, R. J., Taylor, R. N., & Burland, J. B. (1996). Prediction of ground movements and assessment of risk of building damage due to bored tunnelling. *Geotechnical Aspects of Underground Construction in Soft Ground*, *August*, 713–718.

Mancini, M., Cavuoto, G., Pandolfi, L., Petronio, C., Salari, L., & Sardella, R. (2012). Coupling basin infill history and mammal biochronology in a Pleistocene intramontane basin: The case of western L'Aquila Basin (central Apennines, Italy). *Quaternary International*, *267*, 62–77. https://doi.org/10.1016/j.quaint.2011.03.020

Mannella, A., Macerola, L., Martinelli, A., Sabino, A., & Tallini, M. (2019). The local seismic response and the effects of the 2016 central Italy earthquake on the buildings of L'aquila downtown. *Bollettino Di Geofisica Teorica Ed Applicata*, *60*(2), 263–276. https://doi.org/10.4430/bgta0241

Mantovani, M., Bossi, G., Marcato, G., Schenato, L., Tedesco, G., Titti, G., & Pasuto, A. (2019). New perspectives in landslide displacement detection using Sentinel-1 datasets. *Remote Sensing*, *11*(18). https://doi.org/10.3390/rs11182135

Martelli, L., Boncio, P., Baglione, M., Cavuoto, G., Mancini, M., Mugnozza, G. S., & Tallini, M. (2012). Main geologic factors controlling site response during the 2009 L'Aquila earthquake. *Italian Journal of Geosciences*, *131*(3), 423–439. https://doi.org/10.3301/IJG.2012.12

Martino, S., Fiorucci, M., Marmoni, G. M., Casaburi, L., Antonielli, B., & Mazzanti, P. (2022). Increase in landslide activity after a low-magnitude earthquake as inferred from DInSAR interferometry. *Scientific Reports*, *12*(1), 1–19. https://doi.org/10.1038/s41598-022-06508-w

Mazzanti, P., Antonielli, B., Sciortino, A., Scancella, S., & Bozzano, F. (2021). Tracking deformation processes at the legnica glogow copper district (Poland) by satellite insar—ii: Żelazny most tailings dam. *Land*, *10*(6). https://doi.org/10.3390/land10060654

Moro, M., Gori, S., Falcucci, E., Saroli, M., Galadini, F., & Salvi, S. (2013). Historical earthquakes and variable kinematic behaviour of the 2009 L'Aquila seismic event (central Italy) causative fault, revealed by paleoseismological investigations. *Tectonophysics*, *583*, 131–144. https://doi.org/10.1016/j.tecto.2012.10.036

Moro, Marco, Saroli, M., Stramondo, S., Bignami, C., Albano, M., Falcucci, E., Gori, S., Doglioni, C., Polcari, M., Tallini, M., Macerola, L., Novali, F., Costantini, M., Malvarosa, F., & Wegmüller, U. (2017). New insights into earthquake precursors from InSAR. *Scientific Reports*, *7*(1), 1–11. https://doi.org/10.1038/s41598-017-12058-3

Nappo, N., Ferrario, M. F., Livio, F., & Michetti, A. M. (2020). Regression analysis of subsidence in the como basin (northern Italy): New insights on natural and anthropic drivers from InSAR data. *Remote Sensing*, *12*(18). https://doi.org/10.3390/RS12182931

Nappo, N., Peduto, D., Polcari, M., Livio, F., Ferrario, M. F., Comerci, V., Stramondo, S., & Michetti, A. M. (2021). Subsidence in Como historic centre (northern Italy): Assessment of building vulnerability combining hydrogeological and stratigraphic features, Cosmo-SkyMed InSAR and damage data. *International Journal of Disaster Risk Reduction*, *56*. https://doi.org/10.1016/j.ijdrr.2021.102115

NASA. (n.d.). *POWER Data Access Viewer*. 2023-11-23

NHAZCA. (n.d.). *PS Toolbox*. Retrieved November 23, 2023, from https://www.sarinterferometry.com/ps-toolbox/

Nocentini, M., Asti, R., Cosentino, D., Durantec, F., Gliozzi, E., Macerola, L., & Tallini, M. (2017a). Plio-quaternary geology of L'Aquila-Scoppito basin (Central Italy). *Journal of Maps*, *13*(2), 563–574. https://doi.org/10.1080/17445647.2017.1340910

Nocentini, M., Asti, R., Cosentino, D., Durantec, F., Gliozzi, E., Macerola, L., & Tallini, M. (2017b). Plio-quaternary geology of L'Aquila-Scoppito basin (Central Italy). *Journal of Maps*, *13*(2), 563–574. https://doi.org/10.1080/17445647.2017.1340910

Nocentini, M., Cosentino, D., Spadi, M., & Tallini, M. (2018). Plio-quaternary geology of the paganica-san demetrio-castelnuovo basin (Central italy). *Journal of Maps*, *14*(2), 411–420. https://doi.org/10.1080/17445647.2018.1481774

Pagliaroli, A., Pergalani, F., Ciancimino, A., Chiaradonna, A., Compagnoni, M., de Silva, F., Foti, S., Giallini, S., Lanzo, G., Lombardi, F., Luzi, L., Macerola, L., Nocentini, M., Pizzi, A., Tallini, M., & Teramo, C. (2020). Site response analyses for complex geological and morphological conditions: relevant case-histories from 3rd level seismic microzonation in Central Italy. In *Bulletin of Earthquake Engineering* (Vol. 18, Issue 12). https://doi.org/10.1007/s10518-019-00610-7

Peduto, D., Ferlisi, S., Nicodemo, G., Reale, D., Pisciotta, G., & Gullà, G. (2017). Empirical fragility and vulnerability curves for buildings exposed to slow-moving landslides at medium and large scales. *Landslides*, *14*(6), 1993–2007.

https://doi.org/10.1007/s10346-017-0826-7

Peduto, D., Nicodemo, G., Maccabiani, J., & Ferlisi, S. (2017). Multi-scale analysis of settlement-induced building damage using damage surveys and DInSAR data: A case study in The Netherlands. *Engineering Geology*, *218*, 117–133. https://doi.org/10.1016/j.enggeo.2016.12.018

Perissin, D., Wang, Z., & Wang, T. (2011). The SARPROZ InSAR tool for urban subsidence/manmade structure stability monitoring in China. *34th International Symposium on Remote Sensing of Environment - The GEOSS Era: Towards Operational Environmental Monitoring*.

Petitta, M., & Tallini, M. (2003). Groundwater Resources and Human Impacts in a Quaternary Intramontane Basin (L'Aquila Plain, Central Italy). *Water International*, *28*(1), 57–69. https://doi.org/10.1080/02508060308691665

Rovida, A., Locati, M., Camassi, R., Lolli, B., & Gasperini, P. (2020). The Italian earthquake catalogue CPTI15. In *Bulletin of Earthquake Engineering* (Vol. 18, Issue 7). Springer Netherlands. https://doi.org/10.1007/s10518-020-00818-y

Sciortino, A., Marini, R., Guerriero, V., Mazzanti, P., & Tallini, M. (2023). *Satellite A-DInSAR pattern recognition for seismic vulnerability mapping at city scale : insights from the L ' Aquila (Italy) case study*. 1–60. https://doi.org/10.1080/15481603.2023.2293522

SKEMPTON, A. W., & MACDONALD, D. H. (1956). THE ALLOWABLE SETTLEMENTS OF BUILDINGS. *Proceedings of the Institution of Civil Engineers*, *5*(6), 727–768. https://doi.org/10.1680/ipeds.1956.12202

Spadi, M., Gliozzi, E., Cosentino, D., & Nocentini, M. (2016). Late Piacenzian–Gelasian freshwater ostracods (Crustacea) from the L'Aquila Basin (central Apennines, Italy). *Journal of Systematic Palaeontology*, *14*(7), 617–642. https://doi.org/10.1080/14772019.2015.1079561

Storti, F., Aldega, L., Balsamo, F., Corrado, S., Del Monaco, F., Di Paolo, L.,

Mastalerz, M., Monaco, P., & Tallini, M. (2013). Evidence for strong middle Pleistocene earthquakes in the epicentral area of the 6 April 2009 L'Aquila seismic event from sediment paleofluidization and overconsolidation. *Journal of Geophysical Research: Solid Earth*, *118*(7), 3767–3784. https://doi.org/10.1002/jgrb.50254

Stucchi, M., Meletti, C., Montaldo, V., Crowley, H., Calvi, G. M., & Boschi, E. (2011). Seismic hazard assessment (2003-2009) for the Italian building code. *Bulletin of the Seismological Society of America*, *101*(4), 1885–1911. https://doi.org/10.1785/0120100130

Tallini, M., Gasbarri, D., Ranalli, D., & Scozzafava, M. (2006). Investigating epikarst using low-frequency GPR: Example from the Gran Sasso range (Central Italy). *Bulletin of Engineering Geology and the Environment*, *65*(4), 435–443. https://doi.org/10.1007/s10064-005-0017-y

Tallini, M., Lo Sardo, L., & Spadi, M. (2020). Seismic site characterisation of Red Soil and soil-building resonance effects in L'Aquila downtown (Central Italy). *Bulletin of Engineering Geology and the Environment*, *79*(8), 4021–4034. https://doi.org/10.1007/s10064-020-01795-x

Tallini, M., Spadi, M., Cosentino, D., Nocentini, M., Cavuoto, G., & Di Fiore, V. (2019). High-resolution seismic reflection exploration for evaluating the seismic hazard in a Plio-Quaternary intermontane basin (L'Aquila downtown, central Italy). *Quaternary International*, *532*, 34–47. https://doi.org/10.1016/j.quaint.2019.09.016

Tertulliani, A., Leschiutta, I., Bordoni, P., & Milana, G. (2012). Damage distribution in L'Aquila city (central Italy) during the 6 April 2009 earthquake. *Bulletin of the Seismological Society of America*, *102*(4), 1543–1553. https://doi.org/10.1785/0120110205

Tertulliani, Andrea, & Graziani, L. (2022). A critical overview of the January-February 1703 seismic sequence in central Italy. *Bulletin of Geophysics and Oceanography*,

63(4), 541–554. https://doi.org/10.4430/bgo00396

Tertulliani, Andrea, Rossi, A., Cucci, L., & Vecchi, M. (2009). L'Aquila (Central Italy) earthquakes: The predecessors of the april 6, 2009 event. *Seismological Research Letters*, *80*(6), 1008–1013. https://doi.org/10.1785/gssrl.80.6.1008

Tertulliani, Arcoraci, L., Berardi, M., Bernardini, F., Camassi, R., Castellano, C., Del Mese, S., Ercolani, E., Graziani, L., Leschiutta, I., Rossi, A., & Vecchi, M. (2011). An application of EMS98 in a medium-sized city: The case of L'Aquila (Central Italy) after the April 6, 2009 Mw 6.3 earthquake. *Bulletin of Earthquake Engineering*, *9*(1), 67–80. https://doi.org/10.1007/s10518-010-9188-4

Tomás, R., Romero, R., Mulas, J., Marturià, J. J., Mallorquí, J. J., Lopez-Sanchez, J. M., Herrera, G., Gutiérrez, F., González, P. J., Fernández, J., Duque, S., Concha-Dimas, A., Cocksley, G., Castañeda, C., Carrasco, D., & Blanco, P. (2014). Radar interferometry techniques for the study of ground subsidence phenomena: A review of practical issues through cases in Spain. *Environmental Earth Sciences*, *71*(1), 163–181. https://doi.org/10.1007/s12665-013-2422-z

Tosi, L., Teatini, P., Carbognin, L., & Brancolini, G. (2009). Using high resolution data to reveal depth-dependent mechanisms that drive land subsidence: The Venice coast, Italy. *Tectonophysics*, *474*(1–2), 271–284. https://doi.org/10.1016/j.tecto.2009.02.026

Ufficio Speciale per la Ricostruzione dell'Aquila. (n.d.). *USRA*. Retrieved November 23, 2023, from https://usra.it/

Valensise, G., Tarabusi, G., Guidoboni, E., & Ferrari, G. (2017). The forgotten vulnerability: A geology- and history-based approach for ranking the seismic risk of earthquake-prone communities of the Italian Apennines. *International Journal of Disaster Risk Reduction*, *25*(August), 289–300. https://doi.org/10.1016/j.ijdrr.2017.09.014

Vallone, P., Giammarinaro, M. S., Crosetto, M., Agudo, M., & Biescas, E. (2008). Ground motion phenomena in Caltanissetta (Italy) investigated by InSAR and

geological data integration. *Engineering Geology*, *98*(3–4), 144–155.
https://doi.org/10.1016/j.enggeo.2008.02.004

Walters, R. J., Elliott, J. R., D'Agostino, N., England, P. C., Hunstad, I., Jackson, J. A.,
Parsons, B., Phillips, R. J., & Roberts Edinburgh, G. (2009). The 2009 L'Aquila
earthquake (central Italy): A source mechanism and implications for seismic
hazard. *Geophysical Research Letters*, *36*(17), 2–7.
https://doi.org/10.1029/2009GL039337